

ROBUST QUANTUM STORAGE WITH THREE ATOMS

Han Rui



NATIONAL UNIVERSITY OF SINGAPORE

2012

ROBUST QUANTUM STORAGE WITH THREE ATOMS

HAN RUI

B.Sc. (Physics), NUS

A THESIS SUBMITTED FOR THE DEGREE OF
DOCTOR OF PHILOSOPHY

CENTRE FOR QUANTUM TECHNOLOGIES
NATIONAL UNIVERSITY OF SINGAPORE

2012

DECLARATION

I hereby declare that the thesis is my original work and it has been written by me in its entirety. I have duly acknowledged all the sources of information which have been used in the thesis.

This thesis has also not been submitted for any degree in any university previously.



Han Rui

10 Jan 2013

*Dedicated to my parents, friends
and teachers...*

Acknowledgments

First of all, I would like to thank my supervisor Prof. Berthold-Georg Englert for his tireless support throughout my undergraduate study and four years of Ph.D. candidature in Singapore. I am deeply grateful for your invaluable guidance, as well as your passion in Physics that inspires and encourages me always. Thank you for the unconditional support and freedom that is provided through the years.

Thank you, Ng Hui Khoon for collaborating with me on much of the work in the past few years, and also for your patience in teaching me and making our discussions effective and enjoyable. Thank you, Jun Suzuki for the support on the work of quantum storage and guiding me at the beginning of my Ph.D candidature. Thank you to Niels Lörch and Vanessa Paulisch for working with me during your internships in Singapore.

A special thank to Marta Wolak for making the office cheerful, to Shang Jiangwei for being supportive always and to Lee Kean Loon for many very helpful discussions. I would like to express my gratitude to all my colleagues who gave me the possibility to complete this thesis, especially to Philippe Raynal, Arun, Christian Miniatura, Benoît Grémaud, Paul Constantine Condylys, Mile Gu and our dearest “boss” Ola Englert.

I would like to take this opportunity to convey my sincere thanks to János Bergou, Hans Briegel, Kae Nemoto, Maciej Lewenstein and Gerd Leuchs for the wonderful hospitality and enlightening discussions during my visit to their groups.

Thanks to Tan Hui Min Evon, Wang Yimin, Li Wenhui and Wu Chunfeng for various support, help and the enjoyable female physicists gatherings.

My great appreciation also goes to my dearest friends in Singapore: Lan Tian, Wang Huidong, Zhao Xue and Lai Sha. Thank you for being such wonderful friends for years and making my spare time splendid and colorful.

Last but not least, I would like to thank my parents and Zhao Pan, Guo Qiyou, Zhang Yin for their great supports from China.

I would like to thank again Berthold-Georg Englert and Ng Hui Khooon for your careful reading and useful comments that helped in improving this thesis.

Abstract

In this thesis, we present a systematic construction of a reference-frame-free (RFF) qubit in the noiseless subspace for a system of three identical spin- j atoms. The explicit example of three spin-1/2 ${}^6\text{Li}$ atoms trapped in an optical lattice is studied to demonstrate the robustness of the RFF qubit storage. The resulting coherence time can be many days and the fidelity of 99.99% is maintained for 2 hrs, with conservatively estimated parameters, making RFF qubits of this kind promising candidates for quantum information storage units. A qubit preparation scheme using the Rydberg blockade mechanism is presented, and the scheme is numerically proven to be robust with a modest estimation of about 98% of the preparation fidelity with existing technologies. The excitation of an atom from the ground state to the Rydberg state is done with a stimulated Raman transition, which is a powerful tool for the manipulation of atoms. In the last part of this thesis, a new methodology for studying the three-level Raman transition in a single atom is presented. Solutions more accurate than those relying on the conventional adiabatic elimination method are obtained without increasing the computational complexity by much. This new method can also be applied to the multi-atom Rydberg excitation that is used for the RFF state preparation.

ABSTRACT

Contents

Acknowledgments	i
Abstract	iii
List of Figures	ix
1 Introduction	1
1.1 Quantum computation and quantum memories	1
1.2 Physical implementation of qubits	3
1.3 Quantum information with Rydberg atoms	7
1.4 Stimulated Raman transition	10
2 Construction of the RFF qubit	13
2.1 RFF states	14
2.1.1 RFF qubit from three spin-1/2 particles	14
2.1.2 RFF qubit from four spin-1/2 atoms	18
2.1.3 RFF qubit from three spin-1 atoms	19
2.2 Physical carrier and geometry	22
2.2.1 Neutral atoms in an optical lattice	22
2.2.2 Ions in a linear trap and other systems	30
2.3 Summary	31
3 Robustness of the RFF Qubit	33
3.1 Three spin-1/2 ${}^6\text{Li}$ in equilateral triangle configuration	35
3.1.1 Noise model for the magnetic field	35
3.1.2 Lithium-6	38
3.1.3 Master equation	42
3.1.4 Time dependence of RFF-qubit variables	46
3.1.5 Compare to decoherence of a single-atom qubit	47
3.2 Non-ideal geometry	50

CONTENTS

3.2.1	Center-of-mass probability distribution	50
3.2.2	Distortion of equilateral triangle geometry	52
3.2.3	Time dependence of RFF-qubit variables	54
3.2.4	Compensating for triangle distortions	59
3.3	Robustness of the RFF qubit from four spin-1/2 atoms	60
3.3.1	The 2D square geometry	60
3.3.2	The 3D pyramid geometry	63
3.4	Alternatives	65
3.4.1	RFF qubit from three ^{87}Rb atoms	65
3.4.2	Ions in a linear trap	69
3.5	Summary and discussion	71
4	State preparation of the RFF qubit	75
4.1	Rydberg Blockade	75
4.2	General Scheme of RFF State Preparation	79
4.3	Choice of atoms	86
4.3.1	Three ^6Li atoms	87
4.3.2	Three ^{87}Rb atoms	89
4.3.3	Three $^{40}\text{Ca}^+$ ions	89
4.4	Robustness of RFF State Preparation	91
4.4.1	Error analysis	91
4.4.2	Numerical simulation	97
4.5	Summary	103
5	Raman-type Transitions	105
5.1	The three-level system	106
5.2	Adiabatic Elimination	109
5.2.1	The methodology	109
5.2.2	Light shift	111
5.2.3	Problems with adiabatic elimination	113
5.3	Without adiabatic elimination	115

5.3.1	General methodology	115
5.3.2	Resonant two-photon transitions ($\delta = 0$) — exact solution . .	117
5.3.3	Non-resonant two-photon transitions ($\delta \neq 0$)	120
5.3.4	Discussion	126
5.4	Multi-atom collective Rydberg transitions	129
5.4.1	Two-atom collective Rydberg excitation	130
5.5	Summary	138
6 Conclusion and outlook		141
Appendices		143
A Reduced dipole matrix element		145
B Unitarity of the approximate evolution operators		151

CONTENTS

List of Figures

2.1	Six coplanar laser beams consist of two sets of three coherent beams; the angle between beams within each set is $2\pi/3$. The respective wave vectors have lengths $ \mathbf{k}_1 = \mathbf{k}_2 = \mathbf{k}_3 = 2\pi/\lambda$ and $ \mathbf{k}_4 = \mathbf{k}_5 = \mathbf{k}_6 = 2\pi/\lambda'$. Different lattice structures can be created by alternating the phases of the laser beams. For the lattice of our design, we keep the set of beams with wavelength λ to be in phase and the phases for the other three beams with wavelength λ' are $2\pi/3$, 0 , and $-2\pi/3$	23
2.2	The left-hand side is a contour plot of the potential energy $V(x, y)$ in Eq. (2.30) with $(E_0/E'_0)^2 = 3$ and $\lambda/\lambda' = 5$. One unit is equal to $\lambda/2\pi$ in the plots. Red-detuned lasers ($\delta < 0$) are used. The darker is the color, the higher is the potential at the region. The plot on the right-hand side shows the potential maxima produced by the two sets of laser beams individually; the big circles indicate the potential maxima produced by lasers of frequency λ and the small circles indicate the potential maxima produced by lasers of frequency λ'	25
2.3	The left-hand side shows the potential along the vertical cut-off line in plot (b) of Fig. 2.2; and the left-hand side shows the potential along the horizontal cut-off line in plot (b) of Fig. 2.2.	25
2.4	Six coplanar laser beams consist of a set of three coherent beams indicated by red arrows and another set of three coherent beams indicated by blue arrows. The angle between neighboring beams is $\pi/3$	26
2.5	The left hand side is a contour plot with lasers set in the configuration shown in Fig. 2.4 with $V_1/V_2 = 3$ and $\lambda/\lambda' = 4/\sqrt{3}$	26
2.6	Three ions trapped in a linear Paul trap.	31

LIST OF FIGURES

3.1	Three ${}^6\text{Li}$ atoms are trapped at the corners of an equilateral triangle. The probability clouds indicate the center-of-mass distributions whose spread w is about one-sixteenth of a , the distance between the atoms.	39
3.2	Ground-state hyperfine levels of the neutral ${}^6\text{Li}$ atom. The $f = 3/2$ quartet is separated from the $f = 1/2$ doublet by a transition frequency of 228.2 MHz. Three ${}^6\text{Li}$ atoms confined to their $f = 1/2$ ground states serve as the spin-1/2 particles from which the RFF qubit is constructed.	39
3.3	Level scheme for the effective three-atom Hamiltonian of Eq. (3.22). The separations are not drawn to scale: $\hbar\omega_0$ is many orders of magnitude larger than $\hbar\Omega$. The two $J = 1/2$ levels are degenerate doublets; this degeneracy is exploited for the encoding of the robust signal qubit.	41
3.4	Comparison of the data from a numerical simulation with the analytical results of Eqs. (3.46). Curve “a” displays $\langle P_{J=1/2} \rangle_t$, curves “b” show $\langle \Sigma_1 \rangle_t$ for $\langle \Sigma_1 \rangle_0 = 1$, and curve “c” is for $\langle \Sigma_3 \rangle_t$ with $\langle \Sigma_3 \rangle_0 = 1$. The crosses are from a simulation of the dynamics, averaged over 1000 runs. The solid-line curves represent the analytical results of Eqs. (3.46). The dotted “b” curve shows what one would get for $\langle \Sigma_1 \rangle_t$ if Ω vanished rather than being large on the scale set by τ ; we observe that the inter-atomic dipole-dipole interaction accelerates the decay of $\langle \Sigma_1 \rangle_t$. For the parameter values used throughout the paper, the time range is 3×10^{10} s (roughly 1000 years); see Eq. (3.35) for the value of τ	47

<p>3.5 Fidelity of the RFF qubit. For $\Omega_2/\Omega_1 = 10^{-4}$, the plots show $F(t)$ of Eq. (3.89) and its lower bound of Eq. (3.90) for $t < 45 \times 2\pi/\Omega_1$ (top plot), for $t < 150 \times 2\pi/\Omega_1$ (inset in the top plot), and for $t < 2\pi/\Omega_2$ (bottom plot). Curve ‘a’ is the lower bound on $F(t)$; the other three curves are for $\langle \Sigma_1^{(\varphi)} \rangle_0 = 0.4$ and $s(0) = 1$ (curve ‘b’), $s(0) = 0.8$ (curve ‘c’), and $s(0) = 0.6$ (curve ‘d’). One can clearly see the small-amplitude short-period oscillations and the large-amplitude long-period oscillation. For the parameter values used throughout the paper, the respective time ranges are 2, 7, and 450 hours. We have $\Omega_1 \approx \Omega$, with $\Omega = 2\pi \times 6\text{mHz}$ given in Eq. (3.20).</p>	58
<p>3.6 RFF qubit constructed from four spin-1/2 atoms. (i) Two-dimensional square configuration. The dipole-dipole interaction is unavoidably unbalanced here because the distance for the two diagonal pairs is larger than the distance for the four edge pairs. (ii) Three-dimensional pyramidal configuration. Here, if the height h is chosen such that $b/a = 0.661$, the effective dipole-dipole interaction has equal strength for all six pairs of atoms.</p>	61
<p>3.7 Lower bounds for the fidelity $F(t)$ (solid curve) and the expectation value $\langle P_{J=0} \rangle_t$ (dashed curve) for the RFF qubit constructed from four spin-1/2 atoms at the corners of a perfect square. The fidelity of Fig. 3.5 (three atoms with non-ideal geometry) would be indiscernible from $F(t) = 1$ here.</p>	63
<p>3.8 Energy level structure of ^{87}Rb ground state.</p>	65
<p>3.9 Apply the bias magnetic field in the e_z direction to the line of atoms; when $(e_z \cdot \mathbf{n})^2 = 1/3$, the effective dipole-dipole interaction vanishes. The atoms do not need to be placed at equal distance.</p>	70

LIST OF FIGURES

4.1	Energy levels of the coherent excitations of two-atom systems. Plot ‘a’ shows the energy level for the double excitation to a low-lying excited state $ e\rangle$; plot ‘b’ shows the energy level for double excitation to a Rydberg state $ r\rangle$, where the energy of state $ rr\rangle$ is shifted away from $2E$ by ΔE given in Eq. (4.5), and the true energy level is indicated by the red curves.	77
4.2	Coherently driving the transition between the ground state and a Rydberg state in a three-atom system; only single Rydberg excitation can be obtained owing to the Rydberg-blockade mechanism.	79
4.3	Optical pumping of spin- F atoms to the $S_{1/2}$ ground state with $m_f = F$ by applying a σ_+ pumping light field that is coupled to the $P_{1/2}$ excited state.	81
4.4	Population transfer between the ground state $ g_+\rangle$ and the excited state $ r\rangle$ with a stimulated Raman transition via the intermediate state $ e\rangle$	81
4.5	Population transfer between the ground state $ g_-\rangle$ and the excited state $ r\rangle$ with a Raman transition via the intermediate state $ e\rangle$	82
4.6	The geometrical phase of state $ +,0\rangle$ is imprinted by shining a laser with wave vector \mathbf{k}_0 at incident angle θ . Angle θ is determined by Eq. (4.13).	83
4.7	Top view of the trio of atoms and two applied coherent laser beams with wavevectors \mathbf{k}_0 and \mathbf{k}_1 and polarization vectors $\boldsymbol{\epsilon}_0$ and $\boldsymbol{\epsilon}_1$, as given in Eqs. (4.15) and (4.16).	85
4.8	Energy diagram of the ${}^6\text{Li}$ $2s$ and $2p$ levels [1].	87
4.9	Optical transition diagram of the RFF state preparation with ${}^6\text{Li}$ atoms.	88
4.10	Energy diagram of the $5s$ and $5p$ levels of ${}^{87}\text{Rb}$	89
4.11	Optical transition diagram of the RFF state preparation with ${}^{87}\text{Rb}$ atoms.	90

4.12 Optical transition diagram of the RFF state preparation with $^{40}\text{Ca}^+$ ions.	90
4.13 The geometry of the three atoms and the incident laser labeled by \mathbf{k}_0, ϵ_0 with imperfection.	96
4.14 Two-atom energy level structure near the $ 43s, 43s\rangle$ state.	99
4.15 The population of the states during a 2π excitation pulse, for $\Delta = 800\text{MHz}, \Omega_0 = 120\text{MHz}$ and $\Omega_1 = 80\text{MHz}$. The black curve shows the population of the ground state $ ggg\rangle$; the blue curve shows the population of the collective single-Rydberg-excitation state; the green curve shows the population of the state with a single collective excitation to the intermediate $5p_{1/2}$ state; the red curve shows the population of states with one atom excited to $43s_{1/2}$ and one atom excited to $5p_{1/2}$. The populations of the other states are very small and not shown on this plot.	100
4.16 Frequency histogram for the fidelities of the state preparation over 200 numerical simulations. The errors of the parameters are randomly selected from normal distributions with the error ranges stated in this section.	101
4.17 The upper plot shows frequency histogram of the fidelities of preparing state $ 0\rangle + 1\rangle$ over 100 numerical simulations. The lower plot shows population of the states during a 2π excitation pulse, for $\Delta = 800\text{MHz}, \Omega_0 = 80\text{MHz}$ and $\Omega_1 = 40\text{MHz}$. The black curve shows the population of the ground state $ ggg\rangle$; the blue curve shows the population of the collective single-Rydberg-excitation; the green curve shows the population of single collective excitation to the intermediate $5p_{1/2}$ state; and the red curve shows the population of states with one atom excited to $43s_{1/2}$ and one atom excited to $5p_{1/2}$.102	102

LIST OF FIGURES

5.1	Level scheme of a typical Raman transition. (a) shows the level structure of a Λ -type Raman transition and (b) shows the level structure of a cascade-type Raman transition. Ω_0 and Ω_1 denote the Rabi frequencies of the individual two-level transitions, Δ denotes the detuning of the laser from the transition frequency of the excited state and δ is the detuning of the two-photon transition. The requirement is that the detuning Δ is much larger than the Rabi frequencies so that the excited state $ e\rangle$ is not significantly populated.	107
5.2	Fidelity between the two states at later times evolving with the exact Hamiltonian but taking different δ values given by Eq. (5.17) and Eq. (5.20). $\Delta = 400\text{MHz}$ and $ \Omega_1 = 40\text{MHz}$ are fixed and there different curves are for different ratio of $ \Omega_0/\Omega_1 $	112
5.3	Population distribution for a single-atom Raman transition in time when $\delta = 0$. The solid curves show the exact solution, and the dashed curves the adiabatic-elimination approximation. The initial state is $ 0\rangle$. The red curves are for the ground-state population $ c_0(t) ^2$, the blue curves for $ c_1(t) ^2$, and the orange curves report $ c_e(t) ^2$, the population in the excited state. The detuning is $\Delta = 400\text{ MHz}$ for all plots; the top left plot is for $ \Omega_0 = \Omega_1 = \Delta/10 = 40\text{ MHz}$; the top right plot is for $ \Omega_0 = \Delta/10 = 40\text{ MHz}$ and $ \Omega_1 = \Delta/16 = 25\text{ MHz}$; the bottom plot is for $ \Omega_0 = \Omega_1 = \Delta/4 = 100\text{ MHz}$	119

5.4 Plots of populations obtained from different zeroth-order solutions of the Lippmann-Schwinger equations. Blue curves give the exact results from numerical simulation using the Hamiltonian H_1 ; green curves show solutions from the symmetric approximation $\tilde{U}_0^{(S)}(t)$; red curves show solutions from $\tilde{U}_0^{(R)}(t)$; and orange curves show solutions from $\tilde{U}_0^{(L)}(t)$. The parameters are $\Delta = 400$ MHz, $|\Omega_0| = \Delta/2$, $|\Omega_1| = 3\Delta/10$ and $\delta = -\Omega^\dagger \sigma_3 \Omega / (4\Delta) = (|\Omega_1|^2 - |\Omega_0|^2) / (4\Delta) = -16$ MHz. The effective Rabi frequency is $\Omega_R = 27.8$ MHz, about 7% of Δ . Initially, we have $c_0(0) = 1$ and $c_1(0) = c_e(0) = 0$. The curves starting at 1 show the approximations for $|c_0(t)|^2$; the curves that start at 0 and rise to 1 are for $|c_1(t)|^2$; and the curves that start at 0 and never exceed small values are for $|c_e(t)|^2$ 124

5.5 Comparison of the probabilities obtained from the zeroth-, first-, and second-order approximations of the Lippmann-Schwinger equations Eq. (5.37) and Eq. (5.40). In plot (a), the blue, green, and red curves show solutions from $\tilde{U}_0^{(R)}(t)$, $\tilde{U}_1^{(R)}(t)$, and $\tilde{U}_2^{(R)}(t)$, respectively; and in plot (b), the blue, green, and red curves show solutions from $\tilde{U}_0^{(L)}(t)$, $\tilde{U}_1^{(L)}(t)$, and $\tilde{U}_2^{(L)}(t)$, respectively. The parameters and the initial state are the same as in Fig. 5.4. 126

5.6 Comparison of the zeroth-, first-, and second-order approximations of the symmetric Lippmann-Schwinger Eq. (5.42). The parameter values, the initial state, and the color coding are the same as in Fig. 5.5. 127

5.7 Improvement on the effective two-level Hamiltonian compared with adiabatic elimination. The black curves give the exact numerical solution; the green curves are for the symmetric zeroth-order approximation of $U(t)$; the blue dashed curves are for the adiabatic-elimination approximation; and the red curves result from taking M_0 as the effective Hamiltonian. The parameter values and the initial state are the same as in Figs. 5.4. 128

LIST OF FIGURES

- 5.8 Level diagram of a two-atom Rydberg excitation. The transition between the ground state $|g\rangle$ and the excited state $|e\rangle$ is detuned by $-\Delta + \delta/2$; the transition between the excited state $|e\rangle$ and the Rydberg state $|r\rangle$ is detuned by $\Delta + \delta/2$. $\hbar\omega_{dd}$ is the energy shift arising from the Rydberg blockade mechanism. 132
- 5.9 Population distribution for a collective single Rydberg excitation of two atoms with Rydberg blockade. The black curves give the exact numerical solution; the green curves are for the symmetric zeroth-order approximation of $U(t)$; the blue dashed curves are for the adiabatic-elimination approximation; and the red curves give the result from using the effective Hamiltonian H_R in Eq. (5.63). The detuning is $\Delta = 400\text{MHz}$, $\omega_{dd} = 2\text{GHz}$, $\delta = 0$ and coupling strengths $|\Omega_0| = |\Omega_1| = 3\Delta/10$. Initially, we have all the population in the ground state $|v_1\rangle$. The curves that start at 0 show the results for population in state $|v_1\rangle$; the curves that start at 0 and rise to approximately 1 show the population in state $|v_2\rangle$; and the curves that oscillate with small amplitudes are for the populations in state $|v_3\rangle$ and $|v_4\rangle$ 137

Introduction

1.1 Quantum computation and quantum memories

The processing of quantum information — be it for quantum communication, for quantum key distribution, or for quantum computation — has experienced tremendous progress over the past decades, much inspired by Feynman’s 1980s original proposal of using quantum computers to simulate other quantum systems [2]. It has already been shown theoretically that quantum computers would dramatically improve computational power for particular tasks. One of the most important examples in which the quantum computer outperforms the classical computer is factoring large numbers. This is particularly important for secure data encryption: A quantum computer can factorize large numbers much more efficiently with Shor’s algorithm [3] — it is a NP hard problem for a classical computer. While quantum computers have only solved some simple problems with the state-of-the-art experimentally, much more progress has been made in the field of quantum communication. Quantum cryptography allows two distant parties to establish an unconditionally secure quantum key distribution channel [4, 5]. Secure quantum communication over distances of up to hundreds of kilometers has been demonstrated [6]. Owing to photon loss, longer communication channels require quantum repeaters [7], which are small quantum computers that serve as intermediate stations to connect the direct communication channels.

The basic quantum information unit is a qubit that can be written in the form of a ket state $|\Psi\rangle = \alpha|0\rangle + \beta|1\rangle$, where $|0\rangle$ and $|1\rangle$ are two orthogonal basis states and the complex numbers α and β give the probabilities of measuring the two states

$|0\rangle$ and $|1\rangle$ while satisfying $|\alpha|^2 + |\beta|^2 = 1$. It is the option that a qubit state can be in a superposition of the basic states $|0\rangle$ and $|1\rangle$ that makes quantum computation distinct from and superior to classical computation.

The processing of quantum information requires the storage, manipulation, and retrieval of qubits that are carried by physical systems. The experimental design of the physical carrier of qubits, or in other words, the “hardware” of the quantum computer, has become a very active field in the past decade. This hardware can consist of selected well-controllable degrees of freedom of physical systems constructed from the smallest forms of matter to large macroscopic systems. A large number of physical systems are being developed for quantum computation — single photons, trapped ions, neutral atoms in optical lattice, Nitrogen-Vacancy (N-V) centers in diamond, quantum dots or superconducting qubit, to name a few. All of them have advantages and disadvantages that make them well-fit for some purposes and unsuitable for others. Review papers written by Ladd *et al.* [8] and Simon *et al.* [9] have discussed various physical qubit candidates and their development in depth.

Other than the ultimate goal of building universal quantum computers for quantum computing and quantum communication, reliable quantum memories are also important in a number of other applications. For example, some quantum memories potentially can be used as sources of deterministic single-photon [10], entangled quantum memories can be used for loophole-free Bell test [11], and quantum memories built upon collective ensembles of particles could in principle enhance precision measurement in metrology [12].

The drawback of using quantum memory compared to classical memory is that the system is quite fragile, because of environmental decoherence and, very often, the indirect access of information. As physical forms of quantum memories are quite diverse, it would not be easy to have a universal set of precise criteria for accessing their performance. However, in general, the central attention is on maintaining coherence of the system over the storage time, the scalability of the system, the ability to precisely control and manipulate the system and, last but not least, the ability to measure it. Decoherence comes in various ways owing to uncontrolled interac-

tion between the qubits and the environments or unwanted interactions between the registers of the quantum memories. Decoherence is an important consideration for all physical implementations, and it is commonly quantified by the T_2 lifetime — the time it takes for the fidelity of state to drop to e^{-1} of its initial value. The scalability is important for the quantum computer to handle sizable tasks, as the computation grows with the dimensionality of the Hilbert space. The control and manipulation of qubit information can be done with gate operations, and the system is required to have a set of universal quantum gates (the single qubit phase gate and the two-qubit CNOT gate [3], for example), while the amount of resources needed must not grow exponentially with the number of operations. Finally, the assessment of the quality of information storage consists of two parts, namely the state initialization and the information decoding. For information that operates upon emitting and absorbing of light, strong light-matter coupling is essential for efficient measurement. The criteria stated above are consistent with the DiVincenzo criteria [13].

1.2 Physical implementation of qubits

In the following paragraphs, we will discuss briefly a very small subset of the many physical candidates for quantum memories. And, we focus on development of the figures of merit listed in the previous paragraph as criteria for a good quantum memory.

A photonic system provides several degrees of freedom that the quantum information can be encoded in, for example, the polarization, the time bin, or the path alternative. The polarization state is most widely used and the single qubit rotation can be done easily using waveplates made of birefringent material. The work of Knill, Laflamme and Milburn in 2001 provides a scheme where scalable and efficient quantum computing is possible using only single-photon sources, detectors and linear optical circuits [14]. This scheme has been demonstrated experimentally [15], using the idea of cluster state quantum computing [16]. However, for the

photonic quantum computer to be efficient, the challenge will be on the realization of high-efficiency single-photon sources and detectors. The obvious advantage of using polarization states of photons as qubits is that, in free space, they are relatively free from decoherence as photons barely interact with the environment. Although, photonic states are robust against decoherence, the photon loss provides the closest to decoherence in long-time storage as well as transmission over long distance. Efforts are also put on producing deterministic interaction between photons [17, 18]. Besides building a photonic quantum computer, studies of photonic qubits also benefits other types of quantum computers as photons are typically good intermediate quantum communication transmitters between matter qubits.

Individual atomic ions can be confined in free space with nanometer precision by nearby electrodes; in a multiple-ion trap, the ions discretely align themselves with typical distances of a few micrometers owing to the Coulomb repulsion between ions. Entanglement among multiple ions can be created with laser-induced couplings of the spins mediated by a collective mode of the harmonic motion in the trap. Recently, up to 14-qubit entanglement has been observed [19]. A scheme for a two-qubit entangling quantum gate was proposed by Cirac and Zoller in 1995 [20], and experimentally demonstrated immediately by Wineland *et al.* later that year [21]. To date, single-qubit gates can be accomplished with 99.5% fidelity within about $3 \mu\text{s}$ [22] and two-qubit gates can be accomplished with 99.3% fidelity on a $50 \mu\text{s}$ timescale [23]. The coherence time of trapped ion systems can be up to tens of seconds and the fidelity of the qubit state measurement can be as high as 99.9%. According to the current state of the art, it appears that trapped ions are leading the pack of the possible qubit candidates on the market, because of their high gate fidelity and long coherence time. However, it becomes difficult to scale the system up to a much larger number of ions.

Qubits from neutral atoms are similar to qubits from trapped ions. Their major advantage over trapped ion, is that the system is much more scalable as arrays of neutral atoms can be confined in free space by an optical lattice generated with the electric field of far-off-resonance lasers. For qubits constructed from single atoms,

1.2. Physical implementation of qubits

a measured qubit fidelity of higher than 93% and a storage time well exceeding 100 μs have been observed [24, 25]. Single-qubit gates can be realized with Rabi oscillations between states, and two-qubit gates have also been demonstrated with the Rydberg blockade mechanism [26, 27]. Recently, there has been much progress on various fronts of ultra-cold atom physics. In particular, the development in performing high-resolution optical dressing and detection of individual atoms in an optical lattice [28] has made the neutral atoms more promising than ever for scalable quantum computing. Strong light-atom interaction is essential for efficient quantum computing, and in order to increase the optical depth, a qubit made from cold trapped atomic ensembles has been pursued as well [29, 30]. The critical challenge for building quantum computer with trapped atoms will be to preserve the high-fidelity control in a system with a large number of atoms.

Quantum dots and N-V centers in diamond are well-engineered “artificial atoms” that are integrated in solid-state devices. Qubits made from these devices are easy to assemble and operate at higher temperatures compared to most atomic qubits. Quantum dots refer to electrons or holes in a localized potential with discrete levels that are bound by impurity in a semiconductor nanostructure. A quantum dot qubit state encoded in the spin states of an electron (or hole) suffers decoherence from the hyperfine coupling between the electrons and the fluctuating nuclear spins, resulting in a coherence time that is limited to a few μs [31]. The control of individual spin can be done either by a microwave drive [32], or by shifting the electrostatic trap for the case of two electrons in a double quantum dot [33]. Single qubit operations have been demonstrated with up to 98% fidelity in under 40 picoseconds [34]. However, the extreme short-range interaction imposes a crucial constraint on doing fault-tolerant quantum error correction [3]. On the other hand, spin qubits from N-V centers in diamond can be initialized quickly in less than one microsecond and detected in a few milliseconds [35]. By growing isotopic-purified ^{12}C diamond, coherence time in the order of a few milliseconds has been demonstrated [36]. Microcavities will play an important role for enhancing the light coupling with the N-V centers [37], but it remains a major challenge to fabricate cavities of good

Chapter 1. Introduction

quality factors for the system.

Last but not least, there is another type of qubits — the most macroscopic qubit prototype — the superconducting qubit. Superconducting qubits are generally made from superconducting LC circuits and the anharmonicity introduced by the Josephson junctions. Two of the quantized levels given by the anharmonicity of the oscillator levels give rise to a qubit, and quantum control is achieved by altering the electric signals. Distinct from the atomic qubits, neighboring superconducting qubits naturally couple to each other, allowing simple two-qubit gates. In the current state-of-the-art, single-qubit operations can be accomplished in nanoseconds with 99.3% fidelity and two-qubit gates can be performed in 30 ns with a fidelity higher than 90% [38]. The typical coherence time of a few microseconds has been demonstrated [39], and this coherence time can be increased up to 100 microseconds by putting the superconducting qubit into a three-dimensional superconducting cavity [40]. Nevertheless, understanding and eliminating the decoherence for superconducting qubits remains a key challenge.

The physical systems being investigated or proposed for possible quantum memories have spanned much of the modern physics. However, it remains unclear which of the technologies, if any, would be the optimal one and eventually be successfully used for quantum computation. Some of them are more scalable than others, while some of them provide easier ways to carry out gates. However, a universal goal and key challenge for all the possible physical implementations of qubit is to eliminate decoherence and achieve long coherence time. To date, the longest coherence time is given by trapped ion qubits, which is a few seconds. Coherence times of other systems are at most on the order of milliseconds.

It is worth emphasizing again that no system is free of decoherence, and in most of the systems coherence is limited by fluctuating magnetic fields. In order to perform fault-tolerant quantum computing (allowed error is on the order of 10^{-4} [41]), the operation time need to be much faster than the coherence time, such that preserving coherence becomes the central challenge for a good quantum memory. The tools we are armed with to fight against decoherence are of three main cate-

gories, namely quantum error correction protocols [42], dynamical decoupling [43] and decoherence-free (DF) subspaces and subsystems [44]. The DF subspaces and subsystems are sometimes also characterized as a special case of quantum error correction, and they have been experimentally demonstrated for various kinds of physical systems, for example, the photonic system [45], the trapped ion qubits [46], the nuclear magnetic resonance (NMR) nuclear spin qubits [47, 48], etc.

In this thesis, we propose a scheme of making a long-lived atomic qubit with a decoherence-free subsystem. The qubit state is encoded in the reference-frame-free (RFF) subsystem of a system of three identical atoms, where the decoherence from fluctuating magnetic field is largely suppressed. A fidelity of 99.99% can be achieved for a storage time of 2 hrs [49]. In Chapter 2, we first introduce the general strategy of constructing the RFF qubits in Sec. 2.1. The examples of qubit construction from three spin-1/2 particles, four spin-1/2 particles, or three spin-1 particles are presented in Sec. 2.1 in detail. We also include a brief discussion on possible physical carriers, i.e., neutral atoms in an optical lattice or trapped ions in Sec. 2.2. Chapter 3 studies the robustness of this RFF qubit against decoherence with the explicit example of three ${}^6\text{Li}$ atoms in an optical lattice, and shows that the system is very robust against both internal and external noise. The robustness study would apply also to RFF qubits made of other types of atoms, and the decoherence is expected to be of a similar scale.

1.3 Quantum information with Rydberg atoms

Quantum computing with neutral atoms has been recently fueled by the ability of making fast quantum gates and generating entanglement with Rydberg atoms — atoms with one or more electrons in a highly excited Rydberg state with a large principle quantum number n .

Neutral atoms interact with each other mainly via electric and magnetic dipole-dipole interactions, as they are the leading terms of the multipole expansion. The interaction between ground state atoms is dominated by the $1/R^6$ van der Waals

interaction at short distance, and the $1/R^3$ electric dipole-dipole interaction takes over as the atomic distance increases. However, this interaction is very weak for atoms trapped in an optical lattice or ultracold atomic ensembles in their ground states, i.e., for a typical atomic distance of about $1 \mu\text{m}$, the interaction is less than 1 Hz in frequency units. Thus, to a large extent, 2D or 3D ultra-cold ground state quantum gases can be modeled as ideal gases for the study of many-body physical phenomena. This also ensures that an array of neutral atom qubits is structurally stable.

The dipole-dipole interaction energy scales polynomially with the principal quantum number n , for example, the van der Waals interaction typically scales as n^{11} [50, 51] and the resonant Förster interaction scales as n^4 [52] (the concept of the van der Waals interaction and Förster interaction will be introduced in Sec. 4.1). Therefore, strong interaction between neutral atoms can be achieved by promoting the atoms to high-lying Rydberg levels. Different from the strong Coulomb interaction between trapped ions that always exists, this Rydberg interaction can be controlled with the coupling of atoms to light fields. The fact that the two-atom Rydberg interaction can be turned on and off with an interaction strength difference of more than 10 orders of magnitude larger makes Rydberg atoms promising for quantum information processing, for carrying out quantum gates in particular.

The idea of using Rydberg interactions for quantum gates was first introduced by Jaksch *et al.* in 2000 [53], and then it was immediately extended to a large ensemble of atoms in a ultracold quantum gas by Lukin *et al.* one year later [29]. These proposals employ the Rydberg blockade mechanism, which refers to the Rydberg excitation of a single atom which blocks other atoms within the Rydberg blockade radius from being excited to the same Rydberg level owing to the strong dipole-dipole interaction between Rydberg levels [54]. In 2009, the experimental observation of Rydberg blockade between two atoms a few micrometers apart was reported by two groups in the same issue of *Nature Physics* [26, 27]. Following that, the feasibility of using Rydberg blockade for realizing a two-qubit CNOT or phase gate has been demonstrated [55, 56]. Although, challenges in improving the gate fi-

delity and generated entanglement remain, the Rydberg blockaded gates seem to be highly promising as the experiments advance in the future. Numerous alternative proposals for quantum gates between two neutral atoms exist, and many of them have been experimentally investigated or are still under investigation. But to date, none of the other attempts has successfully demonstrated a quantum gate between two neutral atoms experimentally other than the Rydberg blockaded gates.

Other than quantum gate operations, the powerful idea of Rydberg blockade has also led to an intensive theoretical and experimental study of applications in other physical systems. Many of these involve the idea that Rydberg blockade is not only a two-body effect but also exists for an ensemble of atoms within the blockade radius. In the field of ultra-cold quantum gases, promising ideas exist for deterministic single atom loading in optical lattices [57], spin squeezing of atomic ensembles [58], collective encoding of many qubit registers [59, 60], many particle quantum entanglement [61, 62], and many others. These also open a possible way of using ultra-cold atomic gases as a basis for dissipative quantum many-body simulations [63]. Other than that, the light interaction with Rydberg atoms has been explored for non-linear optical physics — establishing photon-photon interaction with electromagnetically induced transparency (EIT) [64], and many other aspects. Well-controlled collective Rydberg excitation and photon emission in atomic ensembles can potentially be used to engineer deterministic single-photon sources. Today, much attention has been paid to the physics of Rydberg atoms and Rydberg interactions; and their potential use in advancing many other fields are being investigated intensively.

In this work, we use the Rydberg interaction to do qubit state preparation. In Chapter 4, we first briefly review the physics behind the Rydberg blockade mechanism in Sec. 4.1. Then, in Sec. 4.2, one of the state preparation schemes for the RFF qubit made from a trio of identical atoms is presented, and the use of Rydberg blockade to achieve a single collective excitation among all three atoms is the key element in this scheme. In Sec. 4.3, we further elaborate the scheme for the qubit made from a trio of ${}^6\text{Li}$ atoms, ${}^{87}\text{Rb}$ atoms and ${}^{40}\text{Ca}^+$ ions. Last, a

robustness analysis of the state preparation scheme is presented in Sec. 4.4.

1.4 Stimulated Raman transition

The manipulation of atomic qubit relies on the coupling of the atomic system to external fields. Atomic and molecular systems can be coupled to external fields in various ways leading to the evolution of the atomic states and the change in the population probability distribution. For example, atomic systems can be represented as electric and magnetic dipoles (or multipole) and coupled to external electric and magnetic fields directly. Among all the couplings, the electric dipole is the strongest, thus optically allowed atomic transitions are often stimulated by the electric dipole coupling between the electric field of optical laser beams and the atoms. Dipole permitted transition, according to the dipole selection rule [65], can be driven by a single light beam directly.

The development in understanding and using different techniques for efficient transfer of population to initially unpopulated atomic levels, such as high-lying Rydberg levels or different sub-levels of the hyperfine states, is of key importance not only in manipulation of quantum information but also in other applications, spectroscopy for example. However, such transitions are very often either forbidden by the dipole selection rule or the transition frequency is out of the popular optical range. In this case, one can search ways to establish an efficient transition indirectly through some other intermediate states. Such stimulated processes exist as the three-level Raman transition [66], multi-level Raman transition [67, 68], stimulated Raman adiabatic passage (STIRAP) [69, 70], etc. Most of the processes rely on the fact that the intermediate excited state is not or barely populated, and the system behaves approximately as a two-level quantum system of the two states of interest.

The theory for Raman transition (three or more levels) and STIRAP differ from each other fundamentally. Assuming we are interested in establishing transition between states $|0\rangle$ and $|1\rangle$ through a two-photon process, for a Raman transition, the initial quantum state can be any superposition state of $|0\rangle$ and $|1\rangle$. The laser

1.4. Stimulated Raman transition

fields for the coupling are applied simultaneously, and the system essentially behaves like a two-level system which exhibits Rabi oscillations between the two states, while the intermediate state population is small. Differently, STIRAP has the constraint that the initial state is either $|0\rangle$ or $|1\rangle$ but not a superposition of both. The laser fields for STIRAP are not applied simultaneously, but rather the pulses are switched on and off following a slowly varying time function and one pulse is delayed from the other throughout the whole process. These processes are more capable of transferring population fully from one state to the other and do not have oscillatory behavior. Population transfer using STIRAP is more deterministic, however, and offers less flexibility and operates much more slowly than using stimulated Raman transitions. Thus, stimulated Raman transition has much wider applications than STIRAP and is an extremely powerful and popularly used tool in optical manipulation of atomic systems.

Vast applications of stimulated Raman transition exist for manipulating atomic systems as well as the measurement of fundamental physical parameters. One of the most direct application is of course Rabi flopping between two atomic levels [71]. Free space Raman cooling [72] and Raman side-band cooling [73] allow the cooling of atoms below the limitations of Doppler cooling and also far below the recoil energy of a photon given to an atom. Sequential Raman pulses can be used to craft arbitrary superpositions in systems with numerous metastable states and to prepare such systems in particular states prior to coherent manipulation [74].

As stated previously in Sec. 1.3, Rydberg atoms are widely used in quantum computation and cold-atom physics, as well as the RFF state encoding presented in this thesis. Rydberg excitation and de-excitation are accomplished by two-photon processes most of the time, since the energy required is beyond the popular optical range of lasers. In order to have a fast transition between ground state and Rydberg state, stimulated Raman transition with two lasers via an intermediate excited state is widely used. The analytical study of such processes are normally done first by neglecting states that are not coupled and not populated throughout the entire process to arrive at a three-level Hamiltonian. A suitable interaction picture is

Chapter 1. Introduction

used to obtain a time-independent three-level Hamiltonian and followed by applying *adiabatic elimination* to further reduce it to a two-level effective Hamiltonian, so that the system can be solved easily. Regardless of the wide popularity of using adiabatic elimination, its limitations remain and very often it does not work well.

The material presented in Chapter 5 is not limited to the framework of quantum computation with RFF qubit; rather it deals with the analytical study of the stimulated Raman transition in general. In Chapter 5, we first review the three-level system for Raman transition and the use of the adiabatic elimination method and its limitations in Secs. 5.1 and 5.2. In Sec. 5.3, we describe a new methodology for solving the three-level Raman transition problem with a significant improvement of accuracy without increasing the computational complexity by much. As an extension and also relevant to the RFF qubit preparation, we apply the methodology to multi-atom Rydberg excitation with Raman transition in Sec. 5.4.

Construction of the RFF qubit

Practical applications that go beyond proof-of-principle experiments rely on qubits that are sufficiently robust for the task at hand. For example, fault-tolerant quantum computation requires a gate fidelity that is very close to unity. Lack of control over the system, however, always gives rise to decoherence. The typical decoherence time for quantum dots, ions in a trap, or diamond N-V centers is of the order of microseconds or milliseconds, and a decoherence time of a few seconds is within reach of the current technologies [8]. This is still not quite sufficient for carrying out some complicated gate operations, nor for storage purposes [9].

We explore here a scheme to overcome the decoherence problem with reference-frame-free (RFF) qubits constructed from three identical particles. These RFF qubits have a remarkably long lifetime — a NMR proof-of-principle experiment that employs three spin-1/2 nuclei is on record [48] — and the alignment of reference frames between observers, or the drift of frame between storage and read-out, is not an issue.

The said construction of RFF qubits from trios of spin-1/2 atoms was studied previously in [75, 76]. These atoms are individually highly sensitive to magnetic stray fields, but their symmetric RFF states are completely insensitive as long as the stray field affects all three atoms in the same way [77]. This makes the RFF qubits good candidates for long-time quantum storage units.

In this chapter, we will first discuss the general structure of the RFF subspace and study a few examples explicitly, i.e., RFF qubit constructed from three spin-1/2 particles, RFF qubit constructed from four spin-1/2 particles, and RFF qubit constructed from three spin-1 particles. Then we will move on to studying the

possibility of using neutral atoms in an optical lattice and trapped ions as physical carriers of the RFF qubit and their properties.

2.1 RFF states

The problems in controlling and preserving coherence in quantum systems make it natural for researchers to put in effort for searching for the possibility of constructing quantum states which are decoherence-free (DF) or reference-frame free. This has been widely discussed [75], and generally it is believed that it is possible to find DF subsystems (or subspaces) and RFF quantum states in any finite dimension. Suzuki *et al* [76]. have shown that there is a symmetric construction of d -dimensional RFF states out of $N = d + 1$ spin-1/2 constituents. For the purpose of this thesis, we first give the explicit construction of RFF states out of three or four spin-1/2 particles following the scheme presented in [76], and then also extend it to RFF states with three spin-1 atoms.

2.1.1 RFF qubit from three spin-1/2 particles

For a system of three spin-1/2 particles, the total spin J of the system can be either 1/2 or 3/2. In the $J = 3/2$ subspace, there are four states with distinct M (magnetic quantum number); in the $J = 1/2$ subspace, there are two different M values, namely $M = \pm 1/2$, with two states each. Upon labeling the degenerate states for $J = 1/2$ by the quantum number λ , we have $|J = 1/2, M = \pm 1/2, \lambda\rangle$ with $\lambda = 0$ or $\lambda = 1$.

We construct these four orthogonal basis kets in the $J = 1/2$ sector by a variant of the procedure described in Ref. [76]. When denoting the Pauli vector operator for the k th atom by σ_k , the total spin vector operator is given by

$$\mathbf{J} = \frac{1}{2} \sum_{k=1}^3 \sigma_k \quad (2.1)$$

in units of \hbar . The lowering operator $J_- = J_x - iJ_y$ has the partner operators¹

$$Q_0 = \frac{1}{\sqrt{3}} \sum_{k=1}^3 q^k \sigma_{k-}, \quad Q_1 = \frac{1}{\sqrt{3}} \sum_{k=1}^3 q^{-k} \sigma_{k-}, \quad (2.2)$$

where $\sigma_{k-} = (\sigma_{kx} - i\sigma_{ky})/2$ is the lowering operator for the k th atom, and $q = e^{i2\pi/3}$ is the basic cubic root of unity. We write $|\pm, \lambda\rangle$ for $|J = 1/2, M = \pm 1/2, \lambda\rangle$ for brevity and choose the “+” kets in accordance with

$$|+, \lambda\rangle = Q_\lambda |\uparrow\uparrow\uparrow\rangle, \quad (2.3)$$

and an application of J_- gives the corresponding “−” kets,

$$|-, \lambda\rangle = J_- |+, \lambda\rangle = J_- Q_\lambda |\uparrow\uparrow\uparrow\rangle, \quad (2.4)$$

with the outcomes

$$\begin{aligned} |+, 0\rangle &= (|\downarrow\uparrow\uparrow\rangle q + |\uparrow\downarrow\uparrow\rangle q^2 + |\uparrow\uparrow\downarrow\rangle) / \sqrt{3}, \\ |+, 1\rangle &= (|\downarrow\uparrow\uparrow\rangle q^2 + |\uparrow\downarrow\uparrow\rangle q + |\uparrow\uparrow\downarrow\rangle) / \sqrt{3} \end{aligned} \quad (2.5)$$

and

$$\begin{aligned} |-, 0\rangle &= -(|\uparrow\downarrow\downarrow\rangle q + |\downarrow\uparrow\downarrow\rangle q^2 + |\downarrow\downarrow\uparrow\rangle) / \sqrt{3}, \\ |-, 1\rangle &= -(|\uparrow\downarrow\downarrow\rangle q^2 + |\downarrow\uparrow\downarrow\rangle q + |\downarrow\downarrow\uparrow\rangle) / \sqrt{3}. \end{aligned} \quad (2.6)$$

The arrows symbolize “spin up” and “spin down” in the z -direction, so that

$|\uparrow\uparrow\uparrow\rangle = |J = 3/2, M = 3/2\rangle$ in Eqs. (2.3) and (2.4). The $|\pm, \lambda\rangle$ kets have the usual

¹The correspondence with the conventions of Ref. [76] is the following: What is q here, is ω_3 there; the labels $\lambda = 0, 1$ here are $\lambda = 1, 2$ there; and the operators Q_0 and Q_1 here are $\Omega_-(1)$ and $\Omega_-(2)$ there. Note that an inadvertent interchange between $\lambda = 1$ and $\lambda = 2$ happened in the transition from Sec. III to Sec. IV A in [76].

Chapter 2. Construction of the RFF qubit

properties as eigenstates of J_z , namely

$$\begin{aligned} J_x|\pm, \lambda\rangle &= |\mp, \lambda\rangle/2, \\ J_y|\pm, \lambda\rangle &= |\mp, \lambda\rangle(\pm i/2), \\ J_z|\pm, \lambda\rangle &= |\pm, \lambda\rangle(\pm 1/2), \end{aligned} \tag{2.7}$$

as one verifies immediately.

Since the eigenvalues of \mathbf{J}^2 distinguish the $J = 1/2$ and $J = 3/2$ sectors, we can express the respective projectors in terms of \mathbf{J}^2 ,

$$P_{J=1/2} = \frac{5}{4} - \frac{1}{3}\mathbf{J}^2, \quad P_{J=3/2} = \frac{1}{3}\mathbf{J}^2 - \frac{1}{4}, \tag{2.8}$$

consistent with $1 = P_{J=1/2} + P_{J=3/2}$ and $\mathbf{J}^2 = \frac{3}{4}P_{J=1/2} + \frac{15}{4}P_{J=3/2}$. Alternatively, the projector onto the subspace with $J = 1/2$ is given by

$$\begin{aligned} P_{J=1/2} &= \sum_{\sigma=\pm} \sum_{\lambda=0,1} |\sigma, \lambda\rangle\langle\sigma, \lambda| \\ &= \frac{1}{6}(3 - \boldsymbol{\sigma}_1 \cdot \boldsymbol{\sigma}_2 - \boldsymbol{\sigma}_2 \cdot \boldsymbol{\sigma}_3 - \boldsymbol{\sigma}_3 \cdot \boldsymbol{\sigma}_1), \end{aligned} \tag{2.9}$$

where the latter expression is available either as a consequence of Eqs. (2.5) and (2.6) or of Eqs. (2.8) and (2.1).

The $J = 1/2$ subspace and the $J = 3/2$ subspace are both four-dimensional Hilbert spaces and, therefore, they can be regarded as tensor product spaces of two qubits, respectively. This is of no consequence for the $J = 3/2$ sector, but it permits writing the $J = 1/2$ sector as composed of a rotationally invariant signal qubit — the RFF qubit — and an idler qubit [76]: the kets $|\sigma, \lambda\rangle$ of Eqs. (2.3)–(2.6) are labeled by the idler quantum number $\sigma = \pm$ and the signal quantum number $\lambda = 0, 1$.

With the idler qubit in a maximally mixed state, the RFF state is identified by

$$\rho^{\text{RFF}} = \sum_{\sigma=\pm} \sum_{\lambda, \lambda'=0,1} |\sigma, \lambda\rangle\langle\sigma, \lambda'| \frac{1}{2} \rho_{\lambda\lambda'} = \frac{1}{2} \mathbf{1}_2 \otimes \tilde{\rho}^{\text{RFF}}, \tag{2.10}$$

where this tensor-product structure applies within the subspace with $J = 1/2$. We exhibit the statistical operator of the signal qubit alone,

$$\tilde{\rho}^{\text{RFF}} = \sum_{\lambda, \lambda'=0,1} |\lambda\rangle \rho_{\lambda\lambda'} \langle \lambda'|, \quad (2.11)$$

by tracing over the idler qubit. The hermitian Pauli operators $\Sigma_1, \Sigma_2, \Sigma_3$ for the RFF qubit,

$$\begin{aligned} \frac{1}{2}(\Sigma_1 + i\Sigma_2) &= \sum_{\sigma=\pm} |\sigma, 0\rangle \langle \sigma, 1| = 1_2 \otimes (|0\rangle \langle 1|), \\ \Sigma_3 &= \sum_{\sigma=\pm} \sum_{\lambda=0,1} |\sigma, \lambda\rangle (-1)^\lambda \langle \sigma, \lambda| \\ &= 1_2 \otimes (|0\rangle \langle 0| - |1\rangle \langle 1|), \end{aligned} \quad (2.12)$$

are explicitly given by

$$\begin{aligned} \Sigma_1 + i\Sigma_2 &= \frac{1}{3}(\boldsymbol{\sigma}_1 \cdot \boldsymbol{\sigma}_2 + q^2 \boldsymbol{\sigma}_2 \cdot \boldsymbol{\sigma}_3 + q \boldsymbol{\sigma}_3 \cdot \boldsymbol{\sigma}_1), \\ \Sigma_3 &= \frac{1}{\sqrt{12}} \boldsymbol{\sigma}_1 \cdot (\boldsymbol{\sigma}_2 \times \boldsymbol{\sigma}_3). \end{aligned} \quad (2.13)$$

These are clearly rotationally invariant and possess the algebraic properties of Pauli spin operators in the $J = 1/2$ subspace, such as $(\Sigma_1)^2 = P_{J=1/2}$ and $\Sigma_1 \Sigma_2 = i\Sigma_3$.

Once the information is encoded in a RFF qubit (2.11), with the idler in the maximally mixed state as in Eq. (2.10) or in some other state, the information will be perfectly preserved as long as all three spin-1/2 atoms precess in unison. In the non-ideal circumstances of a real experimental situation, however, the interaction with the environment and the interactions among the physical carriers of the qubit could cause decoherence, because the atoms may be subject to torques of different strengths. Inevitably, there will be sources of noise over which the experimenter lacks control. In this chapter, we will show the explicit constructions of RFF qubits from some specific physical carriers, and the objective of the next chapter is to demonstrate that the information stored in the RFF qubit is preserved for a long time if magnetic stray fields with typical properties affect the carrier atoms.

2.1.2 RFF qubit from four spin-1/2 atoms

The next example is the case of four spin-1/2 constituents, which live in a sixteen dimensional Hilbert space. The total angular momentum of the system can be $J = 0, 1$ or 2 . The two-dimensional $J = 0$ subspace becomes a natural candidate for the RFF qubit, and the RFF qubit in this case is a pure state with no idler component. The leakage of information is to the $J = 1$ and $J = 2$ subspaces, which are nine-dimensional and five-dimensional, respectively. By contrast, a pure state of the three-spin-1/2-atom RFF qubit corresponds to a mixed state of the three-atom system with leakage into the space of the idler qubit and into the $J = 3/2$ sector. Clearly, the two constructions of the RFF qubit are substantially different.

Now, taking a look at the four-atom qubit construction, we note that the projector onto the $J = 0$ subspace is given by

$$P_{J=0} = \frac{2}{3}(S_{12}S_{34} + S_{13}S_{24} + S_{14}S_{23}), \quad (2.14)$$

where the S_{jk} s are the singlet states between j th and k th constituents,

$$S_{jk} = \frac{1}{4}(1 - \boldsymbol{\sigma}_j \cdot \boldsymbol{\sigma}_k) \quad (2.15)$$

for $j, k = 1, 2, 3, 4$ and $j \neq k$. The hermitian RFF Pauli operators are explicitly given by

$$\begin{aligned} \Sigma_1 &= -\frac{2}{3}(2S_{12}S_{34} - S_{14}S_{23} - S_{13}S_{24}), \\ \Sigma_2 &= -\frac{2}{\sqrt{3}}(S_{13}S_{24} - S_{14}S_{23}), \\ \Sigma_3 &= -\frac{i}{\sqrt{3}}[(S_{12}S_{13} - S_{13}S_{12}) - (S_{23}S_{24} - S_{24}S_{23}) + (S_{34}S_{13} - S_{13}S_{34}) \\ &\quad - (S_{14}S_{24} - S_{24}S_{14})]. \end{aligned} \quad (2.16)$$

Other than the $J = 0$ RFF qubit space, the subspace with the second largest angular momentum also contains an interesting RFF qutrit system. The nine dimensional $J = 1$ subspace can be presented as tensor product of a three-dimensional

idler space with $M = -1, 0, 1$ and a RFF qutrit with states labeled by $\lambda = -1, 0, 1$. This system has also been studied previously [76], and we should not repeat it here.

2.1.3 RFF qubit from three spin-1 atoms

The schemes presented so far are RFF states made from spin-1/2 particles, however, we do not have to limit the construction to spin-1/2 particles only. In principle, one can equally well use three identical particles of any non-zero ground-state spin J to construct a RFF signal qubit in the subspace of total angular momentum $3J - 1$, which has two degenerate states for each M value. The idler space is then $(6J - 1)$ -dimensional. Analogously, RFF qutrits can be constructed in the sector of total angular momentum $3J - 2$ from four identical spin J particles. Such alternative constructions offer considerable flexibility in choosing physical carriers of spins for practical implementations.

In this section, we will focus on the construction of RFF qubits from three spin-1 atoms. Physical representations of this kind of qutrit systems are not difficult to find, such as the spin-1 ^{87}Rb in cold atom experiments for example, and the technologies for manipulating ^{87}Rb atoms are very well developed as well.

For a system of three spin-1 particles, the total angular momentum can be $J = 0, 1, 2$ or 3 . The largest angular momentum subspace has seven states with each of them having a distinct magnetic quantum number M ; the second largest angular momentum $J = 2$ subspace has five distinct M values, while each of them has doubly degenerate states; the subspace with angular momentum $J = 1$ has three distinct M values and each of them has a set of triply degenerate states; finally, the subspace with $J = 0$ only has one state with $M = 0$. All of those subspaces add up to a 27-dimensional Hilbert space.

As we have already mentioned, the $J = 2$ subspace can be presented as a tensor product of a RFF signal qubit and a five-dimensional idler space. For example, a product state can be represented as

$$\rho_{J=2} = \sum_{M, M'=-2}^2 |M\rangle \rho_{M, M'} \langle M'| \otimes \sum_{\lambda, \lambda'=0,1} |\lambda\rangle \rho_{\lambda, \lambda'} \langle \lambda'|. \quad (2.17)$$

Chapter 2. Construction of the RFF qubit

The state is rotationally invariant (or RFF) when the idler is in a completely mixed state. The $M = \pm 2$ states have similar structures as for the system of three spin-1/2 particles, for example,

$$\begin{aligned}
 |M = 2, \lambda = 0\rangle &= \frac{1}{\sqrt{3}}(|011\rangle q + |101\rangle q^2 + |110\rangle), \\
 |M = 2, \lambda = 1\rangle &= -\frac{1}{\sqrt{3}}(|011\rangle q^2 + |101\rangle q + |110\rangle), \\
 |M = -2, \lambda = 0\rangle &= \frac{1}{\sqrt{3}}(|0 \ -1 \ -1\rangle q + |-1 \ 0 \ -1\rangle q^2 + |-1 \ -1 \ 0\rangle), \\
 |M = -2, \lambda = 1\rangle &= -\frac{1}{\sqrt{3}}(|0 \ -1 \ -1\rangle q^2 + |-1 \ 0 \ -1\rangle q + |-1 \ -1 \ 0\rangle),
 \end{aligned} \tag{2.18}$$

where $q = e^{i\frac{2\pi}{3}}$ and the labels in the kets indicates magnetic quantum number $M = -1, 0, 1$ for the individual particles. The $M = 1, 0, -1$ states can be obtained by applying operators J_{\pm} to the states in Eq. (2.19) and the resultant states are slightly more complicated as each of them is a linear combination of six orthogonal states, for example,

$$\begin{aligned}
 |M = 1, \lambda = 0\rangle &= \frac{1}{\sqrt{6}}(|-1, 1, 1\rangle q + |1, -1, 1\rangle q^2 + |1, 1, -1\rangle) \\
 &\quad - \frac{1}{\sqrt{6}}(|1, 0, 0\rangle q + |0, 1, 0\rangle q^2 + |0, 0, 1\rangle), \\
 |M = -1, \lambda = 0\rangle &= \frac{1}{\sqrt{6}}(|1, -1, -1\rangle q + |-1, 1, -1\rangle q^2 + |-1, -1, 1\rangle) \\
 &\quad - \frac{1}{\sqrt{6}}(|-1, 0, 0\rangle q + |0, -1, 0\rangle q^2 + |0, 0, -1\rangle), \\
 |M = 0, \lambda = 0\rangle &= \frac{1}{\sqrt{6}}(1 - q)(|-1, 1, 0\rangle q + |0, -1, 1\rangle q^2 + |1, 0, -1\rangle) \\
 &\quad - \frac{1}{\sqrt{6}}(1 - q)(|1, -1, 0\rangle q + |0, 1, -1\rangle q^2 + |-1, 0, 1\rangle). \tag{2.19}
 \end{aligned}$$

By exchanging $q \leftrightarrow q^2$, we get the states for $\lambda = 1$ with an inverted sign.

For spin-1/2 particles, the angular momentum operator is related to the Pauli operator by $\mathbf{J} = (\hbar/2)\boldsymbol{\sigma}$; for spin-1 particles the components of angular momentum

operator \mathbf{J} are represented by the following three 3×3 matrices:

$$J_x \hat{=} \sqrt{\frac{1}{2}} \begin{pmatrix} 0 & 1 & 0 \\ 1 & 0 & 1 \\ 0 & 1 & 0 \end{pmatrix}, \quad J_y \hat{=} \sqrt{\frac{1}{2}} \begin{pmatrix} 0 & -i & 0 \\ i & 0 & -i \\ 0 & i & 0 \end{pmatrix}, \quad J_z \hat{=} \begin{pmatrix} 1 & 0 & 0 \\ 0 & 0 & 0 \\ 0 & 0 & -1 \end{pmatrix}, \quad (2.20)$$

in units of \hbar . The construction of the RFF operators for spin-1/2 particles makes good use of the swap operators between two constituents in [76]. Though qutrit operators are structurally different from qubit operators, it is still very helpful to define the swap operator between two qutrits first. For two spin-1 particles, the total angular momentum is $J = 0, 1$ or 2 . The $J = 2$ subspace has a basis of five symmetric states, the $J = 0$ subspace consists of one symmetric state and the $J = 1$ subspace has a basis of three anti-symmetric states. Thus, the swap operator, which is symmetric, is given by the sum of the projectors onto the $J = 2$ and $J = 0$ subspaces with the projector onto the $J = 1$ subspace subtracted. Thus, we can write the swap operator between particle j and k as

$$P_{jk} = 1 - \frac{[6 - (\mathbf{J}_j + \mathbf{J}_k)^2](\mathbf{J}_j + \mathbf{J}_k)^2}{4}. \quad (2.21)$$

For three spin-1 particles, the eigenvalues of the operator \mathbf{J}^2 distinguish the subspaces: $J^2 = \{0, 2, 6, 12\}$ for angular momentum $J = \{0, 1, 2, 3\}$, respectively. The projector onto the $J = 2$ subspace where the RFF qubit resides is given by

$$P_{J=2} = -\frac{\mathbf{J}^2(\mathbf{J}^2 - 2)(\mathbf{J}^2 - 12)}{144}, \quad (2.22)$$

where $\mathbf{J} = \mathbf{J}_1 + \mathbf{J}_2 + \mathbf{J}_3$ is the total angular momentum operator for the three-particle system.

The swap operators P_{jks} for two particles are clearly rotationally invariant, we can make use of these swap operators when constructing the rotationally invariant Pauli spin operators of the RFF qubit. However, for this system there are more RFF subspaces, namely the $J = 2$ RFF qubit space and the $J = 1$ RFF qutrit

Chapter 2. Construction of the RFF qubit

space. Therefore, we project those rotationally invariant operators with the right structure into the $J = 2$ subspace to get the right operators that only live in the $J = 2$ subspace. The Pauli operators for the RFF qubit are

$$\begin{aligned}\Sigma_1 + i\Sigma_2 &= \frac{2}{3}P_{J=2} (P_{12} + q^2P_{23} + qP_{31}) P_{J=2}, \\ \Sigma_3 &= \frac{I}{\sqrt{3}}P_{J=2}(P_{31}P_{12} - P_{12}P_{31})P_{J=2}.\end{aligned}\quad (2.23)$$

These Pauli operators have very similar structure as the Pauli operators for RFF qubits made from three spin-1/2 particles, i.e., although the dimensionality of the idler space is different, the RFF qubit structure are essentially the same for these two constructions.

2.2 Physical carrier and geometry

2.2.1 Neutral atoms in an optical lattice

A two-level atom (with transition frequency ω_0 to its excited state) experiences a radiative force when it is exposed to an electromagnetic radiation field due to photon absorption and emission cycles. The amplitude of a monochromatic laser field is given by

$$\mathcal{E}(\mathbf{r}, t) = \mathbf{E}(\mathbf{r})e^{-i\omega_L t}, \quad (2.24)$$

where ω_L is the frequency of the electromagnetic field. The force derived from the polarization energy shift of the atomic levels, and the dipole potential energy due to the laser field is given by

$$V(\mathbf{r}) = \frac{\hbar\Gamma}{8} \frac{\Gamma}{\delta} \frac{I(\mathbf{r})}{I_s}, \quad (2.25)$$

where Γ is the linewidth of the excited state, $\delta = \omega_L - \omega_0$ is the detuning of the applied laser field, $I(\mathbf{r}) = \epsilon_0 c |\mathbf{E}(\mathbf{r})|^2 / 2$ is the light field intensity at the center-of-mass position \mathbf{r} of the atom and I_s is the saturation intensity of the atom under

consideration.

To ensure that the light field does not excite the atoms from the ground state, we need the detuning δ to be much larger than the width Γ . When the light field is blue-detuned from the atomic resonance ($\delta > 0$), the atoms are trapped in the field intensity minima, whereas for red-detuned light ($\delta < 0$) the atoms are trapped at the field intensity maxima. Here, we only make use of the case where the trapping lasers are far red-detuned.

One kind of optical lattice that could be used for the RFF qubit made from three identical atoms is a modification of the Kagome lattice, where we have an equilateral triangular lattice in which every site consists of three spin-J atoms arranged in a small equilateral triangle geometry. A possible physical construction of such a lattice is to use two sets of three coplanar coherent laser beams arranged in the configuration shown in Fig. 2.1 and the angle between the beams within each coherent set is $2\pi/3$.

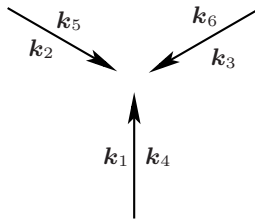


Figure 2.1: Six coplanar laser beams consist of two sets of three coherent beams; the angle between beams within each set is $2\pi/3$. The respective wave vectors have lengths $|\mathbf{k}_1| = |\mathbf{k}_2| = |\mathbf{k}_3| = 2\pi/\lambda$ and $|\mathbf{k}_4| = |\mathbf{k}_5| = |\mathbf{k}_6| = 2\pi/\lambda'$. Different lattice structures can be created by alternating the phases of the laser beams. For the lattice of our design, we keep the set of beams with wavelength λ to be in phase and the phases for the other three beams with wavelength λ' are $2\pi/3$, 0 , and $-2\pi/3$.

One set of three in-plane coherent red-detuned laser beams at angle $2\pi/3$ apart from each other produces an equilateral triangular lattice. We take all the light fields to be linearly polarized and orthogonal to the xy -plane, so that the three complex field amplitudes are given by

$$\mathcal{E}_j(\mathbf{r}, t) = E_0 e^{i(\mathbf{k}_j \cdot \mathbf{r} - \phi_j)} e^{-i\omega_L t} \mathbf{e}_z, \quad (2.26)$$

where \mathbf{k}_j is the wave vector for respective laser field. The optical potential created

Chapter 2. Construction of the RFF qubit

by the electric field of the set of three coherent laser beams with wave vectors \mathbf{k}_1 , \mathbf{k}_2 and \mathbf{k}_3 as shown in Fig. (2.1) is given by

$$V_1(x, y) \propto -E_0^2 \left| e^{2i\pi y/\lambda} + e^{i\pi(\sqrt{3}x-y)/\lambda} + e^{-i\pi(\sqrt{3}x+y)/\lambda} \right|^2, \quad (2.27)$$

where λ is the wavelength and the minus sign accounts for the sign of $\delta < 0$ because red-detuned lasers are used. These three beams form a triangular lattice with lattice constant $a = 2\lambda_L/3$. There is another set of three coherent laser beams in the same geometry with wave vectors \mathbf{k}_4 , \mathbf{k}_5 and \mathbf{k}_6 as shown in Fig. (2.1) and the wavelength $\lambda' \neq \lambda$. The overall potential is obtained by the sum of the potentials produced by the two sets of beams:

$$V(x, y) \propto -E_0^2 \left| e^{2i\pi y/\lambda} + e^{i\pi(\sqrt{3}x-y)/\lambda} + e^{-i\pi(\sqrt{3}x+y)/\lambda} \right|^2 - E_0'^2 \left| e^{2i\pi y/\lambda'} + e^{i\pi(\sqrt{3}x-y)/\lambda' + i\phi_1} + e^{-i\pi(\sqrt{3}x+y)/\lambda' + i\phi_2} \right|^2, \quad (2.28)$$

where ϕ_1 and ϕ_2 take into account the phase difference of the second set of beams. In the case where $\lambda/\lambda' = n$ is an integer, we can make all the maxima of $V_1(x, y)$ coincident with some of the maxima of $V_2(x, y)$ by adjusting the phases of ϕ_1 and ϕ_2 . For example, this can be achieved by taking

$$\phi_1 = -\frac{2\pi}{3} \quad \text{and} \quad \phi_2 = \frac{2\pi}{3}, \quad (2.29)$$

and, of course, the choice of phases is not unique. The total potential is then given by

$$V(x, y) \propto -E_0^2 \left| e^{2i\pi y/\lambda} + e^{i\pi(\sqrt{3}x-y)/\lambda} + e^{-i\pi(\sqrt{3}x+y)/\lambda} \right|^2 - E_0'^2 \left| e^{2i\pi y/\lambda'} + e^{i\pi(\sqrt{3}x-y)/\lambda' - i\frac{2\pi}{3}} + e^{-i\pi(\sqrt{3}x+y)/\lambda' + i\frac{2\pi}{3}} \right|^2, \quad (2.30)$$

and the atoms can be trapped at the maxima of $V(x, y)$. The potential energy or trapping strength depends on the intensity of the lasers as well as the detuning δ . For example, when the ratios between the two potential energies are $(E_0/E_0')^2 = 3$

2.2. Physical carrier and geometry

and $\lambda/\lambda' = 5$, a contour plot of the potential $V(x, y)$ is shown in Figs. (2.2) and (2.3).

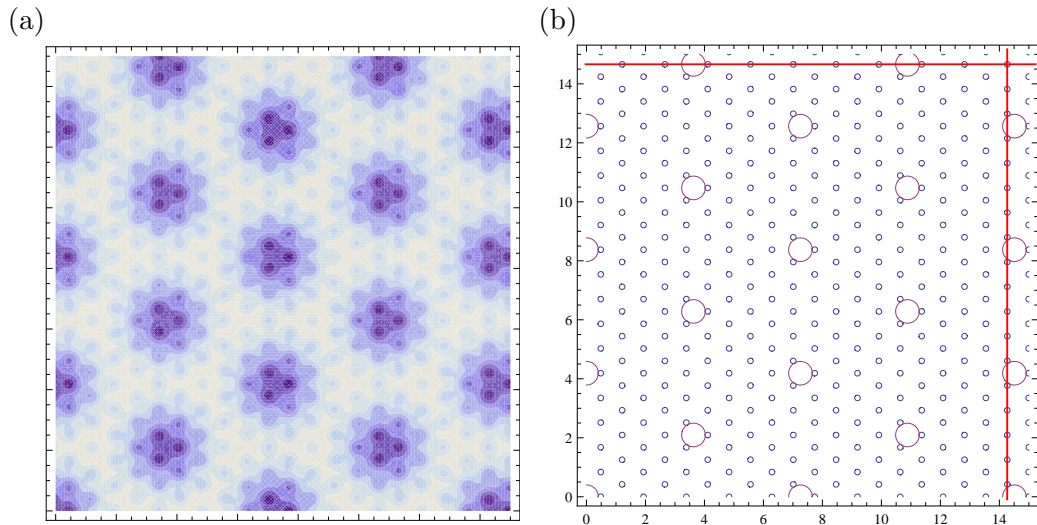


Figure 2.2: The left-hand side is a contour plot of the potential energy $V(x, y)$ in Eq. (2.30) with $(E_0/E'_0)^2 = 3$ and $\lambda/\lambda' = 5$. One unit is equal to $\lambda/2\pi$ in the plots. Red-detuned lasers ($\delta < 0$) are used. The darker is the color, the higher is the potential at the region. The plot on the right-hand side shows the potential maxima produced by the two sets of laser beams individually; the big circles indicate the potential maxima produced by lasers of frequency λ and the small circles indicate the potential maxima produced by lasers of frequency λ'

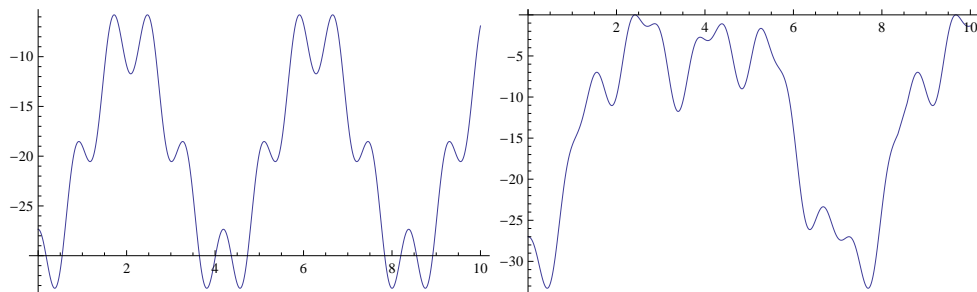


Figure 2.3: The left-hand side shows the potential along the vertical cut-off line in plot (b) of Fig. 2.2; and the right-hand side shows the potential along the horizontal cut-off line in plot (b) of Fig. 2.2.

Remark: This particular construction of optical lattice only works if λ/λ' is an integer. One way of enforcing this condition is to use nonlinear optics and the frequency doubling or tripling effect.

Another possible but less feasible method is to arrange the lasers with a different angle between them, see Fig. 2.4 below. All the laser beams are at the angle of $\pi/3$ with their neighbouring beams.

When $\lambda/\lambda' = 2n/\sqrt{3}$, a different but still interesting lattice can be constructed; see Fig. 2.5. However, the strict requirement of the ratio of λ/λ' makes this lattice

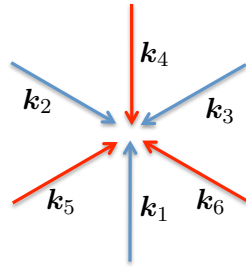


Figure 2.4: Six coplanar laser beams consist of a set of three coherent beams indicated by red arrows and another set of three coherent beams indicated by blue arrows. The angle between neighboring beams is $\pi/3$.

more difficult to obtain experimentally.

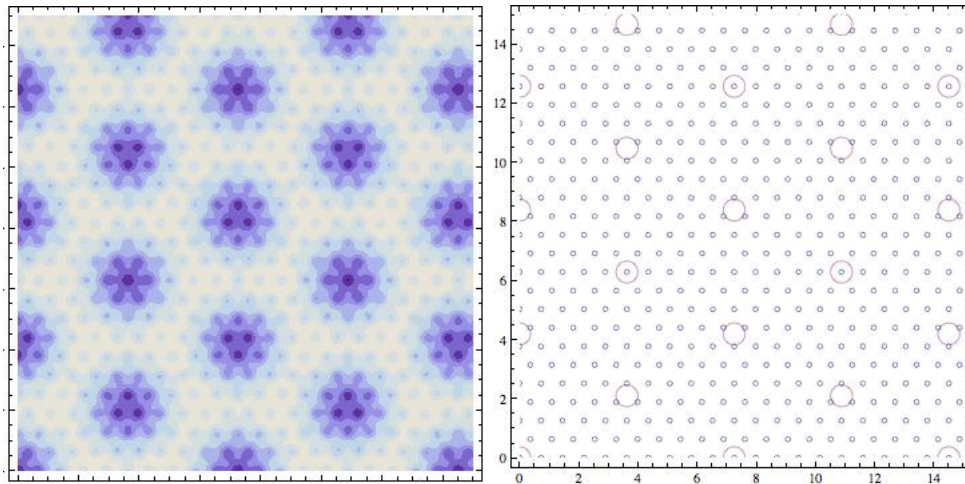


Figure 2.5: The left hand side is a contour plot with lasers set in the configuration shown in Fig. 2.4 with $V_1/V_2 = 3$ and $\lambda/\lambda' = 4/\sqrt{3}$.

In summary, the more feasible physical construction of a possible lattice is to use two sets of three coplanar coherent laser beams and the angle between the beams within each coherent set is $2\pi/3$. By arranging the beams in the configuration shown in Fig. 2.1 and adjusting the phases, an optical trapping potential with the contour plot shown in Fig. 2.2 can be produced. For the potential presented in Fig. 2.2, we chose to keep the phases of the set of beams with the longer wavelength λ to be the same and the phases for the other three beams with the shorter wavelength λ' are $2\pi/3$, 0 , and $-2\pi/3$, but this choice of phases is not unique.

We still have the flexibility of choosing frequencies and intensities of the trapping lasers. The trap depth also depends on the type of atoms put into the lattice. Here we will discuss in more details the optical lattice for spin-1/2 fermionic atom ${}^6\text{Li}$

and spin-1 bosonic atom ^{87}Rb .

^6Li in the optical lattice: Optical properties of the D₁ (D₂) line of ^6Li : [1]

Wavelength	$\lambda = 670.992\text{nm}$ (670.977nm)
Transition frequency	$\omega_0 = 446.790\text{THz}$ (446.800THz)
Natural Linewidth	$\Gamma = 5.872\text{MHz}$ ($\Gamma = 5.872\text{MHz}$)
Atomic Recoil Velocity	$v_{\text{rec}} = 9.887\text{cm/s}$ (9.887cm/s)
Recoil Temperature	$T_{\text{rec}} = 3.536\mu\text{K}$ (3.536 μK)
Saturation Intensity	$I_s = 7.59\text{mW/cm}^2$ (2.54mW/cm ²)

In order to address the RFF qubit individually and minimize scattering between atoms and light for obtaining a long lifetime for the trapped atoms, it would be desirable to have far red-detuned lasers and deeper optical traps. The CO₂ laser is one of the commonly used lasers and it is not difficult to produce high intensity beams with CO₂ lasers. In the following discussion we propose to use the CO₂ laser beams with wavelength 10.6 μm and the beams that can be generated from this wavelength using frequency doubling (or tripling) with standard nonlinear optics. This is just an example, and of course laser fields with other frequencies can also be used.

Let $\lambda = 10.6\mu\text{m}$ and $\lambda' = \lambda/8 = 1.33\mu\text{m}$. That is the distance between atoms within the same RFF qubit is $d = 883\text{nm}$ and the distance between the RFF qubits is $D = 7.1\mu\text{m}$. The recoil energy of the ^6Li D lines is $E_R = \frac{\hbar^2 k^2}{2m} \simeq 4.8 \times 10^{-29}\text{J}$ which corresponds to a recoil temperature of $T_{\text{rec}} \simeq 3.5\mu\text{K}$. To trap the atoms, the depth of the trap needs to be much larger than this kinetic energy, i.e. $\hbar\omega_{\text{trap}} \gg E_R$, where ω_{trap} is the frequency of the trap.

Recall Eq. (2.30), and let

$$g(x, y) = \left| e^{2i\pi y/\lambda} + e^{i\pi(\sqrt{3}x-y)/\lambda} + e^{-i\pi(\sqrt{3}x+y)/\lambda} \right|^2 + \frac{E_0'^2}{E_0^2} \frac{\delta}{\delta'} \left| e^{2i\pi y/\lambda'} + e^{i\pi(\sqrt{3}x-y)/\lambda' - i\frac{2\pi}{3}} + e^{-i\pi(\sqrt{3}x+y)/\lambda' + i\frac{2\pi}{3}} \right|^2, \quad (2.31)$$

Chapter 2. Construction of the RFF qubit

we have the overall potential given by

$$V(x, y) = -\frac{\hbar\Gamma}{8} \frac{\Gamma}{\delta} \frac{I_0}{I_s} g(x, y), \quad (2.32)$$

where $I_0 = \epsilon_0 c E_0^2 / 2$ is the intensity of the low frequency laser beams and $\kappa = \frac{\delta E_0'^2}{\delta' E_0^2}$ is the ratio between the trapping strength from the potential made by the two sets of laser beams individually. For $\kappa = 3$, we expand the function $g(x, y)$ around its global minima, which correspond to global maxima of $V(x, y)$, and fit it with the function $A(x^2 + y^2) + B$. The fitting gives

$$A = 90 \cdot 4\pi^2 / \lambda^2. \quad (2.33)$$

Here we assume the harmonic potential is spherically symmetric and we use the expansion along the direction connecting two atoms. For the harmonic approximation, we have

$$\frac{\hbar\Gamma}{8} \frac{\Gamma}{\delta} \frac{I_0}{I_s} A = \frac{1}{2} m \omega_{\text{trap}}^2 \quad (2.34)$$

and the frequency of the harmonic potential is thus given by $\omega_{\text{trap}} \simeq 1.8 \times 10^2 \sqrt{\frac{I_0}{I_s}}$. For $I_0 = 10^8 \times I_s$, $\omega_{\text{trap}} \simeq 1.8 \text{MHz}$ and the energy separation of the trap $\hbar\omega_{\text{trap}} \simeq 1.8 \times 10^{-28} \text{J}$ ($\cong 13 \mu\text{K}$), which is about five times the recoil energy. The polarizability of ${}^6\text{Li}$ is $\alpha_g = 24.3 \times 10^{-24} \text{cm}^3$, which yields a scattering rate of lower than 10^{-3}s^{-1} at this intensity, corresponds to a scattering time of more than 1000 sec for one photon per atom. Consequently, the recoil heating is negligible for the experiment.

If we define $V_0 = \frac{\hbar\Gamma}{8} \frac{\Gamma}{\delta} \frac{I_0}{I_s}$ as a measure for the trap depth, the trap depth $V_m \simeq 2V_0$ for the potential shown in Fig. 2.2, i.e. $V_m \simeq 1.1 \times 10^{-27} \text{J}$, corresponding to a temperature of about $80 \mu\text{K}$, more than twenty times the recoil energy and deeper than the eighth excited state of the harmonic potential.

The saturation intensity of the D line of ${}^6\text{Li}$ is given by

$$I_s = \frac{1}{\frac{1}{I_{s1}} + \frac{1}{I_{s2}}} = 1.9 \text{mW/cm}^2 \quad (2.35)$$

2.2. Physical carrier and geometry

The numbers above are obtained with the condition $I_0 = 10^8 \times I_s$, and this requires the intensity for the $10.6\mu\text{m}$ CO₂ laser to be

$$I_0 \approx 10^8 \times I_s = 1.9 \times 10^5 \text{W/cm}^2 = 0.19 \text{W}/\mu\text{m}^2, \quad (2.36)$$

and the potential of the low frequency $1.33\mu\text{m}$ lasers to be three times stronger than the potential generated by high frequency lasers, i.e.

$$\frac{I_0}{I'_0} = 3 \frac{\delta}{\delta'} \Rightarrow I'_0 = 0.03 \text{W}/\mu\text{m}^2. \quad (2.37)$$

⁸⁷Rb in the optical lattice: Optical properties of the D₁ (D₂) line of ⁸⁷Rb: [78]

Wavelength	$\lambda = 794.979\text{nm}$ (780.241nm)
Transition frequency	$\omega_0 = 377.107\text{THz}$ (384.230THz)
Natural Linewidth	$\Gamma = 5.750\text{MHz}$ (6.067MHz)
Atomic Recoil Velocity	$v_{\text{rec}} = 5.775\text{mm/s}$ (5.885mm/s)
Recoil Temperature	$T_{\text{rec}} = 348.66\text{nK}$ (361.96nK)
Saturation Intensity	$I_s = 4.49\text{mW/cm}^2$ (2.50mW/cm ²)

Here we analyze the properties of ⁸⁷Rb atoms trapped in the same potential shown in Fig. (2.2) that we studied previously. In general, Rubidium atoms are easier to trap than Lithium atoms because of their low recoil energy, therefore, we can use weaker lasers to achieve a similar effective potential. With the ratio between the laser intensity and the reduced saturation intensity $I_0/I_s = 10^7$, the frequency of the harmonic potential is about $\omega_{\text{trap}} \simeq 1.8/12 = 0.15 \text{MHz}$ and the energy separation of the first excited state and the ground state of the harmonic potential is given by $\hbar\omega_{\text{trap}} \simeq 0.15 \times 10^{-28} \text{J}$ ($\hat{=} 1.1 \mu\text{K}$), which is about three times the recoil energy.

The polarizability of ⁸⁷Rb is $72.6 \times 10^{-24} \text{cm}^3$ (for the D₂ line), which yields a scattering rate below $3 \times 10^{-4} \text{s}^{-1}$ at this intensity and laser frequencies, corre-

Chapter 2. Construction of the RFF qubit

sponding to a scattering time of more than 3000s for one photon per atom. And again we can safely ignore the recoil heating for the experiment. The trap depth is about ten times smaller than the trap depth of the potential for ${}^6\text{Li}$, since the laser intensity is ten times less: $V_m \simeq 1.1 \times 10^{-28}\text{J}$, corresponding to a temperature of about $8\mu\text{K}$, more than twenty times the recoil energy and deeper than the seventh excited state of the harmonic potential.

The saturated intensity of the D line of ${}^{87}\text{Li}$ is given by

$$I_s = \frac{1}{\frac{1}{I_{s1}} + \frac{1}{I_{s2}}} = 1.6\text{mW}/\text{cm}^2 \quad (2.38)$$

The numbers above are obtained under the condition $I_0 = 10^7 \times I_s$, and this requires the intensity for the $10.6\mu\text{m}$ CO_2 laser to be

$$I_0 \approx 10^7 \times I_s = 1.6 \times 10^4\text{W}/\text{cm}^2 = 0.016\text{W}/\mu\text{m}^2, \quad (2.39)$$

and the potential of the low frequency $1.33\mu\text{m}$ lasers to be three times stronger than the potential generated by high frequency lasers, i.e.

$$\frac{I_0}{I'_0} = 3 \frac{\delta}{\delta'} \quad \Rightarrow \quad I'_0 \simeq 0.005\text{W}/\mu\text{m}^2. \quad (2.40)$$

The numbers given above for the trap are for the sample potential presented, which serves the purpose of demonstrating that such a lattice can be had. The properties of the trapping potential strongly depend on the laser intensities I_0 and I'_0 , as well as the light frequency λ and λ' . Other methods for making an array of atomic trios are conceivable as well. This is a hardware issue and details will be determined by the experimental set-up at hand.

2.2.2 Ions in a linear trap and other systems

For the optical lattice set-up above, we aim at making the trio of atoms as symmetric as possible, and thus, the equilateral triangular structure is chosen. However, if we are not insisting on a equilateral triangular symmetry requirement on geometry and

just want to have a convenient way of producing a trio system as our RFF qubit carrier, we can use a linear structure.

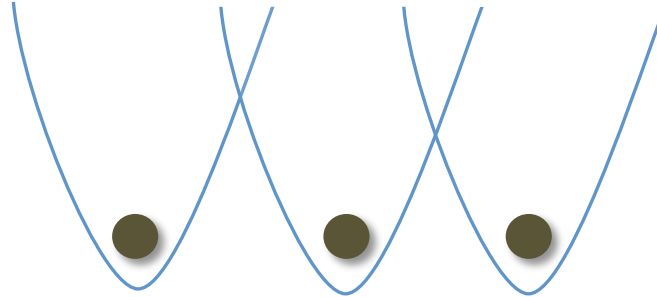


Figure 2.6: Three ions trapped in a linear Paul trap.

The geometry of having three atoms in a line can be easily realized in ion trap experiments, where one can set up a linear Paul trap and fill the trap with identical ions that repel each other; see Fig. 2.6. Certainly one can also produce individual traps for each ion and with the mature technology for trapping ions, the three ions can be arranged in various kind of geometries. Nevertheless, arranging three ions in a linear geometry is the simplest to construct experimentally.

The $^{40}\text{Ca}^+$ ion becomes an obvious candidate for constructing RFF states with an ion trap set-up, not only because its atomic spin is $1/2$ for which the structure of the RFF state is simple, but also because of its wide usage in existing experiments. A neutral ^{40}Ca atom has no nuclear spin, which makes the ground state $^{40}\text{Ca}^+$ ion became a spin- $1/2$ particle with one valence electron. This system could be easier to manipulate, as there is no hyperfine structure for the atoms. The structure of the RFF states from three ground state $^{40}\text{Ca}^+$ ions is the same as the structure of the RFF state made from three ^6Li atoms in its hyperfine ground state. The trapping technology for arranging multiple $^{40}\text{Ca}^+$ ions in a linear geometry is well established and we will not discuss it here.

2.3 Summary

In this chapter, the general structure of the RFF subspace is discussed; and RFF qubit constructed from three spin- $1/2$ particles, RFF qubit constructed from four

Chapter 2. Construction of the RFF qubit

spin-1/2 particles, and RFF qubit constructed from three spin-1 particles are studied explicitly. As examples of physical implementations, we shown that the RFF qubits can be constructed physically with neutral atoms in an optical lattice or ions in a linear Paul trap.

We can also make the RFF states with other physical carriers, for example, three identical diamond N-V centers, three superconducting qubits, three identical nuclei etc.. For each of them, the mathematical construction of the RFF state might be similar, but the physical meanings of spins and manipulation of the RFF qubits could be completely different.

With the current state of the art, for a proof-of-principle experiment with a limited number of RFF qubits, the ion trap experiment would be a good choice. But if we are aiming at a scalable quantum storage or quantum network, using RFF qubits made from neutral atoms in an optical lattice is more feasible and the technology for this type of experiments is developing tremendously fast.

Robustness of the RFF Qubit

For an isolated or perfectly-controlled system, if we prepare the system in a chosen signal state, the system would stay as it was prepared. However, there is neither a truly isolated system nor perfect control in real life, and unfortunately most quantum states are highly entangled with the environment and very fragile against decoherence. Thus, we need smart schemes to protect the quantum states from decoherence. In the previous chapter, we have studied the mathematical structure of the RFF qubit, which uses the particle spin as physical qubit carrier and the constructed logical qubits are rotationally invariant. And the RFF qubits are not affected by any interaction that preserves the total spin operator \mathbf{J} .

Since we are using the spin of the atoms as information carrier, it would be essential to have controllable spin alignment. The stray magnetic field from the environment would be the first problem, because even a small magnetic field might change the alignment completely. To overcome this problem, we apply a uniform magnetic field perpendicular to the plane of the atoms. We should also be more careful when we talk about applying a “uniform” magnetic field, as by applying an overall field we cannot avoid introducing extra noise.

The Hamiltonian of a three spin-1/2 particle system with general noise is given by

$$H = \underbrace{\mu_B B_z (\sigma_{1z} + \sigma_{2z} + \sigma_{3z})}_{H_{\text{bias}}} + \underbrace{\mu_B \sum_{k=1}^3 \mathbf{b}_k(t) \cdot \boldsymbol{\sigma}_k}_{H_{\text{noise}}} + H_{\text{dd}}, \quad (3.1)$$

where B_z is the magnitude of the bias magnetic field and \mathbf{b}_k is the noise at the position of particle k ; the components of all the \mathbf{b}_k are much smaller than the

Chapter 3. Robustness of the RFF Qubit

dominant bias field, i.e. $|\mathbf{b}| \ll B_z$; H_{dd} is the dipole-dipole interaction Hamiltonian between the particles.

Decoherence of the RFF qubit could, therefore, result from spatial inhomogeneities of the stray field. We investigate the effect of such inhomogeneities and demonstrate that the RFF qubits are highly robust: For typical experimental parameters, the magnetic stray fields are of no concern.

Rather, the lifetime of the RFF qubit is limited by the magnetic dipole-dipole interaction among the constituent atoms in conjunction with intrinsic imperfections of the experimental set-up. Our analysis, which uses conservatively estimated parameters and reasonable assumptions about experimental imperfections, shows that a stored qubit maintains a fidelity of 0.9999 or 0.999 for two or seven hours, respectively.

In this section we will first analyze the robustness of the RFF qubit constructed from three spin-1/2 ${}^6\text{Li}$ atoms in an equilateral triangular configuration. In Sec. 3.1, we analyze the robustness of the RFF qubit against decoherence under random stray magnetic fields and conclude that the stray fields are innocuous. We then consider, in Sec. 3.2, the inhomogeneous magnetic dipole fields of the partner atoms for the case of ${}^6\text{Li}$ atoms and find that, in view of unavoidable experimental imperfections, they are the dominating effect that limits the period for which quantum information can be stored. Section 3.3 briefly argues that the RFF system formed by three spin-1/2 constituents is more robust than the system formed by four spin-1/2 constituents. And lastly, the robustness of the RFF qubit constructed from three spin-1 ${}^{87}\text{Rb}$ atoms in an equilateral triangular configuration is discussed qualitatively. We end this chapter with a summary and discussion.

3.1 Three spin-1/2 ${}^6\text{Li}$ in equilateral triangle configuration

3.1.1 Noise model for the magnetic field

The part of the Hamiltonian that describes the effect of the noisy magnetic field on the trio of atoms is given by

$$H_{\text{noise}}(t) = \mu_B \sum_{k=1}^3 \mathbf{b}_k(t) \cdot \boldsymbol{\sigma}_k, \quad (3.2)$$

where μ_B is the Bohr magneton (if necessary multiplied by a gyromagnetic ratio) and $\mathbf{b}_k(t)$ is the randomly fluctuating magnetic stray field that acts on the k th atom. The $\mathbf{b}_k(t)$ s vanish on average,

$$\overline{\mathbf{b}_k(t)} = 0, \quad (3.3)$$

where the overline indicates the stochastic average. Since the atoms are close to each other, the fluctuations in the magnetic fields at the positions of the atoms are not independent but correlated. The dominant part of the noisy magnetic field is the same for all three atoms, and only a small part of the noise affects the atoms differently as a consequence of the nonzero gradient of the magnetic field. Upon denoting the gradient dyadic of the magnetic stray field by $\mathbf{G}(t)$, we have

$$\mathbf{b}_k(t) - \mathbf{b}_l(t) = \mathbf{G}(t) \cdot (\mathbf{r}_k - \mathbf{r}_l), \quad (3.4)$$

where \mathbf{r}_k is the position vector for the k th atom, and $\mathbf{G}(t)$ is assumed to be independent of position within the small volume of relevance. This gradient component is the inhomogeneous noise that gives rise to decoherence of the RFF qubit, while the homogeneous noise is innocuous.

In the noise model considered, every component of the homogeneous stray field and every component of the gradient dyadic has a random gaussian distribution with a vanishing mean. Owing to the Maxwell's equations, the gradient dyadic has

Chapter 3. Robustness of the RFF Qubit

to be symmetric and traceless:

$$\begin{aligned} \mathbf{v}_1 \cdot \mathbf{G}(t) \cdot \mathbf{v}_2 &= \mathbf{v}_2 \cdot \mathbf{G}(t) \cdot \mathbf{v}_1, \\ \sum_{a=x,y,z} \mathbf{e}_a \cdot \mathbf{G}(t) \cdot \mathbf{e}_a &= 0. \end{aligned} \quad (3.5)$$

It follows that the two-time correlation function of the field gradient has the form

$$\begin{aligned} &\overline{\mathbf{v}_1 \cdot \mathbf{G}(t) \cdot \mathbf{v}_2 \mathbf{v}_3 \cdot \mathbf{G}(t') \cdot \mathbf{v}_4} \\ &= (3\mathbf{v}_1 \cdot \mathbf{v}_3 \mathbf{v}_2 \cdot \mathbf{v}_4 + 3\mathbf{v}_1 \cdot \mathbf{v}_4 \mathbf{v}_2 \cdot \mathbf{v}_3 - 2\mathbf{v}_1 \cdot \mathbf{v}_2 \mathbf{v}_3 \cdot \mathbf{v}_4) \frac{1}{4} g^2 e^{-\Gamma_{\text{noise}}|t-t'|} \end{aligned} \quad (3.6)$$

for any four vectors \mathbf{v}_1 , \mathbf{v}_2 , \mathbf{v}_3 , and \mathbf{v}_4 that pick out the components of \mathbf{G} , whereby g^2 is the variance of the gaussian distribution of the diagonal entries of \mathbf{G} , and Γ_{noise} is the decay constant for the temporal correlation. We note that the diagonal elements and the off-diagonal elements of the gradient matrix do not have the same variance:

$$\overline{\mathbf{e} \cdot \mathbf{G}(t) \cdot \mathbf{e} \mathbf{e} \cdot \mathbf{G}(t') \cdot \mathbf{e}} = \frac{4}{3} \overline{\mathbf{e} \cdot \mathbf{G}(t) \cdot \mathbf{e}' \mathbf{e}' \cdot \mathbf{G}(t') \cdot \mathbf{e}'} = g^2 e^{-\Gamma_{\text{noise}}|t-t'|}, \quad (3.7)$$

where \mathbf{e} and \mathbf{e}' are two orthogonal unit vectors. The autocorrelation function for the diagonal components of \mathbf{G} is 4/3 times that of the off-diagonal components, while they have the same correlation time $1/\Gamma_{\text{noise}}$.

As a consequence of Eq. (3.6), the autocorrelation of the field difference of Eq. (3.4) is

$$\begin{aligned} &\overline{\mathbf{v}_1 \cdot (\mathbf{b}_k(t) - \mathbf{b}_l(t)) (\mathbf{b}_k(t') - \mathbf{b}_l(t')) \cdot \mathbf{v}_2} \\ &= \frac{1}{4} g^2 e^{-\Gamma_{\text{noise}}|t'-t|} [3\mathbf{v}_1 \cdot \mathbf{v}_2 \mathbf{r}_{kl}^2 + \mathbf{v}_1 \cdot \mathbf{r}_{kl} \mathbf{r}_{kl} \cdot \mathbf{v}_2] \end{aligned} \quad (3.8)$$

with $\mathbf{r}_{kl} = \mathbf{r}_k - \mathbf{r}_l$. The correlation between the stray fields at the sites of the k th

3.1. Three spin-1/2 ${}^6\text{Li}$ in equilateral triangle configuration

atom and the l th atom is then given by

$$\overline{\mathbf{v}_1 \cdot \mathbf{b}_k(t) \mathbf{b}_l(t') \cdot \mathbf{v}_2} = e^{-\Gamma_{\text{noise}}|t'-t|} \left[b^2 \mathbf{v}_1 \cdot \mathbf{v}_2 - \frac{1}{8} g^2 (3 \mathbf{v}_1 \cdot \mathbf{v}_2 \mathbf{r}_{kl}^2 + \mathbf{v}_1 \cdot \mathbf{r}_{kl} \mathbf{r}_{kl} \cdot \mathbf{v}_2) \right], \quad (3.9)$$

where $b^2 \gg g^2 \mathbf{r}_{kl}^2$ is the strength of the same-site correlation, as we recognize by a look at the $k = l$ version,

$$\overline{\mathbf{v}_1 \cdot \mathbf{b}_k(t) \mathbf{b}_k(t') \cdot \mathbf{v}_2} = b^2 e^{-\Gamma_{\text{noise}}|t'-t|} \mathbf{v}_1 \cdot \mathbf{v}_2. \quad (3.10)$$

Take note that b is an average of magnetic field strength while g describes the magnetic field gradient, they measure different quantities. Consistency with Eq. (3.8) is established by using Eq. (3.9) four times on the right-hand side of

$$\begin{aligned} & \overline{\mathbf{v}_1 \cdot (\mathbf{b}_k(t) - \mathbf{b}_l(t)) (\mathbf{b}_k(t') - \mathbf{b}_l(t')) \cdot \mathbf{v}_2} \\ &= \overline{\mathbf{v}_1 \cdot \mathbf{b}_k(t) \mathbf{b}_k(t') \cdot \mathbf{v}_2} + \overline{\mathbf{v}_1 \cdot \mathbf{b}_l(t) \mathbf{b}_l(t') \cdot \mathbf{v}_2} \\ & \quad - \overline{\mathbf{v}_1 \cdot \mathbf{b}_k(t) \mathbf{b}_l(t') \cdot \mathbf{v}_2} - \overline{\mathbf{v}_1 \cdot \mathbf{b}_l(t) \mathbf{b}_k(t') \cdot \mathbf{v}_2}. \end{aligned} \quad (3.11)$$

Equations (3.3) and (3.9) define the noise model that we use in Sec. 3.1.3 below to derive the master equation by which we then study the effect of the inhomogeneous magnetic stray fields on the RFF qubit in Sec. 3.1.4, and on a single-atom qubit in Sec. 3.1.5. The model is characterized by the three parameters Γ_{noise} , b^2 , and g^2 , which would have to be determined from experimental data when applying the model to an actual laboratory situation. Other noise models are conceivable, in particular if one wants to describe a specific noise source of known characteristics. The noise model of Eqs. (3.3) and (3.9) is generic, however, and quite suitable for the purpose at hand.

In an experimental realization of the three-atom RFF qubit, there will be nearby Helmholtz coils for producing the bias magnetic field at the location of the atoms. Typically, these coils are about 50 cm away and carry currents of about 1 A that are stabilized to 100 ppm or better¹. Now, a current of 0.1 mA at a distance of 0.5 m

¹G. Maslennikov, private communication

gives rise to a magnetic field of 4×10^{-11} T and a field gradient of 8×10^{-11} T/m. Not assuming any fortunate cancellation of the contributions from different coils, the values

$$b = 5 \times 10^{-10} \text{ T} \quad \text{and} \quad g = 10^{-9} \text{ T/m} \quad (3.12)$$

are conservative estimates for these noise parameters. The temporal properties of the fluctuating currents tend to be dominated by the ubiquitous 50 Hz noise that the wires pick up, while high-frequency noise can be filtered out very efficiently, so that a correlation time of

$$1/\Gamma_{\text{noise}} = 20 \text{ ms} \quad (3.13)$$

is a reasonable estimate.

There are many other sources of stray field other than the Helmholtz coils. Electrical wires in the laboratory or metallic objects moving in the vicinity of the laboratory can generate unwanted magnetic field. However, the magnetic field generated in this way are much weaker than the noise in Helmholtz coils, for example, the field generated by a large dump truck passing by at a distance of five meters away from the atoms is of the order 10^{-13} T. Thus, the stray field essentially comes from the Helmholtz coils and we will use the numbers given in Eqs. (3.12) and (3.13) throughout.

3.1.2 Lithium-6

To be specific, but also mindful of possible experiments with two-dimensional confinement [79], we consider the situation of Fig. 3.1: Three ${}^6\text{Li}$ atoms at the corners of an equilateral triangle, perhaps the sites of neighboring maxima of an red-detuned optical potential such as the one discussed in Sec. 2.2.1. Each ${}^6\text{Li}$ atom is in the hyperfine ground state with $f = 1/2$, which is energetically below the $f = 3/2$ hyperfine state by $2\pi\hbar \times 228.2$ MHz; see Fig. 3.2.

We denote the electronic spin operator of the k th atom by \mathbf{s}_k , with $\mathbf{s}_k^2 = 3\hbar^2/4$, so that the energy of the atom trio in an external homogeneous magnetic bias field

3.1. Three spin-1/2 ${}^6\text{Li}$ in equilateral triangle configuration

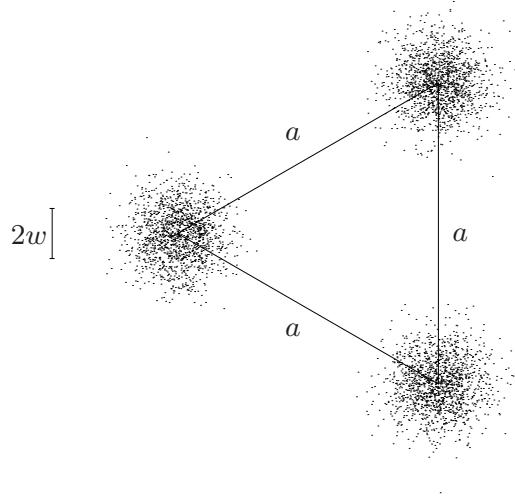


Figure 3.1: Three ${}^6\text{Li}$ atoms are trapped at the corners of an equilateral triangle. The probability clouds indicate the center-of-mass distributions whose spread w is about one-sixteenth of a , the distance between the atoms.

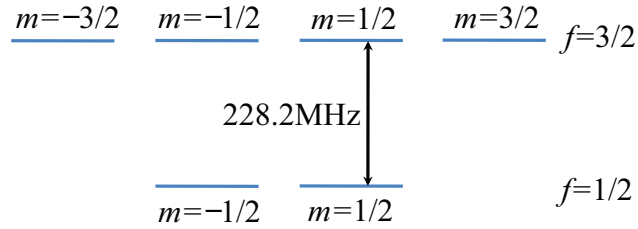


Figure 3.2: Ground-state hyperfine levels of the neutral ${}^6\text{Li}$ atom. The $f = 3/2$ quartet is separated from the $f = 1/2$ doublet by a transition frequency of 228.2MHz. Three ${}^6\text{Li}$ atoms confined to their $f = 1/2$ ground states serve as the spin-1/2 particles from which the RFF qubit is constructed.

\mathbf{b}_0 is given by

$$H_{\text{bias}} = \sum_{k=1}^3 2 \frac{\mu_B}{\hbar} \mathbf{s}_k \cdot \mathbf{b}_0, \quad (3.14)$$

where we take the value of 2 for the gyromagnetic factor of the electron. With each atom confined to its $f = 1/2$ ground state, this becomes

$$H_{\text{bias}} = \sum_{k=1}^3 \left(-\frac{2}{3} \right) \frac{\mu_B}{\hbar} \mathbf{F}_k \cdot \mathbf{b}_0, \quad (3.15)$$

where $-2/3$ is the gyromagnetic ratio and $\mathbf{F}_k = (\hbar/2)\boldsymbol{\sigma}_k$ is the atomic angular momentum for k th particle in the present context; the magnetic moment of the spin-1 nucleus is ignored. As indicated, here we identify the Pauli operators of

Chapter 3. Robustness of the RFF Qubit

Eqs. (2.1), (2.9), (2.13), or (3.2).

We choose the bias field in the z -direction, perpendicular to the xy -plane in which the atoms are located, $\mathbf{b}_0 = -B_0 \mathbf{e}_z$, and express its strength in terms of the circular frequency ω_0 : $\hbar\omega_0 = 2\mu_B B_0/3$; then

$$H_{\text{bias}} = \frac{1}{2} \hbar\omega_0 \sum_{k=1}^3 \sigma_{kz} = \hbar\omega_0 J_z. \quad (3.16)$$

The coupling of the $f = 1/2$ and the $f = 3/2$ multiplets by the bias field is ignored, which is permissible if the field is weak on the scale set by the energy difference, that is: $\omega_0 \ll 2\pi \times 228.2$ MHz. For example, this condition is met for the modest field strength of $B_0 = 2$ mG = 2×10^{-7} T, when $\omega_0 = 2\pi \times 2$ kHz is a thousandth of a percent of the transition frequency, and transition probabilities are of the order of $(10^{-5})^2 = 10^{-10}$.

We need the bias field to fight the ‘‘internal magnetic pollution’’ that originates in the magnetic dipole-dipole interaction between the spin-1/2 atoms. In terms of the electronic spin operators, this interaction energy is

$$H_{\text{dd}} = \frac{\mu_0}{4\pi} \left(\frac{2\mu_B}{\hbar} \right)^2 \frac{1}{a^3} \sum_{(k,l)} (\mathbf{s}_k \cdot \mathbf{s}_l - 3\mathbf{s}_k \cdot \mathbf{e}_{kl} \mathbf{e}_{kl} \cdot \mathbf{s}_l), \quad (3.17)$$

where $a = |\mathbf{r}_{kl}|$ is the common distance between the atoms at the corners of the equilateral triangle, $\mathbf{e}_{kl} = \mathbf{r}_{kl}/a$ is the unit vector that points from the k th to the l th atom, and the summation is over the three pairs. As in the transition from Eq. (3.14) to Eq. (3.15), the restriction to the $f = 1/2$ ground state amounts to the replacement

$$\mathbf{s}_k \rightarrow -\frac{1}{3} \mathbf{F}_k = -\frac{\hbar}{6} \boldsymbol{\sigma}_k, \quad (3.18)$$

which turns Eq. (3.17) into

$$H_{\text{dd}} = \frac{1}{3} \hbar\Omega \sum_{(k,l)} (\boldsymbol{\sigma}_k \cdot \boldsymbol{\sigma}_l - 3\boldsymbol{\sigma}_k \cdot \mathbf{e}_{kl} \mathbf{e}_{kl} \cdot \boldsymbol{\sigma}_l) \quad (3.19)$$

3.1. Three spin-1/2 ${}^6\text{Li}$ in equilateral triangle configuration

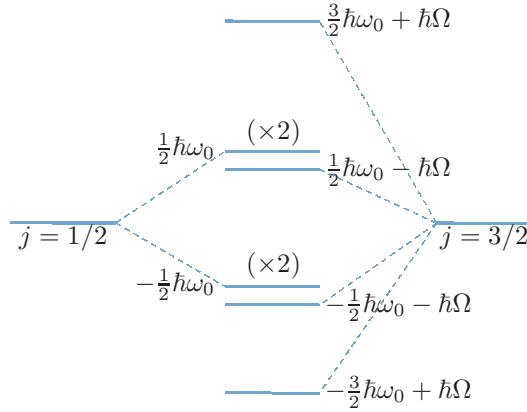


Figure 3.3: Level scheme for the effective three-atom Hamiltonian of Eq. (3.22). The separations are not drawn to scale: $\hbar\omega_0$ is many orders of magnitude larger than $\hbar\Omega$. The two $J = 1/2$ levels are degenerate doublets; this degeneracy is exploited for the encoding of the robust signal qubit.

with

$$\hbar\Omega = \frac{\mu_0 \mu_B^2}{4\pi 3a^3}. \quad (3.20)$$

For a distance of $a = 883$ nm (see Sec. 2.2.1), we have $\Omega = 2\pi \times 6$ mHz, smaller than ω_0 by a factor of 3×10^5 , so that the transitions induced by H_{dd} are completely suppressed in the presence of a 2 mG bias field. Therefore, only the part of H_{dd} that commutes with H_{bias} of Eq. (3.16) is relevant, and we arrive at

$$H_{\text{dd}} = \frac{1}{3}\hbar\Omega (3J_z^2 - \mathbf{J}^2) \quad (3.21)$$

as the effective Hamiltonian for the magnetic dipole-dipole interaction among the atoms. Note that this H_{dd} vanishes in the $J = 1/2$ sector where the signal and idler qubits reside.

The combined effective Hamiltonian

$$H_{\text{bias}} + H_{\text{dd}} = \hbar\omega_0 J_z + \frac{1}{3}\hbar\Omega (3J_z^2 - \mathbf{J}^2) \quad (3.22)$$

has the non-degenerate eigenvalues $\pm\frac{3}{2}\hbar\omega_0 + \hbar\Omega$ and $\pm\frac{1}{2}\hbar\omega_0 - \hbar\Omega$ in the $J = 3/2$ sector, and the two-fold eigenvalues $\pm\frac{1}{2}\hbar\omega_0$ in the $J = 1/2$ sector; see Fig. 3.3. The energy differences correspond to transition frequencies of about $1, 2, 3 \times \omega_0/(2\pi)$, which are in the few-kHz range, and to transition frequency $\Omega/(2\pi)$, which is 6 mHz,

Chapter 3. Robustness of the RFF Qubit

if we continue to use the numbers found above. There is a clear separation of time scales, then, and noise with a correlation time $1/\Gamma_{\text{noise}}$ in the order of 20 ms — which we regard as a typical number, see above — would not be able to induce transitions between the states separated by several $\hbar\omega_0$ while it will mix the states that are separated by $\hbar\Omega$ only or not at all.

There are, of course, stray fields in the radio frequency range but their sources (the radio stations) are far away so that the gradient parameter g is extremely small, and noise of this kind is of no concern. By contrast, noise originating in nearby sources — current carrying wires in the vicinity of the laboratory, say — is relevant.

3.1.3 Master equation

In view of this separation of time scales — very fast ω_0 -oscillations and very slow Ω -oscillations on the scale set by the correlation time $1/\Gamma_{\text{noise}}$ of the random stray field — we can use master equation techniques to account for the net effect of the noise. For the purpose of deriving the Lindblad operators of the master equation, we put H_{dd} of Eq. (3.22) aside and use an interaction picture in which the fast ω_0 -oscillations of H_{bias} are transformed away. The statistical operator in this interaction picture, denoted by $\tilde{\varrho}(t)$, then obeys the von Neumann equation of motion

$$\frac{\partial}{\partial t}\tilde{\varrho}(t) = \frac{i}{\hbar}[\tilde{\varrho}(t), \tilde{H}_{\text{noise}}(t)] \quad (3.23)$$

with

$$\begin{aligned} \tilde{H}_{\text{noise}}(t) &= e^{iH_{\text{bias}}t/\hbar} H_{\text{noise}}(t) e^{-iH_{\text{bias}}t/\hbar} \\ &= e^{i\omega_0 t J_z} \left(-\frac{\mu_B}{3}\right) \sum_{k=1}^3 \mathbf{b}_k(t) \cdot \boldsymbol{\sigma}_k e^{-i\omega_0 t J_z}, \end{aligned} \quad (3.24)$$

where the replacement $\mu_B \rightarrow -\mu_B/3$ accounts for the gyromagnetic ratio that we first met in the transition from Eq. (3.14) to Eq. (3.15).

The unitary evolution operator $U(T)$ links $\tilde{\varrho}(T)$ to the initial statistical operator

3.1. Three spin-1/2 ${}^6\text{Li}$ in equilateral triangle configuration

$\tilde{\varrho}(0)$,

$$\tilde{\varrho}(T) = U(T)\tilde{\varrho}(0)U(T)^\dagger. \quad (3.25)$$

We solve the Lippmann–Schwinger equation

$$U(T) = 1 - \frac{i}{\hbar} \int_0^T dt \tilde{H}_{\text{noise}}(t)U(t) \quad (3.26)$$

to second order in H_{noise} ,

$$U(T) \simeq 1 - i\phi_1(T) - \frac{1}{2}\phi_1(T)^2 - i\phi_2(T), \quad (3.27)$$

where the hermitian phases $\phi_1(T)$ and $\phi_2(T)$ are given by

$$\begin{aligned} \phi_1(T) &= \frac{1}{\hbar} \int_0^T dt \tilde{H}_{\text{noise}}(t), \\ \phi_2(T) &= \frac{1}{2i\hbar^2} \int_0^T dt \int_0^t dt' [\tilde{H}_{\text{noise}}(t), \tilde{H}_{\text{noise}}(t')]. \end{aligned} \quad (3.28)$$

To second order in H_{noise} , then, we have

$$\tilde{\varrho}(T) = \tilde{\varrho}(0) + i[\tilde{\varrho}(0), \phi_1(T) + \phi_2(T)] + \frac{1}{2}[\phi_1(T), [\tilde{\varrho}(0), \phi_1(T)]], \quad (3.29)$$

and the stochastic averaging of Sec. 3.1.1 turns this into

$$\tilde{\rho}(T) = \tilde{\rho}(0) + i[\tilde{\rho}(0), \overline{\phi_2(T)}] + \frac{1}{2}[\phi_1(T), \overline{[\tilde{\rho}(0), \phi_1(T)]}], \quad (3.30)$$

where $\rho(t) = \overline{\varrho(t)}$ and the initial statistical operator is not affected by the averaging or the transition to the interaction picture: $\tilde{\varrho}(0) = \overline{\tilde{\varrho}(0)} = \tilde{\rho}(0) = \rho(0)$. Note that $\overline{\phi_1(T)} = 0$ follows from Eq. (3.3).

We take a closer look at the ‘‘sandwich term’’ in the double commutator,

$$\overline{\phi_1(T)\tilde{\rho}(0)\phi_1(T)} = \left(\frac{\mu_B}{3\hbar}\right)^2 \sum_{k,l=1}^3 \int_0^T dt \int_0^T dt' \tilde{\sigma}_k(t) \cdot \overline{\mathbf{b}_k(t)\tilde{\rho}(0)\mathbf{b}_l(t')} \cdot \tilde{\sigma}_l(t'). \quad (3.31)$$

Here, T is much longer than the correlation time of the noise, $\Gamma_{\text{noise}}T \gg 1$, so that

Chapter 3. Robustness of the RFF Qubit

there are very many cycles of the ω_0 -oscillation in a short t -interval. Therefore, the rapidly oscillating terms in $\tilde{\sigma}_k(t)$ do not contribute to the t -integration and the replacement

$$\tilde{\sigma}_k(t) = e^{i\omega_0 t J_z} \sigma_k e^{-i\omega_0 t J_z} \rightarrow \sigma_k \cdot \mathbf{e}_z \mathbf{e}_z = \sigma_{kz} \mathbf{e}_z \quad (3.32)$$

is permissible; and likewise for $\tilde{\sigma}_l(t')$. This ‘‘rotating-wave approximation’’ takes us to

$$\begin{aligned} \overline{\phi_1(T) \tilde{\rho}(0) \phi_1(T)} &= \left(\frac{\mu_B}{3\hbar}\right)^2 \sum_{k,l=1}^3 \sigma_{kz} \tilde{\rho}(0) \sigma_{lz} \int_0^T dt \int_0^T dt' \overline{\mathbf{e}_z \cdot \mathbf{b}_k(t) \mathbf{b}_l(t') \cdot \mathbf{e}_z} \\ &= \left(\frac{\mu_B}{3\hbar}\right)^2 \sum_{k,l=1}^3 \sigma_{kz} \tilde{\rho}(0) \sigma_{lz} \left[b^2 - \frac{3}{8} (ga)^2 (1 - \delta_{kl}) \right] \int_0^T dt \int_0^T dt' e^{-\Gamma_{\text{noise}} |t-t'|} \end{aligned} \quad (3.33)$$

after using Eq. (3.9) for $\mathbf{v}_1 = \mathbf{v}_2 = \mathbf{e}_z$, $\mathbf{r}_{kl} \cdot \mathbf{e}_z = 0$, and $r_{kl}^2 = (1 - \delta_{kl})a^2$. For $\Gamma_{\text{noise}} T \gg 1$, the remaining double integral equals $2T/\Gamma_{\text{noise}}$, and we arrive at

$$\overline{\phi_1(T) \tilde{\rho}(0) \phi_1(T)} = \frac{T}{4\tau} \sum_{k=1}^3 \sigma_{kz} \tilde{\rho}(0) \sigma_{kz} + \frac{T}{\tau'} J_z \tilde{\rho}(0) J_z \quad (3.34)$$

with the time constants

$$\tau = 3\Gamma_{\text{noise}} \left(\frac{\hbar}{\mu_B ga} \right)^2 \quad (3.35)$$

and

$$\tau' = \frac{3(ga)^2}{8b^2 - 3(ga)^2} \tau. \quad (3.36)$$

Since $ga \ll b$, we have $\tau' \ll \tau$, and the numbers of Sec. 3.1.2, that is: $1/\Gamma_{\text{noise}} = 20$ ms and $ga = 9 \times 10^{-16}$ T, give $\tau = 2 \times 10^{10}$ s — an amazingly long time.

The replacement of Eq. (3.32) gives a vanishing commutator in the double integral for $\phi_2(T)$ in Eq. (3.28), so that $\overline{\phi_2(T)} = 0$ in Eq. (3.30). In summary, then, we have

$$\tilde{\rho}(T) \simeq \tilde{\rho}(0) + T \mathcal{L} \tilde{\rho}(0) \quad (3.37)$$

with the Lindblad operator \mathcal{L} given by

$$\mathcal{L}\rho = \frac{1}{8\tau} \sum_{k=1}^3 [\sigma_{kz}, [\rho, \sigma_{kz}]] + \frac{1}{2\tau'} [J_z, [\rho, J_z]], \quad (3.38)$$

3.1. Three spin-1/2 ${}^6\text{Li}$ in equilateral triangle configuration

and the master equation in the interaction picture is simply

$$\frac{\partial}{\partial t} \tilde{\rho}(t) = \mathcal{L} \tilde{\rho}(t). \quad (3.39)$$

Upon getting out of the interaction picture, and re-introducing the slow Ω -oscillations of H_{dd} , this gives us the master equation

$$\frac{\partial}{\partial t} \rho(t) = \frac{i}{\hbar} [\rho(t), H_{\text{bias}} + H_{\text{dd}}] + \mathcal{L} \rho(t) \quad (3.40)$$

for the evolution of the coarse-grain, stochastically averaged, statistical operator $\rho(t)$.

We note in passing that this master equation could alternatively be derived with standard textbook methods, such as those that proceed from the Redfield equation, here:

$$\frac{\partial}{\partial T} \tilde{\rho}(T) = \frac{1}{\hbar^2} \int_0^T dt \overline{[\tilde{H}_{\text{noise}}(T), [\tilde{\rho}(t), \tilde{H}_{\text{noise}}(t)]]}, \quad (3.41)$$

and invoke the Born–Markov approximation and the rotating-wave approximation to arrive at Eq. (3.39). For details of this procedure, see Sec. (3.2) in Ref. [80], for example.

In view of the diagonal form of the Lindblad operator in Eq. (3.38), the expectation value $\langle A \rangle_t = \text{tr} \{A \rho(t)\}$ of an observable A obeys the differential equation

$$\frac{d}{dt} \langle A \rangle_t = \frac{1}{i\hbar} \langle [A, H_{\text{bias}} + H_{\text{dd}}] \rangle_t + \langle \mathcal{L} A \rangle_t. \quad (3.42)$$

For observables that commute with J_z , which is the case for all operators related to the signal qubit, only the \mathbf{J}^2 part of H_{dd} and the τ -term of \mathcal{L} matter, and then the simpler equation

$$\frac{d}{dt} \langle A \rangle_t = \frac{i\Omega}{3} \langle [A, \mathbf{J}^2] \rangle_t + \frac{1}{4\tau} \sum_{k=1}^3 \langle \sigma_{kz} A \sigma_{kz} \rangle_t - \frac{3}{4\tau} \langle A \rangle_t \quad (3.43)$$

applies. In particular we have

$$\langle f(J_z) \rangle_t = \langle f(J_z) \rangle_0 \quad (3.44)$$

for all functions of J_z . The product

$$\Omega\tau = \frac{\mu_0}{4\pi} \frac{\hbar\Gamma_{\text{noise}}}{a^3(ga)^2} \propto a^{-5} \quad (3.45)$$

states the relative size of the time constants in Eq. (3.43). It depends rather strongly on the distance a between the atoms; we have $\Omega\tau \simeq 10^9$ for the values used earlier ($a = 883$ nm, $1/\Gamma_{\text{noise}} = 20$ ms, $ga = 9 \times 10^{-16}$ T).

3.1.4 Time dependence of RFF-qubit variables

By making use of Eq. (3.43), we can now calculate $\langle P_{J=1/2} \rangle_t$, the probability of finding the three-atom system in the $J = 1/2$ sector at time t , and the time-dependent expectation values of the RFF-qubit Pauli operators of Eqs. (2.13) and (2.12). The outcome is

$$\begin{aligned} \langle P_{J=1/2} \rangle_t &= \frac{1}{3} \left(2 + e^{-t/\tau} \right), \\ \langle \Sigma_1 + i\Sigma_2 \rangle_t &= e^{-\frac{2}{3}t/\tau} \langle \Sigma_1 + i\Sigma_2 \rangle_0, \\ \langle \Sigma_3 \rangle_t &= e^{-t/\tau} \langle \Sigma_3 \rangle_0, \end{aligned} \quad (3.46)$$

if the system is initially in the $J = 1/2$ sector, where the idler and signal qubits reside. The expressions for $\langle P_{J=1/2} \rangle_t$ and $\langle \Sigma_3 \rangle_t$ are exact solutions of the respective versions of Eq. (3.43), and the result for $\langle \Sigma_1 + i\Sigma_2 \rangle_t$ is an approximation that neglects terms of relative size $(\Omega\tau)^{-2} \simeq 10^{-18}$.

Supporting evidence is provided by numerical simulations [81]. These are done by generating a RFF state at initial time $t = 0$ and letting the state evolve with stochastic random noisy magnetic fields on the three atoms. All components of the noise are generated randomly at each time step from a gaussian distribution, and the Maxwell's equations are strictly imposed on the magnetic fields. Figure 3.4

3.1. Three spin-1/2 ${}^6\text{Li}$ in equilateral triangle configuration

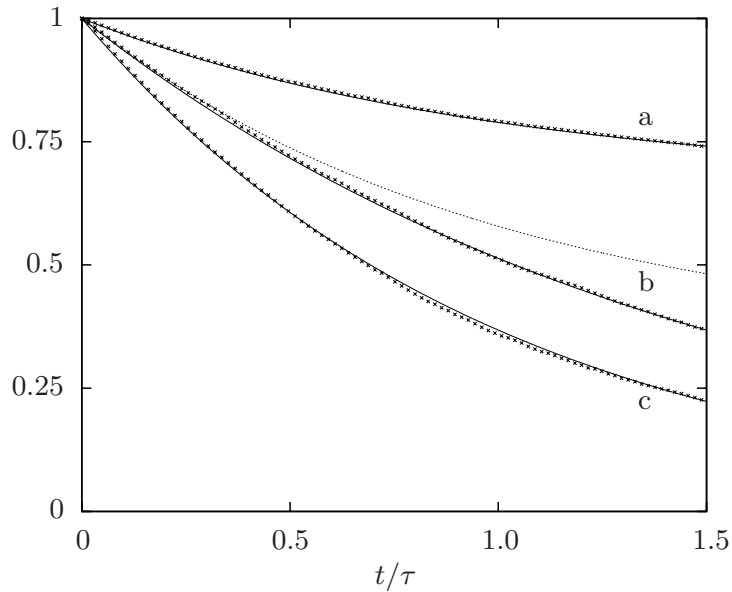


Figure 3.4: Comparison of the data from a numerical simulation with the analytical results of Eqs. (3.46). Curve “a” displays $\langle P_{J=1/2} \rangle_t$, curves “b” show $\langle \Sigma_1 \rangle_t$ for $\langle \Sigma_1 \rangle_0 = 1$, and curve “c” is for $\langle \Sigma_3 \rangle_t$ with $\langle \Sigma_3 \rangle_0 = 1$. The crosses are from a simulation of the dynamics, averaged over 1000 runs. The solid-line curves represent the analytical results of Eqs. (3.46). The dotted “b” curve shows what one would get for $\langle \Sigma_1 \rangle_t$ if Ω vanished rather than being large on the scale set by τ ; we observe that the inter-atomic dipole-dipole interaction accelerates the decay of $\langle \Sigma_1 \rangle_t$. For the parameter values used throughout the paper, the time range is 3×10^{10} s (roughly 1000 years); see Eq. (3.35) for the value of τ .

shows both the analytical and the numerical results of the evolution of the RFF qubit for an arbitrary initial RFF state. We note that there is very good agreement between the results of the simulation and the analytical solution of the master equation.

Quantum information stored in the RFF qubit is degraded substantially only after a good fraction of τ has elapsed. But since $\tau = 2 \times 10^{10}$ s is more than 600 years, we conclude that the effect of the inhomogeneous magnetic stray fields is of absolutely no concern. Put differently, the experimenter need not take special measures to suppress the stray fields.

3.1.5 Compare to decoherence of a single-atom qubit

If — rather than making good use of the three-atom RFF signal qubit — one encoded quantum information into the $f = 1/2$ ground state of a single ${}^6\text{Li}$ atom, the effect of the random magnetic stray field would be described by the single-atom

Chapter 3. Robustness of the RFF Qubit

master equation

$$\frac{\partial}{\partial t}\rho(t) = \frac{i\omega_0}{2}[\rho(t), \sigma_z] + \frac{1}{4\tau_1}[\sigma_z, [\rho(t), \sigma_z]] \quad (3.47)$$

with

$$\tau_1 = \frac{2\tau\tau'}{\tau + \tau'} = \frac{3}{4}\left(\frac{ga}{b}\right)^2\tau = \Gamma_{\text{noise}}\left(\frac{3\hbar}{2\mu_B b}\right)^2 \ll \tau. \quad (3.48)$$

The resulting time-dependent expectation values are

$$\begin{aligned} \langle \sigma_x + i\sigma_y \rangle_t &= e^{i\omega_0 t} e^{-t/\tau_1} \langle \sigma_x + i\sigma_y \rangle_0, \\ \langle \sigma_z \rangle_t &= \langle \sigma_z \rangle_0, \end{aligned} \quad (3.49)$$

so that the quantum information can be stored for a fraction of time τ_1 .

The bias field stabilizes the z component: It separates the spin-up and spin-down states in energy by $\hbar\omega_0$ and so prevents transitions between them — this is, of course, the essence of the rotating-wave approximation of Eq. (3.32). Therefore, one could encode a *classical* bit in a single spin-1/2 atom and protect it from the stray magnetic field².

Without the bias field, the master equation

$$\frac{\partial}{\partial t}\rho(t) = \frac{1}{4\tau_1}[\boldsymbol{\sigma} \cdot, [\rho(t), \boldsymbol{\sigma}]] \quad (3.50)$$

applies. Its solution

$$\rho(t) = \frac{1}{2}(1 + e^{-2t/\tau_1}\langle \boldsymbol{\sigma} \rangle_0 \cdot \boldsymbol{\sigma}) \quad (3.51)$$

shows that the state decays toward the completely mixed state with a life time of $\tau_1/2$. It follows that, in addition to preserving the z component, the bias field also slows down the decay of the x and y components by a factor of two.

For the example used in Sec. 3.1.1 — a fluctuating 0.1 mA current in a wire at a distance of 50 cm — we have $ga/b \simeq 10^{-6}$ and obtain $\tau_1 \simeq 2 \times 10^{-12}\tau$. Even

²When using two atoms, the bias field separates the $\uparrow\uparrow$ and $\downarrow\downarrow$ states from the $\uparrow\downarrow$ and $\downarrow\uparrow$ states, which have approximately the same energy and can be used for the storage of a qubit. A life time of several seconds was achieved in an ion-trap experiment [?].

3.1. Three spin-1/2 ${}^6\text{Li}$ in equilateral triangle configuration

for the very large value of τ found above, $\tau \simeq 2 \times 10^{10}$ s, the lifetime of the single-atom qubit is quite short: $\tau_1 \simeq 40$ ms. Clearly, the well-protected RFF qubit of the three-atom system has an advantage over the unprotected single-atom qubit: The stray fields, which are of no concern for the RFF qubit, have a devastating effect on the single-atom qubit.

More relevant than the lifetime τ_1 is the duration of the initial period of high fidelity. The general fidelity between two state ρ_1 and ρ_2 is defined as

$$F(\rho_1, \rho_2) = \text{tr} \left\{ \sqrt{\sqrt{\rho_1} \rho_2 \sqrt{\rho_1}} \right\}. \quad (3.52)$$

With this definition, the fidelity of two single-qubit states, specified by their respective Pauli vectors, is given by

$$F(\rho_1, \rho_2) = \sqrt{\frac{1}{2}(1 + \mathbf{s}_1 \cdot \mathbf{s}_2) + \frac{1}{2}\sqrt{1 - \mathbf{s}_1^2}\sqrt{1 - \mathbf{s}_2^2}}. \quad (3.53)$$

For the fidelity $F(t) \equiv F(\rho(t), \rho(0))$ between the initial qubit state and the state at later time t , we have the lower bound

$$F(t) \geq \begin{cases} \sqrt{\frac{1}{2}(1 + e^{-t/\tau_1} \cos(\omega_0 t))} & \text{for Eq. (3.47)} \\ \sqrt{\frac{1}{2}(1 + e^{-2t/\tau_1})} & \text{for Eq. (3.50)} \end{cases} \quad (3.54)$$

so that a fidelity of, say, 0.999 is only guaranteed for a fraction of a millisecond. By contrast, the RFF qubit would have a fidelity of 0.9999 or better for several months if nothing mattered except for the magnetic stray field.

We note that the ratio of τ_1 and τ is solely determined by the comparison of the distance between the atoms and the distance of the atoms from the source of the noise, for which we have been using 883 nm and 50 cm, respectively, implying $ga/b = 900 \times 10^{-9}/50 \times 10^{-2} \simeq 2 \times 10^{-6}$. Therefore, the conclusion that $\tau_1/\tau \simeq (2 \times 10^{-6})^2 \simeq 10^{-12}$ holds irrespective of the actual physical process that generates the stray magnetic field as long as the noise source is half a meter away.

3.2 Non-ideal geometry

Two assumptions of ideal geometry enter the derivation of the effective Hamiltonian for the dipole-dipole interaction in Eq. (3.21): That the atoms are located at the corners of a perfect equilateral triangle; and that the bias field is exactly perpendicular to the plane of the atoms. Let us now consider the consequences of imperfections on both counts.

3.2.1 Center-of-mass probability distribution

As illustrated by the probability clouds in Fig. 3.1, the atoms do not have definite positions but rather probability distributions for their centers of mass, given by the ground-state wave functions of the trapping potentials. We assume that, for the purpose at hand, the respective trapping potentials are reasonably well approximated by isotropic harmonic oscillator potentials, so that each atom has a gaussian probability distribution,

$$p(\mathbf{r}) = (\sqrt{2\pi} w)^{-3/2} e^{-\frac{1}{2}r^2/w^2}, \quad (3.55)$$

where $\mathbf{r} = 0$ is the position of the trap center and w is the width of the gaussian. The oscillator frequency $\omega_{\text{trap}}/(2\pi)$ of the trap is related to w and the mass M of the atom by

$$\omega_{\text{trap}} = \frac{\hbar}{2Mw^2}, \quad (3.56)$$

which is obtained by fitting the potential around the bottom of the trap to a harmonic-oscillator potential. For the potential of Sec. 2.2.1, $\omega_{\text{trap}} = 2\pi \times 0.3$ MHz, so that the width of the gaussian wave function is

$$w = \sqrt{\frac{\hbar}{2m\omega_{\text{trap}}}} \approx 53\text{nm}, \quad (3.57)$$

Accordingly, here, earlier in Fig. 3.1, and in what follows, we take the width w to be about one-sixteenth of the distance a between the atoms.

When comparing the restoring force of the oscillator potential, $M\omega_{\text{trap}}^2 r$, with

the dipole forces exerted by the partner atoms, $\hbar\Omega/a$, we find that the balance of forces would shift the equilibrium position by an amount of the order of

$$\frac{\hbar\Omega}{M\omega_{\text{trap}}^2 a} = \frac{2\Omega}{\omega_{\text{trap}}} \frac{w^2}{a} \simeq 2 \times 10^{-9} w, \quad (3.58)$$

which is a completely negligible effect. We also note that, depending on the joint spin state of the three atoms, the shift is in different directions, and the center-of-mass degrees of freedom get entangled with the spin degrees of freedom but, since the shift is such a tiny fraction of the position spread w , this entanglement is so weak that it can be safely ignored. As a consequence, the center-of-mass motion is decoupled from the dynamics of the spins, and probability distributions as in Eq. (3.55) apply to the atoms at all times.

The total statistical operator for the three-atom system is then the product $\varrho(t)\varrho_{\text{CM}}$ of the spin factor $\varrho(t)$ of Sec. 3.1.3 and a static center-of-mass factor ϱ_{CM} . The von Neumann equation for $\varrho(t)$ is obtained by tracing over the center-of-mass variables,

$$\frac{\partial}{\partial t}\varrho(t) = \frac{i}{\hbar}[\varrho(t), \text{tr}\{\varrho_{\text{CM}}H_{\text{tot}}\}], \quad (3.59)$$

where $H_{\text{tot}} = H_{\text{CM}} + H_{\text{dd}} + H_{\text{bias}} + H_{\text{noise}}$ is the total Hamiltonian. Of its four terms, the dipole-dipole interaction energy H_{dd} and the noise part H_{noise} involve both spin variables and center-of-mass variables. In view of the lesson learned in Sec. 2, however, there is no need to deal with H_{noise} in detail.

We consider the center-of-mass average of the contribution from atoms 1 and 2 to H_{dd} ,

$$\text{tr}\left\{\varrho_{\text{CM}}H_{\text{dd}}^{(12)}\right\} = -\frac{\mu_0}{4\pi}\left(\frac{\mu_{\text{B}}}{3}\right)^2\boldsymbol{\sigma}_1\cdot\nabla_{\mathbf{a}}\boldsymbol{\sigma}_2\cdot\nabla_{\mathbf{a}}\int(d\mathbf{r}_1)(d\mathbf{r}_2)\frac{p_1(\mathbf{r}_1)p_2(\mathbf{r}_2)}{|\mathbf{a}-\mathbf{r}_1+\mathbf{r}_2|}, \quad (3.60)$$

where \mathbf{a} is the vector from the trap center for atom 1 to the trap center for atom 2. Allowing for different widths of the two gaussians, the integration yields

$$\int(d\mathbf{r}_1)(d\mathbf{r}_2)\frac{p_1(\mathbf{r}_1)p_2(\mathbf{r}_2)}{|\mathbf{a}-\mathbf{r}_1+\mathbf{r}_2|} = \frac{1}{a}\text{erf}\left(\frac{a}{\sqrt{2w_1^2+2w_2^2}}\right) \quad (3.61)$$

with the standard error function $\text{erf}(\cdot)$. Its asymptotic form

$$\text{erf}(z) = 1 - \frac{e^{-z^2}}{\sqrt{\pi} z} + \dots \quad \text{for } z \gg 1 \quad (3.62)$$

tells us that the right hand side of Eq. (3.61) differs from $1/a$ by a term of relative size 10^{-28} for $w_1 \simeq w_2 \simeq a/16$. It follows that

$$\text{tr} \left\{ \varrho_{\text{CM}} H_{\text{dd}}^{(12)} \right\} = \frac{\mu_0}{4\pi} \left(\frac{\mu_{\text{B}}}{3} \right)^2 \boldsymbol{\sigma}_1 \cdot \left(-\nabla_{\mathbf{a}} \nabla_{\mathbf{a}} \frac{1}{a} \right) \cdot \boldsymbol{\sigma}_2 \quad (3.63)$$

in the present context, which is exactly the $(k, l) = (1, 2)$ term in Eq. (3.19), and the center-of-mass probability distribution is of no further concern.

3.2.2 Distortion of equilateral triangle geometry

But we need to account for the unavoidable imperfections of any experimental realization: The triangle formed by the trap centers for the three atoms is not exactly equilateral, and the plane of the actual triangle is not exactly perpendicular to the z -axis defined by the bias field.

First, with a_{kl} denoting the distance between the k th and the l th trap center, we define the average distance a by means of

$$\sum_{(k,l)} \left(\frac{a}{a_{kl}} \right)^3 = 3, \quad (3.64)$$

and measure the deviation of a_{kl} from a by the small parameter α_{kl} ,

$$\left(\frac{a}{a_{kl}} \right)^3 = 1 - 3\alpha_{kl}, \quad \sum_{(k,l)} \alpha_{kl} = 0. \quad (3.65)$$

This average a value is used in Eq. (3.20) to determine the dipole-dipole coupling strength $\hbar\Omega$, and we have

$$H_{\text{dd}} = \frac{1}{3} \hbar\Omega \sum_{(k,l)} (1 - 3\alpha_{kl}) \boldsymbol{\sigma}_k \cdot (\mathbf{1} - 3\mathbf{e}_{kl} \mathbf{e}_{kl}) \cdot \boldsymbol{\sigma}_l \quad (3.66)$$

instead of Eq. (3.19), where $\mathbf{1}$ denotes the unit dyadic. If the atoms are indeed trapped in the minima of an optical potential, $|\alpha_{kl}| \simeq 10^{-2}$ is achievable without resorting to extreme measures³.

Second, nonzero z -components of the unit vectors \mathbf{e}_{kl} require

$$\mathbf{1} - 3\mathbf{e}_{kl}\mathbf{e}_{kl} \rightarrow \frac{1}{2}(3\mathbf{e}_z\mathbf{e}_z - \mathbf{1})[1 - 3(\mathbf{e}_z \cdot \mathbf{e}_{kl})^2] \quad (3.67)$$

for the step from Eq. (3.19) to Eq. (3.21). Misalignments that exceed 1° can be avoided with standard experimental techniques, so that $|\mathbf{e}_z \cdot \mathbf{e}_{kl}| = 10^{-2}$ is a conservative estimate.

The combined effect of both imperfections is a modification of H_{dd} , such that

$$H_{\text{dd}} = \frac{1}{3}\hbar\Omega(3J_z^2 - \mathbf{J}^2) + \hbar\Omega K \quad (3.68)$$

with

$$K = \sum_{(k,l)} \epsilon_{kl} \frac{1}{2}(\boldsymbol{\sigma}_k \cdot \boldsymbol{\sigma}_l - 3\sigma_{kz}\sigma_{lz}), \quad (3.69)$$

rather than the $\epsilon_{kl} \equiv 0$ version of Eq. (3.21). The relative size of the imperfections is measured by

$$\epsilon_{kl} = \alpha_{kl} + (\mathbf{e}_z \cdot \mathbf{e}_{kl})^2 - 3\alpha_{kl}(\mathbf{e}_z \cdot \mathbf{e}_{kl})^2, \quad (3.70)$$

wherein, for the values of $|\alpha_{kl}|$ and $|\mathbf{e}_z \cdot \mathbf{e}_{kl}|$ above, the three terms are of the order 10^{-2} , 10^{-4} , and 10^{-6} , respectively, and the α_{kl} contribution dominates.

We note in passing that the imperfection parameters α_{kl} and the dot products $\mathbf{e}_z \cdot \mathbf{e}_{kl}$ that appear on the right-hand side of Eq. (3.70) are not independent of each other. Rather, the triangle condition $a_{12}\mathbf{e}_{12} + a_{23}\mathbf{e}_{23} + a_{31}\mathbf{e}_{31} = 0$ imposes the restriction

$$\sum_{(k,l)} (1 - 3\alpha_{kl})^{-1/3} \mathbf{e}_z \cdot \mathbf{e}_{kl} = 0, \quad (3.71)$$

where the summation over the pairs is cyclic, that is: $(k, l) = (1, 2)$, $(2, 3)$, and $(3, 1)$.

³D. Wilkowski, private communication

The operator K vanishes in the $J = 1/2$ sector,

$$P_{J=1/2} K P_{J=1/2} = 0, \quad (3.72)$$

and there are no first-order contributions from the K -term to the evolution of the RFF qubit. It follows that, during the initial period of high fidelity, the geometrical imperfections contribute in second-order of the small ϵ_{kl} parameters.

3.2.3 Time dependence of RFF-qubit variables

For a quantitative analysis, we employ the master equation that results when Eq. (3.40) is modified in accordance with the observations made here and above,

$$\begin{aligned} \frac{\partial}{\partial t} \rho(t) = & i\omega_0[\rho(t), J_z] + i\Omega[\rho(t), J_z^2 - \frac{1}{3}\mathbf{J}^2 + K] \\ & + \frac{1}{\tau_1} [J_z, [\rho(t), J_z]], \end{aligned} \quad (3.73)$$

where we put $1/\tau \rightarrow 0$, $2\tau' \rightarrow \tau_1$ in the Lindblad operator of Eq. (3.38). While the double-commutator term leads to the fast decay of single-atom spin coherence, as we saw above in Sec. 3.1.5, it is of no consequence for the RFF qubit because all RFF observables as well as their commutators with \mathbf{J}^2 commute with J_z . It follows further that the expectation value $\langle A \rangle_t$ of a RFF variable A , with the three-atom system initially prepared in the $J = 1/2$ sector, is

$$\langle A \rangle_t = \left\langle U_{\text{eff}}(t)^\dagger A U_{\text{eff}}(t) \right\rangle_0 \quad (3.74)$$

with

$$U_{\text{eff}}(t) = P_{J=1/2} \exp(-i\Omega t (J_z^2 - \frac{1}{3}\mathbf{J}^2 + K)) P_{J=1/2}. \quad (3.75)$$

The decoherence is given by the operator $J_z^2 - \mathbf{J}^2 + K$, which can only cause transitions between states with the same magnetic quantum number M . If we label the basis of the subspace with $M = +1/2$ by $\{|J = 1/2, M = 1/2, \lambda = 0\rangle$,

$|J = 1/2, M = 1/2, \lambda = 1\rangle, |J = 3/2, M = 1/2\rangle\}$ and the basis of the subspace with $M = -1/2$ by $\{|J = 1/2, M = -1/2, \lambda = 0\rangle, |J = 1/2, M = -1/2, \lambda = 1\rangle, |J = 3/2, M = -1/2\rangle\}$, the operators in these three dimensional subspaces can be represented as

$$\left(J_z^2 - \frac{1}{3}\mathbf{J}^2 + K\right)_+ \hat{=} \begin{pmatrix} 0 & 0 & -\kappa \\ 0 & 0 & -\kappa^* \\ -\kappa^* & -\kappa & \epsilon - 1 \end{pmatrix}, \quad \left(J_z^2 - \frac{1}{3}\mathbf{J}^2 + K\right)_- \hat{=} \begin{pmatrix} 0 & 0 & \kappa \\ 0 & 0 & \kappa^* \\ \kappa^* & \kappa & \epsilon - 1 \end{pmatrix} \quad (3.76)$$

with the subscripts $+$ and $-$ representing the subspaces for $M = +1/2$ and $M = -1/2$, respectively, where we define

$$\begin{aligned} \epsilon &= \epsilon_{12} + \epsilon_{23} + \epsilon_{31} > 0, \\ \kappa &= \epsilon_{12} + q^2\epsilon_{23} + q\epsilon_{31} = e^{i\varphi}\kappa^*. \end{aligned} \quad (3.77)$$

This suggests that we should split the evolution into subspaces with the same M values as they evolve independently. Since the initial state is in the $J = 1/2$ subspace, the subspace with $M = \pm 3/2$ does not play a role in the evolution at all times. Let us first consider the subspaces with $M = 1/2$ and $M = -1/2$ separately, and define the unitary operator in the $M = 1/2$ subspace to be

$$U_+(t) = \left[e^{-i\Omega t(J_z^2 - \mathbf{J}^2/3 + K)} \right]_+. \quad (3.78)$$

The operator in the $M = -1/2$ subspace is then given by

$$U_-(t) = \begin{pmatrix} 1 & 0 & 0 \\ 0 & 1 & 0 \\ 0 & 0 & -1 \end{pmatrix} U_+(t) \begin{pmatrix} 1 & 0 & 0 \\ 0 & 1 & 0 \\ 0 & 0 & -1 \end{pmatrix}. \quad (3.79)$$

It is not difficult to do the eigenvalue decomposition of $U_+(t)$ analytically. Upon

defining

$$\left. \begin{array}{l} \Omega_1 \\ \Omega_2 \end{array} \right\} = \frac{\Omega}{2} \left(\sqrt{(1-\epsilon)^2 + 8|\kappa|^2} \pm (1-\epsilon) \right), \quad (3.80)$$

we have

$$\begin{aligned} U_+(t) = & \begin{pmatrix} \kappa \\ -\kappa^* \\ 0 \end{pmatrix} \frac{1}{2\kappa^*\kappa} (\kappa^*, -\kappa, 0) + \begin{pmatrix} \kappa \\ \kappa^* \\ \frac{\Omega_1}{\Omega} \end{pmatrix} \frac{e^{i\Omega_1 t}}{2\kappa^*\kappa + \Omega_1^2/\Omega^2} \left(\kappa^*, \kappa, \frac{\Omega_1}{\Omega} \right) \\ & + \begin{pmatrix} \kappa \\ \kappa^* \\ -\frac{\Omega_2}{\Omega} \end{pmatrix} \frac{e^{-i\Omega_2 t}}{2\kappa^*\kappa + \Omega_1^2/\Omega^2} \left(\kappa^*, \kappa, -\frac{\Omega_2}{\Omega} \right). \end{aligned} \quad (3.81)$$

Here, we identify the eigenvalues of $(J_z^2 - \frac{1}{3}\mathbf{J}^2 + K)_+$ being $\{0, -\Omega_1/\Omega, \Omega_2/\Omega\}$ and the eigenvectors are the column vectors in this equation for $U_+(t)$. Since only the evolution in the $J = 1/2$ sector is interesting for this problem, we can use the effective operator $U_+(t)$, and project it onto the $J = 1/2$ subspace. The operator in the $M = -1/2$ subspace can be obtained directly from Eq. (3.79) and, as a result after the projection on the $J = 1/2$ sector, the two effective operators for $U_{\pm}(t)$ have the same form. We have

$$P_{J=1/2} U_{\pm}(t) P_{J=1/2} \hat{=} \frac{1}{2} \begin{pmatrix} 1 & -e^{i\phi} & 0 \\ -e^{-i\phi} & 1 & 0 \\ 0 & 0 & 0 \end{pmatrix} + \frac{1}{2} \begin{pmatrix} 1 & e^{i\phi} & 0 \\ e^{-i\phi} & 1 & 0 \\ 0 & 0 & 0 \end{pmatrix} f(t), \quad (3.82)$$

where

$$f(t) = \frac{\Omega_1 e^{-i\Omega_2 t} + \Omega_2 e^{i\Omega_1 t}}{\Omega_1 + \Omega_2}. \quad (3.83)$$

Hereby, we can rewrite the operator U_{eff} using Eq. (3.82), and then the effective

operator has the simple form

$$U_{\text{eff}}(t) = \frac{1 + f(t)}{2} P_{J=1/2} - \frac{1 - f(t)}{2} (\Sigma_1 \cos \varphi - \Sigma_2 \sin \varphi). \quad (3.84)$$

The decay of the RFF operators directly depends on the function $f(t)$. For $|\alpha_{kl}| \simeq |\mathbf{e}_z \cdot \mathbf{e}_{kl}| \simeq 10^{-2}$ in Eq. (3.70), we have first $\epsilon \simeq |\kappa|^2 \simeq 10^{-4}$ and then $\Omega_1 \simeq \Omega$ and $\Omega_2 = 2|\kappa|^2 \Omega^2 / \Omega_1 \simeq 10^{-4} \Omega$. Accordingly, $f(t)$ is the sum of a long-period oscillation with a large amplitude and a short-period oscillation with a small amplitude; see Fig. 3.5.

The resulting time-dependent expectation values of the RFF observables are

$$\begin{aligned} \langle P_{J=1/2} \rangle_t &= \frac{1 + |f(t)|^2}{2} - \frac{1 - |f(t)|^2}{2} \langle \Sigma_1^{(\varphi)} \rangle_0, \\ \langle \Sigma_1^{(\varphi)} \rangle_t &= \frac{1 + |f(t)|^2}{2} \langle \Sigma_1^{(\varphi)} \rangle_0 - \frac{1 - |f(t)|^2}{2}, \\ \langle \Sigma_2^{(\varphi)} - i \Sigma_3 \rangle_t &= f(t) \langle \Sigma_2^{(\varphi)} - i \Sigma_3 \rangle_0 \end{aligned} \quad (3.85)$$

with

$$\begin{aligned} \Sigma_1^{(\varphi)} &= \Sigma_1 \cos \varphi - \Sigma_2 \sin \varphi, \\ \Sigma_2^{(\varphi)} &= \Sigma_2 \cos \varphi + \Sigma_1 \sin \varphi. \end{aligned} \quad (3.86)$$

Equations (3.85) contain all information about the state of the signal qubit in the course of time. We use them to evaluate the purity of the signal-qubit state at time t and its fidelity with the initial signal-qubit state.

The purity $[1 + s(t)^2]/2$ of the signal-qubit state is quantified by the squared length of its Pauli vector,

$$\begin{aligned} s(t)^2 &= \frac{\langle \Sigma_1 \rangle_t^2 + \langle \Sigma_2 \rangle_t^2 + \langle \Sigma_3 \rangle_t^2}{\langle P_{J=1/2} \rangle_t^2} \\ &= 1 - \frac{|f(t)|^2}{\langle P_{J=1/2} \rangle_t^2} [1 - s(0)^2], \end{aligned} \quad (3.87)$$

so that an initially pure signal-qubit state, $s(0) = 1$, remains pure. When the initial

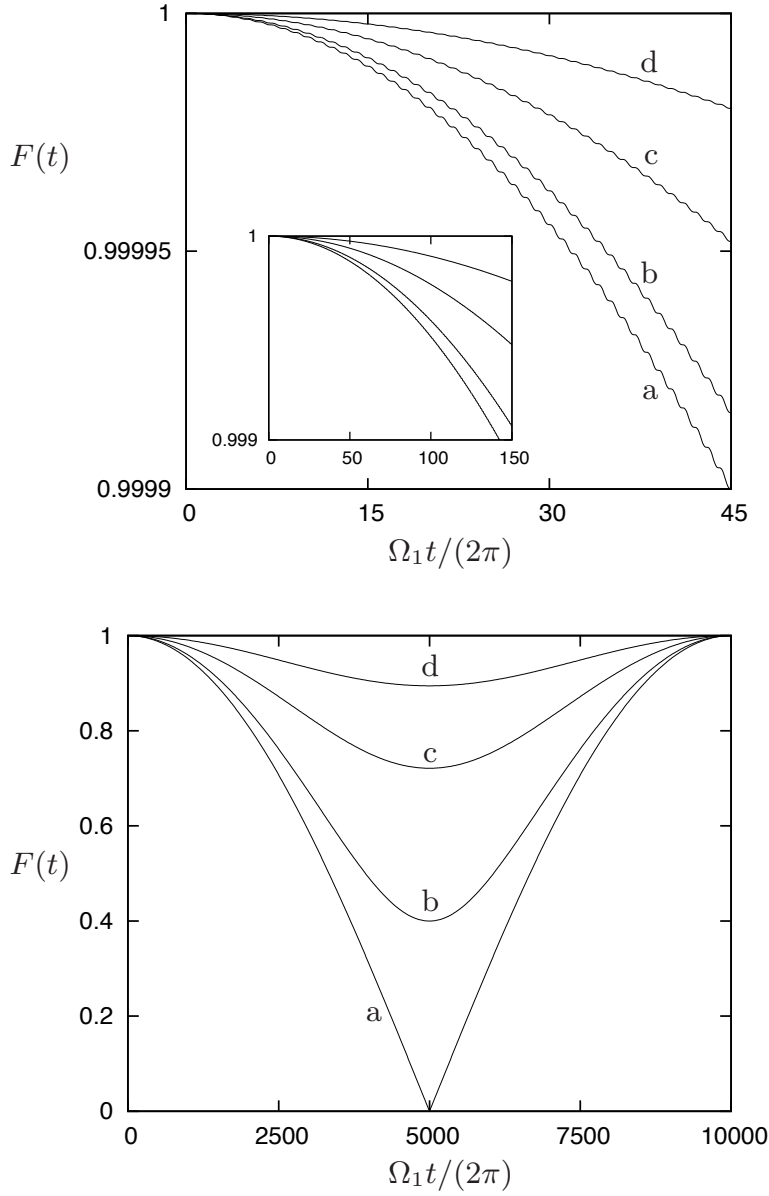


Figure 3.5: Fidelity of the RFF qubit. For $\Omega_2/\Omega_1 = 10^{-4}$, the plots show $F(t)$ of Eq. (3.89) and its lower bound of Eq. (3.90) for $t < 45 \times 2\pi/\Omega_1$ (top plot), for $t < 150 \times 2\pi/\Omega_1$ (inset in the top plot), and for $t < 2\pi/\Omega_2$ (bottom plot). Curve ‘a’ is the lower bound on $F(t)$; the other three curves are for $\langle \Sigma_1^{(\varphi)} \rangle_0 = 0.4$ and $s(0) = 1$ (curve ‘b’), $s(0) = 0.8$ (curve ‘c’), and $s(0) = 0.6$ (curve ‘d’). One can clearly see the small-amplitude short-period oscillations and the large-amplitude long-period oscillation. For the parameter values used throughout the paper, the respective time ranges are 2, 7, and 450 hours. We have $\Omega_1 \approx \Omega$, with $\Omega = 2\pi \times 6\text{MHz}$ given in Eq. (3.20).

state is mixed, $s(0) < 1$, both $s(t) > s(0)$ and $s(t) < s(0)$ are possible, depending on the relative size of $|f(t)|$ and $\langle P_{J=1/2} \rangle_t$. Specifically, we have

$$s(t) \geq s(0) \quad \text{if} \quad (1 + |f(t)|) \left(1 + \langle \Sigma_1^{(\varphi)} \rangle_0 \right) \leq 2 \quad (3.88)$$

and $|f(t)| < 1$.

The fidelity $F(t)$ of the signal-qubit state at the later time t with the initial state is given by

$$F(t)^2 = 1 - \frac{|1 - f(t)|^2}{4\langle P_{J=1/2} \rangle_t} \left(1 - \langle \Sigma_1^{(\varphi)} \rangle_0^2 \right) + \frac{|f(t)| - \text{Re}f(t)}{2\langle P_{J=1/2} \rangle_t} [1 - s(0)^2]. \quad (3.89)$$

It is bounded from below by

$$F(t) \geq \sqrt{1 - \frac{|1 - f(t)|^2}{(1 + |f(t)|)^2}}, \quad (3.90)$$

where the equal sign holds for $f(t) \neq 1$ if, for example, $s(0) = 1$ and $\langle \Sigma_1^{(\varphi)} \rangle_0 = 2/(1 + |f(t)|) - 1$. For $\Omega_2 \ll \Omega_1$ and $t \ll 2\pi/\Omega_2$, this bound is

$$F(t) \geq \cos \frac{\Omega_2 t}{2} - \frac{\Omega_2}{2\Omega_1} \sin \frac{\Omega_2 t}{2} + \dots \quad (3.91)$$

where the ellipsis stands for terms of order $(\Omega_2/\Omega_1)^2$. This two-term approximation serves all practical purposes for $\Omega_2/\Omega_1 \simeq 10^{-4}$. The fidelity is assuredly very high during the early period dominated by the small-amplitude oscillations with frequency $\Omega_1/(2\pi) \simeq \Omega/(2\pi)$: We have $F = 0.9999$ or better for 45 periods of the fast Ω_1 oscillations, and $F = 0.999$ or better for 140 periods, when $\Omega_2 = 10^{-4}\Omega_1$. These matters are illustrated in Fig. 3.5.

3.2.4 Compensating for triangle distortions

In Secs. 3.2.2 and 3.2.3 we regarded the imperfection parameters α_{kl} and $\mathbf{e}_z \cdot \mathbf{e}_{kl}$ as resulting from the lack of perfect control over the apparatus, and their values would not be known with high precision. Suppose, however, that the experimenter has diagnosed the set-up and knows the actual shape of the triangle quite well while having very precise control over the direction of the magnetic bias field. She can then attempt to adjust the bias field such that the three ϵ_{kl} s of Eq. (3.70) are equal, with the consequence that $\kappa = 0$ in Eq. (3.77) and $f(t) \equiv 1$ in Eq. (3.83). We do not discuss this matter in further detail and are content with mentioning that, for

small values of the α_{kl} s, a bias-field direction \mathbf{e}_z with

$$(\mathbf{e}_z \cdot \mathbf{e}_{kl})^2 \simeq \sqrt{\frac{2}{3} \sum_{(k,l)} \alpha_{kl}^2} - \alpha_{kl} \quad (3.92)$$

achieves this, where the approximation neglects terms of second and higher order in the α_{kl} s. With this compensation for the imperfections in the shape of the triangle by a judicious tilt of the bias field, the ratio Ω_2/Ω_1 can be reduced by much, with a corresponding lengthening of the initial period of high fidelity.

3.3 Robustness of the RFF qubit from four spin-1/2 atoms

An alternative construction of a RFF qubit uses four spin-1/2 atoms and their two-dimensional subspace with $J = 0$. A pure state of the RFF qubit is then realized by a pure state of the four-atom system, and decay results from leakage to the sectors with $J = 1$ and $J = 2$, which are nine-dimensional and five-dimensional, respectively. By contrast, a pure state of the three-spin-1/2-atom RFF qubit corresponds to a mixed state of the three-atom system with leakage into the space of the idler qubit and into the $J = 3/2$ sector. Clearly, the two constructions of the RFF qubit are substantially different.

3.3.1 The 2D square geometry

For comparison with the two-dimensional equilateral triangular configuration of three atoms, let us consider four atoms located at the corners of a square; see Fig. 3.6(i). The system is stabilized with a bias magnetic field perpendicular to the plane of atoms to reduce the decoherence due to the internal pollution from the dipole-dipole interactions. The distance between the two diagonal pairs of atoms is $\sqrt{2}$ times larger than the distance between the four pairs at the sides. Thus, the dipole-dipole interaction is unbalanced between all pairs and it cannot be made rotationally invariant by the bias magnetic field. Explicitly, the effective dipole-

3.3. Robustness of the RFF qubit from four spin-1/2 atoms

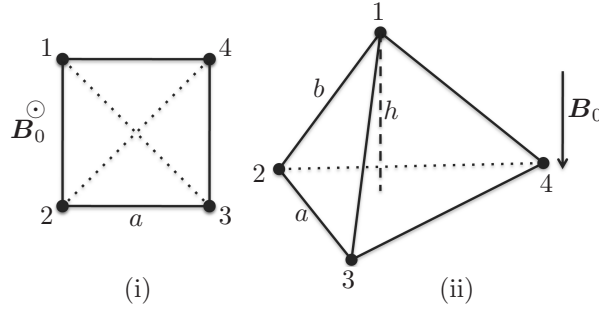


Figure 3.6: RFF qubit constructed from four spin-1/2 atoms. (i) Two-dimensional square configuration. The dipole-dipole interaction is unavoidably unbalanced here because the distance for the two diagonal pairs is larger than the distance for the four edge pairs. (ii) Three-dimensional pyramidal configuration. Here, if the height h is chosen such that $b/a = 0.661$, the effective dipole-dipole interaction has equal strength for all six pairs of atoms.

dipole interaction is here given by

$$H_{\text{dd}} = \frac{1}{3}\hbar\Omega \left(3J_z^2 - \mathbf{J}^2 - \frac{4 - \sqrt{2}}{8} [3(\sigma_{1z}\sigma_{3z} + \sigma_{2z}\sigma_{4z}) - (\boldsymbol{\sigma}_1 \cdot \boldsymbol{\sigma}_3 + \boldsymbol{\sigma}_2 \cdot \boldsymbol{\sigma}_4)] \right) \quad (3.93)$$

with $\hbar\Omega$ as in Eq. (3.20). For the same reasons as in the three-atom case, the stray magnetic field is of no concern, and the system evolves unitarily

$$\rho(t) = e^{-i(H_0 + H_{\text{dd}})t/\hbar} \rho_0 e^{i(H_0 + H_{\text{dd}})t/\hbar}. \quad (3.94)$$

The projector onto the $J = 0$ subspace of the four-atom RFF qubit is given by Eq. (2.14).

The effective dipole-dipole Hamiltonian has the structure of Eq. (3.68), with the operator K now given by

$$K = \frac{c}{4} (\boldsymbol{\sigma}_1 \cdot \boldsymbol{\sigma}_3 + \boldsymbol{\sigma}_2 \cdot \boldsymbol{\sigma}_4 - 3\sigma_{1z}\sigma_{3z} - 3\sigma_{2z}\sigma_{4z}), \quad (3.95)$$

where $c = (4 - \sqrt{2})/6$ accounts for the relative reduction in the strength of the dipole-dipole interaction for the two diagonal atom pairs. Moreover, Eq. (3.74) continues to apply for the expectation value of a RFF operator A , with the four-atom system initially prepared in the $J = 0$ sector. Thereby, the effective unitary

evolution operator is now

$$\begin{aligned} U_{\text{eff}}(t) &= P_{J=0} e^{-iH_{\text{dd}}t/\hbar} P_{J=0} \\ &= \frac{1+f(t)}{2} P_{J=0} + \frac{1-f(t)}{4} (\Sigma_1 + \sqrt{3}\Sigma_2), \end{aligned} \quad (3.96)$$

where Σ_1 , Σ_2 , and Σ_3 are the RFF Pauli operators for the four-atom system as defined in Eqs. (2.16) of Ref. [76], and $f(t)$ is exactly of the form in Eq. (3.83) with Ω_1 and Ω_2 replaced by

$$\left. \begin{array}{l} \Omega_1 \\ \Omega_2 \end{array} \right\} = \frac{\Omega}{2} \left(\sqrt{(2-c)^2 + 8c^2} \pm (2-c) \right) = \begin{cases} 1.78\Omega \\ 0.21\Omega \end{cases} \quad (3.97)$$

which have a ratio of $\Omega_1/\Omega_2 \simeq 8.5$, very different from the ratio of 10^4 in Eqs. (3.83) and (3.77).

The expectation values of the RFF operators in the $J = 0$ sector can be obtained analytically, in particular for the expectation value $\langle P_{J=0} \rangle_t$ and the RFF qubit fidelity $F(t)$, for which the obvious analogs of $\langle P_{J=1/2} \rangle_t$ in Eq. (3.85) and $F(t)$ in Eq. (3.89) apply. With the four-atom version of $f(t)$, the lower bound on $F(t)$ of Eq. (3.90) is valid, and we also have $\langle P_{J=0} \rangle_t \geq |f(t)|^2$. Both lower bounds are shown in Fig. 3.7 for the high-fidelity period of $0 \leq \Omega t \leq 2\pi \times 0.112$. We have a fidelity of 0.9999 or better for $t \leq 0.062 \times 2\pi/\Omega$ and 0.999 or better for $t \leq 0.11 \times 2\pi/\Omega$.

Note, in particular, the substantial probability of losing the four-atom RFF qubit: After the lapse of $t = 0.087 \times 2\pi/\Omega$, there is a chance of more than 10% that the four-atom system has left the $J = 0$ sector. This is a consequence of the rather small Ω_1/Ω_2 ratio. By contrast, for the three-atom qubit with $\Omega_1/\Omega_2 = 10^4$, the persistence probability $\langle P_{J=1/2} \rangle_t$ is never less than 0.9996.

The dipole-dipole coupling strength Ω is proportional to $1/a^3$, where a is the length of the sides of the square. If we use laser beams with the same wavelengths as used for the three-atom system in Sec. 2.2.1 to construct the potential for four atoms in a square geometry, the inter-atomic distance is $a = 663$ nm and Eq. (3.20) gives $\Omega = 2\pi \times 16$ mHz. It follows that we can guarantee $F \geq 0.9999$ for about

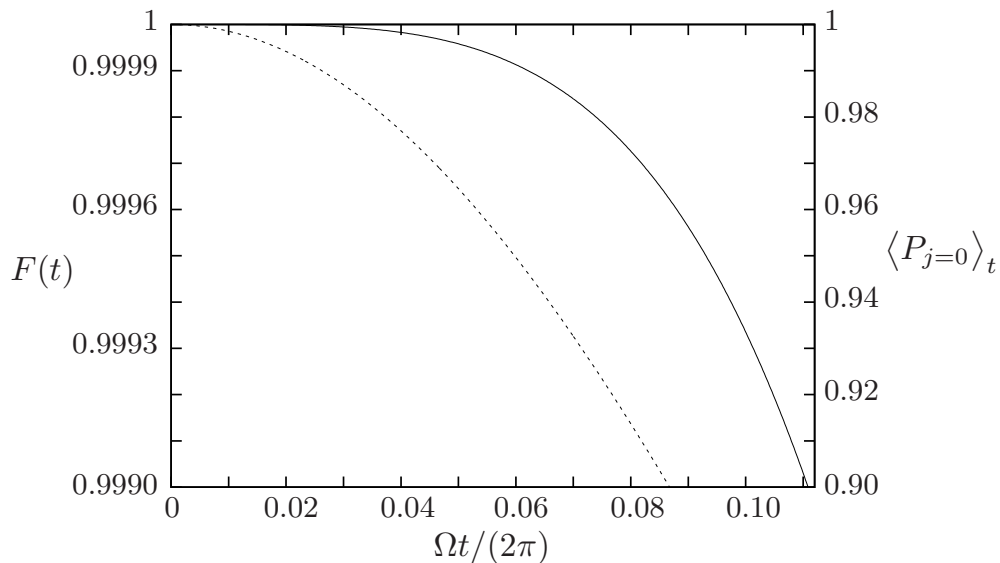


Figure 3.7: Lower bounds for the fidelity $F(t)$ (solid curve) and the expectation value $\langle P_{j=0} \rangle_t$ (dashed curve) for the RFF qubit constructed from four spin-1/2 atoms at the corners of a perfect square. The fidelity of Fig. 3.5 (three atoms with non-ideal geometry) would be indiscernible from $F(t) = 1$ here.

four seconds and $F \geq 0.999$ for about seven seconds. This shows that even with a perfect square geometry, the RFF state constructed from four spin-1/2 atoms decays about 2000 times faster than the qubit constructed from three spin-1/2 atoms in an imperfect equilateral triangle configuration.

3.3.2 The 3D pyramid geometry

The imbalance in the dipole-dipole interaction strength between the pairs of atoms could be removed by using the three-dimensional pyramidal configuration; see Fig. 3.6(ii). Similar as before for three atoms, a bias magnetic field can help us to suppress the non-rotationally invariant part of the dipole-dipole interaction. However, what would be the appropriate direction of the bias magnetic field?

To symmetrize the interaction between any three of the four atoms, the applied bias magnetic field needs to be perpendicular to one face of the tetrahedral, where the atoms reside at the three corners of a perfect equilateral triangle. In this case the fourth atom is singled out, and the vectors connecting this atom to the other three atoms are not perpendicular to the direction of bias magnetic field.

The effective dipole-dipole interaction between this singled-out atom and any

Chapter 3. Robustness of the RFF Qubit

one of the other three atoms is weakened by the bias magnetic field, thus the interaction is not symmetric among all four atoms. To solve this problem, we shorten the height of the tetrahedron. To obtain a rotationally invariant total dipole-dipole interaction, we need

$$\frac{1}{a^3} = \frac{1}{b^3} \left(1 - 3 \frac{h^2}{b^2} \right), \quad (3.98)$$

where h is the height of the tetrahedron and

$$3h^2 = 3b^2 - a^2. \quad (3.99)$$

Let $x = b/a$ and

$$x^5 + 2x^2 = 1. \quad (3.100)$$

We can get the solution numerically: $x \simeq 0.661$.

Here, we have shown that by shortening the height of the tetrahedron, the effective dipole-dipole interaction can be made rotationally invariant. However, lack of control of experimental parameters can still give rise to decoherence. It mainly depends on how well we can make the designed tetrahedron and how well the incident angle of the bias magnetic field can be controlled. The decoherence due to those imperfections could be limited to a similar rate as in the case of three atoms in an equilateral triangular shape, however, it is much more challenging to produce this designed three-dimensional lattice. Therefore, overall speaking, using four atoms is less feasible than using three atoms.

Other than the pyramid of Fig. 3.6(ii), the only arrangement of four atoms such that the effective dipole-dipole interaction is balanced between all six pairs of atoms, is to have the atoms along a straight line and the bias magnetic field with an angle of $\arccos(1/\sqrt{3})$ to that line. Any deviations from the ideal configuration — pyramid or straight line — will, however, tend to introduce a short time scale for the persistence of the fidelity because the partial cancelation inherent in Eqs. (3.77),

which reduced the distortion effects for the three-atom RFF qubit, does not happen in the four-atom case (recall also Sec. 3.2.4).

Clearly, there is no advantage in using the RFF qubits made from four atoms over the RFF qubits made from three atoms. Rather, the simpler three-atom system is preferable.

3.4 Alternatives

We have already analyzed the robustness of the RFF qubit made from three spin- $1/2$ ${}^6\text{Li}$ atoms in detail. How about the robustness of RFF qubits constructed from other physical carriers, for example the ${}^{87}\text{Rb}$ atoms and ${}^{40}\text{Ca}^+$ ions? Likewise, physical systems other than cold atoms should in principle give a long lifetime if information is encoded in the RFF subsystem. In this subsection, we will take the examples of the system of three ${}^{87}\text{Rb}$ atoms in an equilateral triangular lattice and three ${}^{40}\text{Ca}^+$ ions in a linear trap, and study the robustness of RFF qubits made from these two systems qualitatively.

3.4.1 RFF qubit from three ${}^{87}\text{Rb}$ atoms

${}^{87}\text{Rb}$ atom has nuclear spin $3/2$, and the atomic spin of the hyperfine ground state is thus $f = 1$. The magnetic moment is given by $\boldsymbol{\mu} = -\mu_B g_F \mathbf{F}/\hbar$, where g_F is the gyromagnetic ratio, which takes the value $g_F = -1/(I + 1/2) = -1/2$. The hyperfine ground state with $f = 1$ is energetically below the ground state with $f = 2$ by $2\pi\hbar \times 6.8\text{GHz}$; see Fig. (3.8).

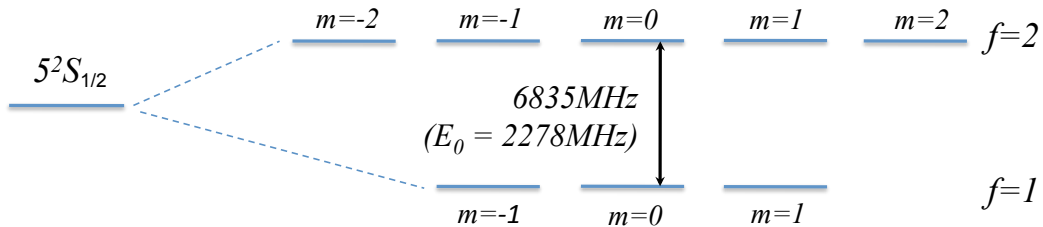


Figure 3.8: Energy level structure of ${}^{87}\text{Rb}$ ground state.

Again we arrange the three rubidium atoms in an equilateral triangular geometry and with each atom confined to its $f = 1$ ground state, the atoms interact with

the external magnetic fields through

$$H_B = \sum_{k=1}^3 \left(-\frac{1}{2} \right) \frac{\mu_B}{\hbar} \mathbf{F}_k \cdot \mathbf{b}_k, \quad (3.101)$$

and we identify the components of spin operator \mathbf{F}_k with Eq. (2.20). Although the spin operators for ^{87}Rb atoms are structurally different from those for ^6Li atoms and gyromagnetic ratios differ by a factor of $3/4$, the strength of their dipole interaction with the magnetic field is of roughly the same order. Since the lifetime of RFF qubit due to decoherence from stray magnetic field can be as long as 600 years, we can also safely conclude that the effect of the stray magnetic field on the RFF qubit made from three ^{87}Rb atoms is also negligibly small.

Other than the magnetic dipole interaction, the spin-1 ^{87}Rb atoms also interact with the external fields via its electric quadrupole moment. The electric quadrupole moment is a dyadic operator, which interacts with the gradient of the electric field, and it vanishes for particles with spin $1/2$ and 0 . Typically, the electric quadrupole interaction is of the same order of magnitude as the magnetic dipole interaction. We have already shown that the decoherence due to magnetic dipole interaction between the atoms and field is of no concern, thus, we can also conclude that the electric quadrupole interaction is of no concern for the decoherence of the RFF qubit, as the gradient of the electric field is also governed by the Maxwell's equations.

Upon replacing the electronic spin operator in Eq. (3.20) with

$$\mathbf{s}_k \rightarrow -\frac{1}{4} \mathbf{F}_k, \quad (3.102)$$

the magnetic dipole-dipole interaction energy between the atoms is given by

$$H_{\text{dd}} = \frac{3\Omega}{4\hbar} \sum_{(k,l)} (\mathbf{F}_k \cdot \mathbf{F}_l - 3\mathbf{F}_k \cdot \mathbf{e}_{kl} \mathbf{e}_{kl} \cdot \mathbf{F}_l) \quad (3.103)$$

with $\hbar\Omega = \frac{\mu_0 \mu_B^2}{4\pi 3a^3}$, the same as previously defined in Eq. (3.20). The hyperfine splitting for the ground state of ^{87}Rb is more than twenty times larger than that

of ${}^6\text{Li}$, thus the transition induced by a 2mG bias magnetic field is completely negligible. The transition induced by H_{dd} is suppressed in the presence of a small bias magnetic field and only the part that commutes with H_{bias} is relevant, thus the effective Hamiltonian for perfect equilateral triangular geometry and no stray magnetic field is given by

$$H_{\text{bias}} + H_{\text{dd}} = \hbar\omega_0 J_z + \frac{1}{3}\hbar\Omega(3J_z^2 - \mathbf{J}^2). \quad (3.104)$$

It has the same form as we had for ${}^6\text{Li}$ in Eq. (3.21); but the energy associated with dipole-dipole interaction is associated to the total angular momentum operator redefined as $\mathbf{J} = \frac{3}{4\hbar}\mathbf{F}$.

In the case of perfect geometry, the decoherence is caused by inhomogeneous stray magnetic field and the electric quadrupole coupling with the stray electric field, thus decoherence is negligible for typical experimental parameters. The spread of the wave function of the ${}^{87}\text{Rb}$ atoms in the same optical potential would be even smaller than the spread of the ${}^6\text{Li}$ atoms, as rubidium atoms are much more massive. Thus, we can also ignore the center-of-mass distribution of the atomic wave function and regard the three atoms as point particles.

The main source of decoherence comes from the distortion of the perfect geometry. The structure and the noise analysis is analogous to that of ${}^6\text{Li}$, and we recall the effective master equation that accounts for geometry imperfection

$$\frac{\partial}{\partial t}\rho(t) = i\omega_0[\rho(t), J_z] + i\Omega[\rho(t), J_z^2 - \frac{1}{3}\mathbf{J}^2 + K] + \frac{1}{\tau_1}[J_z, [\rho(t), J_z]],$$

with

$$K = 2 \sum_{(k,l)} \epsilon_{kl}(\mathbf{J}_k \cdot \mathbf{J}_l - 3J_{kz}J_{lz}). \quad (3.105)$$

It follows further that the expectation value $\langle A \rangle_t$ of a RFF variable A , with the three-atom system initially prepared in the $J = 2$ sector, is given by Eq. (3.74) with

$$U_{\text{eff}}(t) = P_{J=2} \exp(-i\Omega t(J_z^2 - \frac{1}{3}\mathbf{J}^2 + K)) P_{J=2}. \quad (3.106)$$

Chapter 3. Robustness of the RFF Qubit

The decoherence arises from the operator $J_z^2 - \mathbf{J}^2 + K$ which only causes transitions between states with the same magnetic quantum number M . There are seven states with $M = 0$, six states each for $M = \pm 1$, four states each for $M = \pm 2$ and one state each for $M = \pm 3$. We can follow the previous strategy and write a separate Hamiltonian for each individual subspace of conserved M and analyze the decoherence. We will, however, not deal with the detail and exact analytical expression, but just give a general argument instead.

The decoherence happens because the operator K does not commute with the operator J_z , and the speed of the decoherence is related to the strength of the operator K (or the eigenvalues of K). The strength of K is

$$2\Omega\epsilon_{kl} \sim 10^{-2}\Omega, \quad (3.107)$$

where ϵ_{kl} is of magnitude 10^{-2} given by Eq. (3.70). The decay of the RFF qubit depends on a few frequencies that are given by the difference of the eigenvalues of K . The lifetime of the RFF qubit would be at most in the order of magnitude of $100/\Omega$, which is the larger frequency; and of course we might also encounter the case where the fast oscillations that go with $10^{-2}\Omega$ have very small amplitude and the frequencies for the large amplitude oscillation is even much smaller. Without assuming any luck here, we get $100/\Omega \sim 44\text{min}$ as a lower estimation of the lifetime and the fidelity of the state remains very high for at least a few minutes.

With the qualitative argument above, we can conclude that the RFF state made from three spin-1 ^{87}Rb atoms is very robust and a high fidelity of state can be maintained for a few minutes, which is of the typical lifetime of atoms in an optical lattice. Here we omitted the detailed analysis for the spin-1 case, however, of course, the actual robustness of the RFF qubit depends on the experimental setup and parameters, and can do the detailed analysis for the experimental setup at hand when it is needed.

3.4.2 Ions in a linear trap

Other than arranging the atoms in a symmetric geometry to make the effective dipole-dipole interaction rotationally invariant, we can also arrange the atoms in a line and eliminate the dipole-dipole interaction by adjusting the angle of the applied bias magnetic field.

To illustrate this, let us first consider a pair of atoms (labeled by k and l) at distance a apart. Their dipole-dipole interaction energy is

$$H_{\text{dd}} = \frac{\mu_0}{4\pi} \frac{1}{a^3} \boldsymbol{\sigma}_k \cdot (1 - 3\mathbf{e}_{kl}\mathbf{e}_{kl}) \cdot \boldsymbol{\sigma}_l, \quad (3.108)$$

where $\boldsymbol{\sigma}_k$ and $\boldsymbol{\sigma}_l$ denote the Pauli spin operators respectively, and \mathbf{e}_{kl} is the unit vector pointing from atom k to atom l . According to Eq. (3.67), in the presence of a bias magnetic field along the z -axis, the effective dipole-dipole interaction is given by

$$H_{\text{dd,eff}} = \frac{\mu_0}{4\pi} \frac{1}{a^3} \frac{1}{2} (3\sigma_{zk}\sigma_{zl} - \boldsymbol{\sigma}_k \cdot \boldsymbol{\sigma}_l) [1 - 3(\mathbf{e}_{kl} \cdot \mathbf{e}_z)^2]. \quad (3.109)$$

Thus, for a system of three atoms in a line, the effective total dipole-dipole interaction Hamiltonian can be written as

$$H_{\text{dd,eff}} = \frac{\mu_0}{4\pi} \sum_{(k,l)} \frac{1}{a_{kl}^3} \frac{1}{2} (3\sigma_{zk}\sigma_{zl} - \boldsymbol{\sigma}_k \cdot \boldsymbol{\sigma}_l) [1 - 3(\mathbf{n} \cdot \mathbf{e}_z)^2], \quad (3.110)$$

where the summation (k, l) is over all three pairs and \mathbf{n} is the unit vector pointing along the line where the atoms are located. The strength of the dipole-dipole interaction depends on the angle between the line of atoms and the direction of the bias magnetic field, and in particular, we have

$$H_{\text{dd,eff}} = 0 \quad \text{for} \quad (\mathbf{n} \cdot \mathbf{e}_z)^2 = \frac{1}{3}. \quad (3.111)$$

If the angle is denoted by η , as shown in Fig. 3.9, the effective dipole-dipole interaction vanishes when $\eta = \arccos \frac{1}{\sqrt{3}}$. In this case, the dipolar interaction between

the atoms does not lead to decoherence of the RFF qubits.

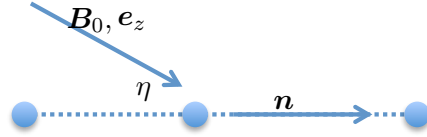


Figure 3.9: Apply the bias magnetic field in the e_z direction to the line of atoms; when $(\mathbf{e}_z \cdot \mathbf{n})^2 = 1/3$, the effective dipole-dipole interaction vanishes. The atoms do not need to be placed at equal distance.

However, in practice, the direction of the applied bias field might not be controlled perfectly. With 1° of error in control of the angle, we have

$$1 - 3 \sin^2 \left(\arcsin \frac{1}{\sqrt{3}} + \frac{\pi}{180} \right) = -0.0497$$

and

$$1 - 3 \sin^2 \left(\arcsin \frac{1}{\sqrt{3}} - \frac{\pi}{180} \right) = 0.0491 .$$

This shows that potentially the dipole-dipole interaction can have a magnitude of

$$H_{\text{dd,eff}} \simeq \frac{\mu_0}{4\pi} \frac{1}{40} \sum_{(k,l)} \frac{1}{a_{kl}^3} (3\sigma_{zk}\sigma_{zl} - \boldsymbol{\sigma}_k \cdot \boldsymbol{\sigma}_l) . \quad (3.112)$$

The difference in the distance a_{kl} for each pair of atoms makes the effective interaction non-rotationally invariant, and thus, it leads to decoherence. The lifetime is

$$\tau \sim \frac{1}{20} \frac{2\pi}{\Omega} , \quad (3.113)$$

where Ω is defined in Eq. (3.20). The decoherence rate is more than a hundred times faster than the equilateral triangular configuration shown in Fig. 3.5, but it is still large enough for many potential applications.

3.5 Summary and discussion

We studied the effect of stochastic magnetic stray fields on the RFF qubit made from three spin-1/2 atoms and found that the RFF qubit decoheres very slowly although the spin states of the individual atoms decay very quickly. The only coupling of the spin-1/2 atoms to the environment is through their magnetic dipole moments, so that magnetic stray fields give rise to uncontrolled changes of the quantum state of the atoms. The long lifetime of the RFF qubit results from its insensitivity to the over-all magnetic field and its fluctuations because they affect all three atoms equally and, therefore, do not affect the RFF qubit at all. Decoherence of the RFF qubit originates in spatial variations of the magnetic field, but they are subject to the constraints imposed by the Maxwell's equations. For parameter values that are typical for experimental situations, we find that the RFF qubit can maintain a very high fidelity for months — if the magnetic stray field is the only source of decoherence.

We then analyzed the effect of the dipole-dipole interactions among the three atoms and imperfections in the geometry of the trapped atoms. We found that the inter-atomic interactions bring more decoherence to the RFF qubit than the fluctuating magnetic stray fields, although the dipole-dipole interaction itself is a unitary process. Nevertheless, the RFF qubit states were shown to be very robust within the parameter regime and under our assumptions.

As an example, we showed that for the RFF qubit made from three ${}^6\text{Li}$ atoms, the lifetime can be 600 years when the geometry of the system is perfect; and a period of high fidelity, say $F = 0.9999$, with respect to the initial state is roughly two hours for non-ideal geometry due to moderate imperfections in the experimental setup. The robustness of the RFF qubit made from three spin-1 ${}^{87}\text{Rb}$ atoms can be analyzed in the same way as for three ${}^6\text{Li}$ atoms, where the lifetime is also limited by non-ideal geometry and the period of high fidelity with respect to the initial state can be roughly a few minutes at least. In the cases of RFF qubits made from neutral atoms in an optical lattice, the lifetime of the qubit is limited by the

Chapter 3. Robustness of the RFF Qubit

collision of the atoms with the rest gas, as the period of high fidelity is longer than the typical trapping time of the atoms.

Geometries for implementing the RFF qubits other than using three atoms in an equilateral triangle geometry are also studied. It is shown that RFF qubits made of four atoms of the same kind in a 2D geometry is not as long-living as RFF qubits made from three atoms in an equilateral triangle. The robustness of the RFF qubit made from four atoms can be improved by arranging the atoms in a 3D tetrahedral geometry, but it requires more complicated trapping schemes compared with the simple structure of three atoms in a 2D equilateral triangle. One can also make RFF qubits with ions in a linear Paul trap. In the ideal case, by applying a bias magnetic field at a specific angle, decoherence from the interactions between ions can be suppressed and long lifetime can be achieved, but this scheme is not very robust against errors in the angle of the bias magnetic field. However, lifetime is still improved with the RFF qubits than using single ion qubits.

Let us review the assumptions that we used to derive the result and discuss their validity.

We have assumed that the atoms are trapped in the deep optical lattice at very low temperature so that their center-of-mass motions are negligible. One example for such a desired optical lattice, created by standard laser techniques, was presented in Sec. 2.2.1. We estimated, in Sec. 3.2.1, the effect of the center-of-mass motion and found that it is much smaller (i.e., 10^{-16}) than the effect of the dipole-dipole interactions for the optical lattice considered.

The most challenging element seems to be to maintain the stable lasers for the optical lattice in order to observe the long-time evolution of the RFF qubit. In a real experiment the collisions with rest-gas atoms are also inevitable and they may very well limit the lifetime of the RFF qubit in practice. We note that drifts of the lasers in time would not spoil the long lifetime as long as all lasers are locked in phase. This is because the time scale for these parameter changes is much slower

and hence all atoms follow the optical lattice adiabatically.

The noise model employed in this study is divided into two types. One is a fluctuating magnetic stray field arising from unavoidable imperfections in the surrounding apparatuses such as the Helmholtz coils, electric wires, and so on. The Helmholtz coils used to generate the homogenous bias magnetic field are identified as the major source for the noise of this kind. Other possible fluctuating magnetic fields are much smaller than this and less inhomogeneous as the respective sources are farther away. We then linearized these fluctuating fields around the homogeneous bias field to analyze the decoherence for the RFF qubit in Secs. 3.1.1 and 3.1.3.

The other type of noise is due to the magnetic dipole-dipole interaction among the three atoms. We have shown that these inter-atomic interactions are a major source of decoherence for the RFF qubit when imperfections of the experimental set-up are taken into account. In Secs. 3.2.2 and 3.2.3, we accounted for deviations from the ideal equilateral triangle configuration of the three atoms as well as a misalignment of the magnetic bias field and found that such insufficiencies still allow for a very long lifetime of the RFF qubit. In fact, we observed that imperfections in the geometry of the three atoms could be compensated for by adjusting the direction of the bias magnetic field, provided that the experimenter has sufficient control over the relevant parameters.

We should not forget to mention that the rotating-wave approximation was used, for example, when analyzing the effect of fluctuating magnetic stray fields. This approximation is valid within the energy scale of our set-up, where the probability for a non-resonant transition is very small. The numerical study without the rotating-wave approximation also supports the validity of our master-equation analysis.

All these results are, of course, derived with the assumption that the parameters used in this study are well controlled with a certain precision. We however took rather conservative numbers for these parameters so that we can estimate a realistic lifetime of the RFF qubit. This also leaves some room for improving the lifetime

Chapter 3. Robustness of the RFF Qubit

of the RFF qubit in further studies.

State preparation of the RFF qubit

Chapter 3 showed that the constructed RFF qubit is robust against decoherence and the lifetime for high fidelity storage is improved by orders of magnitude compared with other available atomic qubits. The follow-up question is how can the quantum information be stored and measured in such systems. As the first step to answer this question, in this chapter, we propose a scheme for preparing a RFF state constructed from three identical particles, with the aid of the Rydberg-blockade mechanism.

In Sec. 4.1, a brief introduction to the Rydberg-blockade mechanism is given. A general scheme of the RFF state preparation is presented in Sec. 4.2. Following that, in Sec. 4.3, we discuss the preparation scheme for RFF states constructed from trios of ${}^6\text{Li}$ atoms, ${}^{87}\text{Rb}$ atoms or ${}^{40}\text{Ca}^+$ ions, respectively, taking into account their specific energy level structures. Finally, we analyze the robustness of this scheme in Sec. 4.4 for the system of three ${}^{87}\text{Rb}$ atoms in an optical lattice, as one example. With modest estimation of experimental errors, the state preparation scheme is shown to be quite robust with a minimum fidelity of about 96%.

4.1 Rydberg Blockade

Rydberg blockade refers to the phenomenon that the Rydberg excitation of a single atom prevents other atoms within a certain blockade radius to be excited to the Rydberg states. This blockade happens owing to the strong dipole-dipole interaction between the Rydberg levels, which has been experimentally observed for electrons

in solid-state devices [82–84], photons [85], and cold atoms [26, 27, 62].

The interaction between two distant neutral atoms is dominated by the dipole-dipole interaction as it is the leading non-vanishing term in the multipole expansion. Moreover, because the magnetic dipolar interaction between atoms is orders of magnitude weaker than the electric dipolar interaction for the same system, we only need to consider the electric dipole-dipole interaction here. The interaction Hamiltonian between atoms a and b are given by

$$V_{\text{dd}} = \frac{\mathbf{d}_a \cdot \mathbf{d}_b - 3\mathbf{n} \cdot \mathbf{d}_a \mathbf{d}_b \cdot \mathbf{n}}{4\pi\epsilon_0 R^3}, \quad (4.1)$$

where \mathbf{d}_a and \mathbf{d}_b are the electric dipole moments of the individual atoms, \mathbf{n} is the unit vector pointing from atom a to atom b and R is the distance between the atoms. This dipole-dipole interaction Hamiltonian couples a pair of atomic states to other pairs of states, following the dipole selection rules. Especially, for a pair of atoms in the same Rydberg state denoted by (r, r) , the dipole-dipole interaction can couple it to another pair of Rydberg states (s, t) :

$$|n_r l_r j_r\rangle + |n_r l_r j_r\rangle \rightarrow |n_s l_s j_s\rangle + |n_t l_t j_t\rangle \quad (4.2)$$

with $l_s + l_t = 2l_r$ and $\Delta m = \pm 1$. The energy difference between the final and initial two-atom states is given by

$$\Delta_{\text{F}} = E(n_s, l_s) + E(n_t, l_t) - 2E(n_r, l_r), \quad (4.3)$$

where Δ_{F} is the so-called Förster defect. The coupling energy between the states is denoted by

$$C = \langle n_s, l_s; n_t, l_t | V_{\text{dd}} | n_r, l_r; n_r, l_r \rangle. \quad (4.4)$$

As a result of the dipole-dipole interaction between the states in Eq. (4.2), the energy of the doubly excited Rydberg state $|rr\rangle$ for the two-atom system is shifted

due to the degenerate perturbation theory by

$$\Delta E = \left(\sqrt{8C^2 + \Delta_F^2} \pm \Delta_F \right) / 2. \quad (4.5)$$

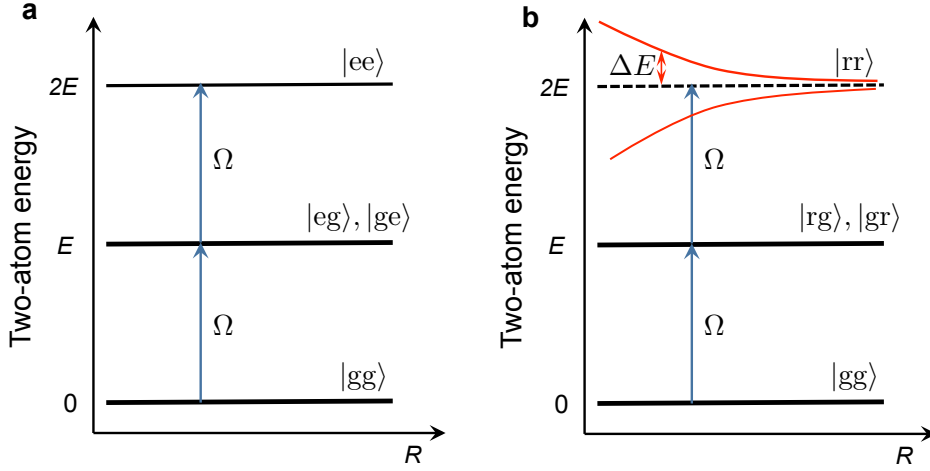


Figure 4.1: Energy levels of the coherent excitations of two-atom systems. Plot ‘a’ shows the energy level for the double excitation to a low-lying excited state $|e\rangle$; plot ‘b’ shows the energy level for double excitation to a Rydberg state $|r\rangle$, where the energy of state $|rr\rangle$ is shifted away from $2E$ by ΔE given in Eq. (4.5), and the true energy level is indicated by the red curves.

For the lower-lying states (small principle quantum number n), the Förster defects Δ_F is orders of magnitude larger than the interaction energy C , such that the energy shifts is negligibly small. Therefore, there is no blockade of multiple excitations to low-lying excited states. The Förster defect Δ_F gets smaller as n increases owing to the quantum defect theory [86], and the energy shift is no longer negligible for Rydberg states with large n . In the regime where $|C| \ll |\Delta_F|$, the interaction is of the van der Waals type and the energy shift is given by

$$|\Delta E| \approx 2 \frac{C^2}{|\Delta_F|} \sim \frac{1}{R^6}. \quad (4.6)$$

In the strong dipole-dipole interaction regime, where $|C| \gg |\Delta_F|$, the energy shift is given by

$$|\Delta E| \approx \sqrt{2}C \sim \frac{1}{R^3}. \quad (4.7)$$

The $1/R^3$ Rydberg shift in the strong dipole-dipole interaction regime is a first-order effect which occurs for some particular states on or nearly on Förster resonance,

i.e. $\Delta_F \simeq 0$. Because of this, such an interaction is also referred to as Förster interaction. The Förster resonance occurs more often for Rydberg states with larger angular momentum $l = 2, 3, \dots$, because these states have smaller quantum defect numbers in general.

Following the blockade mechanism, if two atoms are resonantly driven by a light field tuned to the transition frequency to the Rydberg state $|n_r l_r j_r\rangle$, the doubly excited Rydberg state $|n_r l_r j_r; n_r l_r j_r\rangle$ is detuned by ΔE . When the Rydberg blockade is strong (i.e. $|\Delta E|$ is large), the doubly excited Rydberg state is shifted far off-resonant with the light field. Thus, only a single Rydberg excitation is permitted and it is delocalized over the whole system producing a collective superposition state. Entanglement of multipartite system can be generated deterministically in this way.

Although the general mechanism applies when more than two atoms are presented in the system, there are a couple of aspects worth paying extra attention to. In particular, in the Förster interaction regime, it is possible that the Rydberg blockade of a two-atom system is broken by adding in a third atom, due to quantum interference between different energy exchange channels in many-atom ensembles [87]. By contrast, in the van der Waals interaction regime, the energy shifts are binary additive and such a breaking of the blockade does not happen.

The analysis above treats every single Rydberg state as a non-degenerate state or one particular Zeeman sub-level in their fine or hyperfine multiplets. However, for a system with degenerate Zeeman sub-levels that are coupled to the same light field, the van der Waals blockade can depend on the superposition of the Zeeman sub-levels of the Rydberg state that the atoms are driven to [88]. This Zeeman-level dependency is shown explicitly in Table I of [88], with the exception that $s_{1/2} + s_{1/2} \rightarrow p + p$ is the only channel where the Rydberg energy shift does not depend on the Zeeman sub-levels. This isotropy of the blockade energy is true also for many-atom systems. For example, the group in Stuttgart is using the ns ($n > 40$) state of ^{87}Rb to obtain a Rydberg blockade in cold atomic clouds [62].

In the following part of this chapter, we explore the possibility of preparing the

RFF states with the Rydberg-blockade mechanism.

4.2 General Scheme of RFF State Preparation

Since the noise will turn the idler-qubit state into the completely mixed state in a very short time, to prepare an arbitrary pure RFF state $\alpha|0\rangle + \beta|1\rangle$, we can prepare state $\alpha|+,0\rangle + \beta|+,1\rangle$ with $m = 1/2$ for the idler qubit first, where states $|+,0\rangle$ and $|+,1\rangle$ are given in Eq. (2.5), and then let the noise take it to the RFF state where the idler qubit is in its completely mixed state. The signal qubit information barely decoheres during the short life time of the idler qubit.

States $|+,0\rangle$ and $|+,1\rangle$ are both superposition states of a collective single spin flip of $|\uparrow\uparrow\uparrow\rangle$ with specified geometrical phases. To make such states, one can first drive the three atoms from state $|\uparrow\uparrow\uparrow\rangle$ resonantly with the light field to a chosen Rydberg state to obtain a collective single Rydberg excitation state. And then, another laser field is applied immediately to bring the population in the Rydberg state down to the ground state $|\downarrow\rangle$, resulting in a collective single spin flip of the ground state.

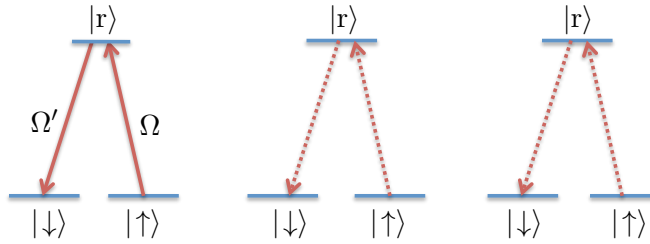


Figure 4.2: Coherently driving the transition between the ground state and a Rydberg state in a three-atom system; only single Rydberg excitation can be obtained owing to the Rydberg-blockade mechanism.

Let us omit the procedure of selecting the suitable Rydberg state first and assume that, for the chosen Rydberg state, the blockade effect is strong enough to block the multiple Rydberg excitations completely among the trio of atoms. The energy shift of the triply excited Rydberg state is roughly of the same order of magnitude as the energy shift of the doubly excited Rydberg state.

The dipole interaction energy between the atoms and the electromagnetic field

is given by

$$V_{AL} = -\mathbf{d} \cdot \mathbf{E} = -g \sum_{j=1,2,3} (|r\rangle\langle g|)_j a(t) e^{i\mathbf{k} \cdot \mathbf{R}_j} + \text{h.c.}, \quad (4.8)$$

where $a(t) = a e^{-i\omega_L t}$ is the time dependent photonic annihilation operator for a single mode laser with frequency ω_L and wave vector \mathbf{k} ; \mathbf{R}_j is the position vector of the j th atom; and g is the atom-light coupling strength, which is assumed to be the same for all three atoms.

Let $\phi_j = \mathbf{k} \cdot \mathbf{R}_j$ and set the origin of the position vector at the position of atom $j = 1$, i.e., $\phi_1 = 0$, $\phi_2 = \mathbf{k} \cdot \mathbf{R}_{12}$ and $\phi_3 = \mathbf{k} \cdot \mathbf{R}_{13}$, where $\mathbf{R}_{jk} = \mathbf{R}_k - \mathbf{R}_j$. With the Rydberg blockade effect, the effective interaction Hamiltonian is given by

$$\begin{aligned} H_{AL} &= -\hbar\Omega \left(|r_{gg}\rangle\langle g_{gg}| e^{i\omega_L t} + |g_{rg}\rangle\langle g_{gg}| e^{i\omega_L t} e^{i\phi_2} + |g_{gr}\rangle\langle g_{gg}| e^{i\omega_L t} e^{i\phi_3} \right) + \text{h.c.} \\ &= -\hbar\sqrt{3}\Omega \frac{1}{\sqrt{3}} \left(|r_{gg}\rangle + e^{i\phi_2} |g_{rg}\rangle + e^{i\phi_3} |g_{gr}\rangle \right) \langle g_{gg}| e^{i\omega_L t} + \text{h.c.}, \end{aligned} \quad (4.9)$$

where we consider a coherent laser field $a|\alpha\rangle = \alpha|\alpha\rangle$ and the coupling strength is measured by the frequency $\Omega = g\alpha$. The field drives a simple two-level transition between state $|ggg\rangle$ and the collective state $\frac{1}{\sqrt{3}} (|egg\rangle + e^{i\phi_2} |geg\rangle + e^{i\phi_3} |gge\rangle)$ resonantly with Rabi frequency $\sqrt{3}\Omega$, which is $\sqrt{3}$ times faster than the Rabi frequency of a single atom system. The effective two-level transition in a N -atom system has an effective atom-light coupling enhanced by \sqrt{N} , due to the normalization factor of the collective states. Experimentally, this \sqrt{N} enhancement was also identified in the work [26] with two atoms, where the Rabi frequency for a collective single Rydberg excitation in a two-atom system was measured.

For brevity, we neglect all the other states that are not involved in the transition and denote the ground state very often by $|g_+\rangle$ and $|g_-\rangle$ instead of $|\uparrow\rangle$ and $|\downarrow\rangle$. A RFF state constructed from three atoms can be prepared in the following three basic steps:

1) Optical pumping:

Three atoms can be trapped in their ground state in an equilateral triangu-

4.2. General Scheme of RFF State Preparation

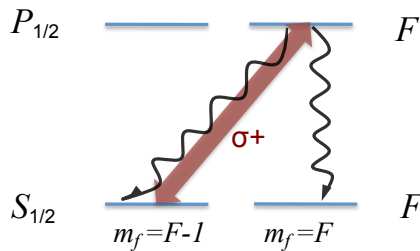


Figure 4.3: Optical pumping of spin- F atoms to the $S_{1/2}$ ground state with $m_f = F$ by applying a σ_+ pumping light field that is coupled to the $P_{1/2}$ excited state.

lar geometry with standard laser cooling and optical trapping. In different Zeeman sub-levels of the individual trapped atoms, the population of state remains random, which is the degree of freedom the RFF qubit is encoded in. To have control over this ground-state spin degree-of-freedom and initialize the system for state preparation, we first optically pump all the atomic population to the single ground state with the largest magnetic quantum number $m_f = F$ and get $|\uparrow\uparrow\uparrow\rangle \hat{=} |g_+g_+g_+\rangle$. This can be achieved by resonantly driving the transition between the ground-state multiplets and an excited-state multiplet of the same number or more Zeeman sub-levels with a σ_+ circularly polarized laser for some duration. The population accumulates in the ground state sub-level with the largest magnetic quantum number because of the spontaneous emission from the excited states.

2) Collective excitation to the Rydberg state:

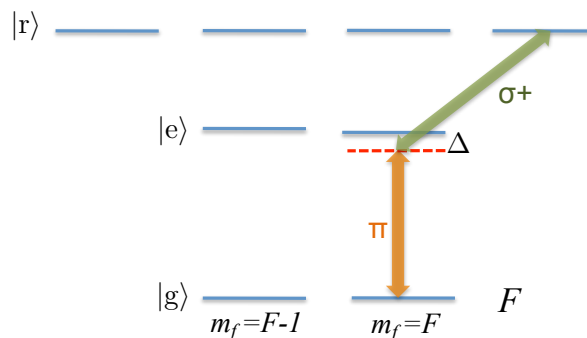


Figure 4.4: Population transfer between the ground state $|g_+\rangle$ and the excited state $|r\rangle$ with a stimulated Raman transition via the intermediate state $|e\rangle$.

The energy difference between the ground state and the Rydberg state is typically too large to find a single laser field to match the transition frequency. Hence, the transition is often driven by a light field consisting of two lasers through a

two-photon stimulated Raman process via an intermediate excited state. Here, as shown in Fig. 4.4, one of the lasers couples the ground state and a intermediate state $|e\rangle$ with linear π polarization, and the other laser couples state $|e\rangle$ to the Rydberg state $|r\rangle$ with σ_+ polarization. With proper control over the applied laser pulse duration, complete population transfer from $|g_+g_+g_+\rangle$ to a collective Rydberg state can be achieved:

$$|g_+g_+g_+\rangle \rightarrow \frac{1}{\sqrt{3}} \left(|rg_+g_+\rangle + e^{i\phi_2}|g_+rg_+\rangle + e^{i\phi_3}|g_+g_+r\rangle \right). \quad (4.10)$$

The manipulation of the phases ϕ_2 and ϕ_3 will be addressed later.

3) Deexcitation of the Rydberg state:

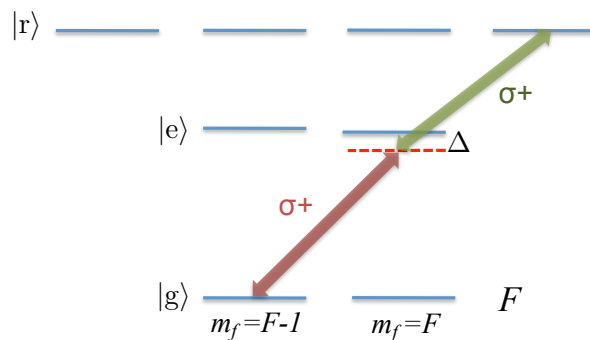


Figure 4.5: Population transfer between the ground state $|g_-\rangle$ and the excited state $|r\rangle$ with a Raman transition via the intermediate state $|e\rangle$.

To avoid spontaneous emission and ionization from the Rydberg state, the laser fields needs to be applied immediately after the previous step to drive all the population in $|r\rangle$ down to a steady ground state. The deexcitation is also done through a two-photon Raman process with the intermediate state $|e\rangle$ detuned by Δ . Both lasers are σ_+ polarized, so that the population in $|r\rangle$ is driven to $|g_-\rangle$ after half of the Rabi cycle.

$$\begin{aligned} & \frac{1}{\sqrt{3}} \left(|rg_+g_+\rangle + e^{i\phi_2}|g_+rg_+\rangle + e^{i\phi_3}|g_+g_+r\rangle \right) \\ \rightarrow & \frac{1}{\sqrt{3}} \left(|g_-g_+g_+\rangle + e^{i\phi_2}|g_+g_-g_+\rangle + e^{i\phi_3}|g_+g_+g_-\rangle \right) \end{aligned} \quad (4.11)$$

Here we note that the same laser can be used for steps 2) and 3) to couple the

4.2. General Scheme of RFF State Preparation

states $|e\rangle$ and $|r\rangle$. Therefore, only three different lasers are required for the Rydberg excitation and deexcitation, and the laser indicated with blue color can be left on all the time while the Rabi pulse duration is controlled with the red and orange lasers. There remains the problem of fixing the phases ϕ_2 and ϕ_3 such as to obtain the desired RFF state.

Obtaining the right phases by adjusting the linearly polarized laser:

To prepare state $|+, 0\rangle$, one needs $\phi_2 = -\phi_3 = 2\pi/3$; and to prepare state $|+, 1\rangle$, one needs $\phi_2 = -\phi_3 = -2\pi/3$. In order to imprint different phases into the superposition state, a non-symmetric interaction between the light field and the three atoms is required. We denote the propagation angle of the light field to the plane of atoms by θ and the angle to the vector \mathbf{R}_{12} by ϕ .

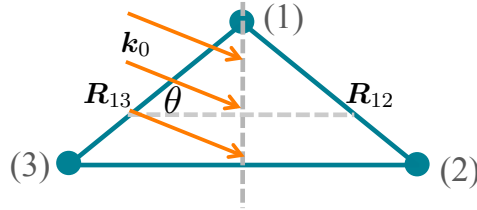


Figure 4.6: The geometrical phase of state $|+, 0\rangle$ is imprinted by shining a laser with wave vector \mathbf{k}_0 at incident angle θ . Angle θ is determined by Eq. (4.13).

We first set \mathbf{k} to be perpendicular to the midline of the triangle that goes through atom $j = 1$, so that the requirement $\mathbf{k} \cdot \mathbf{R}_{13} = -\mathbf{k} \cdot \mathbf{R}_{12}$ is automatically fulfilled. If the laser beam propagates in the plane of the atoms (i.e., $\theta = 0$ and $\phi = \pi/3$), since a π -polarized laser requires $\mathbf{k} \perp \mathbf{e}_z$, we need $\mathbf{k} \cdot \mathbf{R}_{12} = kR \cos(\pi/3) = 2\pi/3 + 2n\pi$. For $n = 0$, we have $R = 2\lambda/3$, where λ is the frequency of the applied laser ($k = |\mathbf{k}| = 2\pi/\lambda$). This sets an extra constraint on R and λ . For an optical lattice, R is determined by the wavelength and geometry of the trapping field, and it would not always be feasible to fulfill the constraint on R and λ when $\theta = 0$.

In order not to impose the strict constraint on R and λ , we can lift the incident laser out of the plane of atoms with an angle θ and the identity $\cos \phi = \frac{1}{2} \cos \theta$

always holds with this geometry. Thus, we have

$$\mathbf{k} \cdot \mathbf{R}_{12} = kR \cos \phi = \frac{1}{2}kR \cos \theta = 2\pi/3 + 2n\pi. \quad (4.12)$$

The incident angle is determined by

$$\cos \theta = \frac{2\lambda}{R} \left(\frac{1}{3} + n \right), \quad (4.13)$$

where the integer n can be chosen freely as long as the right-hand-side does not fall outside the interval $[-1, 1]$.

Note: The quantization axis is set by the bias magnetic field which is perpendicular to the plane of the atoms. Conventionally, the light field with a π -polarization as seen by the atoms requires the light beam to propagate in the xy -plane (the plane of the atoms) and light field of a σ_{\pm} polarization requires the light beam to propagate perpendicular to the plane of the atoms. The σ_{\pm} -polarized light is always in phase for the atoms as $\mathbf{k} \cdot \mathbf{R}_j = 0$. However, since the atoms are not in a line geometry, they would acquire different phase factors at any incident angle in general. Therefore, it is more convenient to adjust the linearly polarized laser to imprint the phases and leave the circularly polarized light coherent. The polarization seen by the atoms depends on the incident angle θ , thus, the polarization has to be adjusted accordingly as well.

According to the previous analysis, to prepare state $|+, 0\rangle$, the appropriate propagation vector is $\mathbf{k}_0 \hat{=} (\cos \theta, 0, -\sin \theta)^T$. The relation $\mathbf{k}_0 \cdot \boldsymbol{\epsilon}_0 = 0$ between the propagation vector and the polarization vector yields an elliptical polarization of the form

$$\boldsymbol{\epsilon}_0 \hat{=} \begin{pmatrix} \frac{\sin \theta}{\cos \theta} \epsilon_z \\ \epsilon_y \\ \epsilon_z \end{pmatrix}. \quad (4.14)$$

This elliptical polarization is carried by the laser beam driving the $|g\rangle \leftrightarrow |e\rangle$ tran-

4.2. General Scheme of RFF State Preparation

sition indicated in Fig. 4.4. If the excited state $|e\rangle$ has the same quantum number F as the ground state $|g\rangle$, the σ_+ component in ϵ_0 would not couple any transition if the initial population is in $|g_+\rangle$. Thus, if we can make the σ_- component vanish, the laser becomes effectively linearly polarized for the atoms. To ensure that there is no σ_- component in ϵ_0 , we need $i\epsilon_x = \epsilon_y$, so that,

$$\mathbf{k}_0 = \begin{pmatrix} \cos \theta \\ 0 \\ -\sin \theta \end{pmatrix} \quad \text{and} \quad \boldsymbol{\epsilon}_0 = \begin{pmatrix} \sin \theta \\ i \sin \theta \\ \cos \theta \end{pmatrix} / \sqrt{1 + \sin^2 \theta}. \quad (4.15)$$

The preparation of state $|+, 1\rangle$ can be done by changing the incident angle $\theta \rightarrow \pi - \theta$, as the phases of the light field on atoms 2 and 3 is proportional to $\cos \theta$ and needs to be reversed. This yields

$$\mathbf{k}_1 = - \begin{pmatrix} \cos \theta \\ 0 \\ \sin \theta \end{pmatrix} \quad \text{and} \quad \boldsymbol{\epsilon}_1 = - \begin{pmatrix} \sin \theta \\ i \sin \theta \\ -\cos \theta \end{pmatrix} / \sqrt{1 + \sin^2 \theta}. \quad (4.16)$$

Prepare an arbitrary pure qubit state $\alpha|+, 0\rangle + \beta|+, 1\rangle$

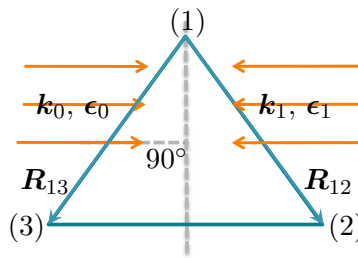


Figure 4.7: Top view of the trio of atoms and two applied coherent laser beams with wavevectors \mathbf{k}_0 and \mathbf{k}_1 and polarization vectors $\boldsymbol{\epsilon}_0$ and $\boldsymbol{\epsilon}_1$, as given in Eqs. (4.15) and (4.16).

If the two lasers with wave vectors \mathbf{k}_0 and \mathbf{k}_1 are applied simultaneously, the

atom-light interaction Hamiltonian is given by

$$\mathbf{V}_{AL} = - \sum_{j=1,2,3} (|r\rangle\langle g|)_j g a(t) \left(\alpha e^{i\mathbf{k}_0 \cdot \mathbf{R}_j} + \beta e^{i\mathbf{k}_1 \cdot \mathbf{R}_j} \right) + \text{h.c.}, \quad (4.17)$$

where g denotes the common factor in the atom-light coupling strength of the two fields and α/β is the relative ratio of the electric field amplitudes of the laser beams denoted by \mathbf{k}_0 and \mathbf{k}_1 in Fig. 4.7. Following the same scheme proposed previously, the encoded state is thus

$$|\uparrow\uparrow\downarrow\rangle + |\uparrow\downarrow\uparrow\rangle \left(\alpha e^{i\mathbf{k}_0 \cdot \mathbf{R}_2} + \beta e^{i\mathbf{k}_1 \cdot \mathbf{R}_2} \right) + |\downarrow\uparrow\uparrow\rangle \left(\alpha e^{i\mathbf{k}_0 \cdot \mathbf{R}_3} + \beta e^{i\mathbf{k}_1 \cdot \mathbf{R}_3} \right),$$

after going through the excitation and deexcitation of a chosen Rydberg state. If we set the coordinates such that $\mathbf{R}_{12} = R(1/2, -\sqrt{3}/2, 0)^T$ and $\mathbf{R}_{13} = -R(1/2, \sqrt{3}/2, 0)^T$, together with the condition $\cos \theta = \frac{2\lambda}{R} \left(\frac{1}{3} + n \right)$, the state becomes

$$|\uparrow\uparrow\downarrow\rangle(\alpha + \beta) + |\uparrow\downarrow\uparrow\rangle(\alpha q + \beta q^2) + |\downarrow\uparrow\uparrow\rangle(\alpha q^2 + \beta q) \propto \alpha|+, 0\rangle + \beta|+, 1\rangle. \quad (4.18)$$

Therefore, to prepare the qubit state $\alpha|+, 0\rangle + \beta|+, 1\rangle$, we need

$$\frac{\alpha}{\beta} = \frac{|E_0|}{|E_1|} e^{i(\phi_0 - \phi_1)}, \quad (4.19)$$

where $\phi_0 - \phi_1$ denotes the relative phase difference of the laser beams, and E_0 and E_1 denote the electric field strengths, respectively. An arbitrary pure RFF qubit state can be prepared in this way.

4.3 Choice of atoms

The scheme presented in Sec. 4.2 applies generally for a system of three identical atoms in an equilateral triangle geometry. The atomic level structures, frequencies of laser beams to use and many other aspects strongly depend on the choice of atoms. In this section, we address these issues briefly for three examples of qubit carriers, namely ${}^6\text{Li}$ atoms, ${}^{87}\text{Rb}$ atoms and ${}^{40}\text{Ca}^+$ ions.

For three atoms trapped at about $1\mu\text{m}$ away from one another, the Rydberg blockade of the van der Waals kind is sufficiently strong so that we do not need to find a Rydberg state with an extremely small Förster defect for a good blockade. With the ground state of the electron being a s state, a two-photon excitation can bring the electron to either a d or a s Rydberg state. Compared to the nd Rydberg states, using the ns Rydberg states has a few advantages. First, the ns states have isotropic blockade over all Zeeman sub-levels, but in comparison, Zeeman superposition states with no blockade effect, referred to as Förster zero states, can be found for nd Rydberg states where the double Rydberg excitation is not blocked [88]. Moreover, the hyperfine and Zeeman structures are simpler for a s state than for a d state, which can make the optical addressing easier. Therefore, we choose to use the ns Rydberg states in our scheme.

4.3.1 Three ${}^6\text{Li}$ atoms

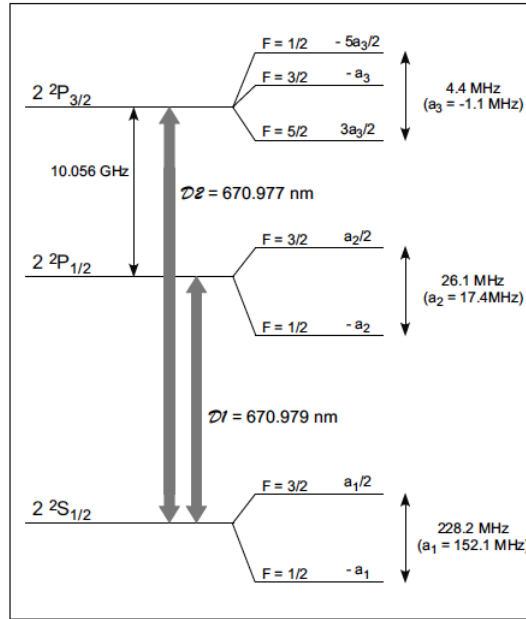


Figure 4.8: Energy diagram of the ${}^6\text{Li}$ $2s$ and $2p$ levels [1].

${}^6\text{Li}$ has two D-transition lines, namely the transition $2s_{1/2} \rightarrow 2p_{1/2}$ and $2s_{1/2} \rightarrow 2p_{3/2}$; see Fig. 4.8. The fine-structure splitting of the $2p$ level is about 10 GHz, and this large splitting enables us to address the $2p_{1/2}$ and the $2p_{3/2}$ levels separately on the scale of a typical laser detuning Δ of a few hundred MHz. We choose the simpler

$2p_{1/2}$ as the intermediate level, and the two hyperfine multiplets with $F = 1/2$ and $F = 3/2$ are driven by the fields simultaneously, since the hyperfine splitting is $26.1\text{MHz} \ll \Delta$. The applied pulse duration for the Rabi flopping from the ground state to the Rydberg state depends on the light-atom coupling to both hyperfine multiplets of the intermediate $2p_{1/2}$ level.

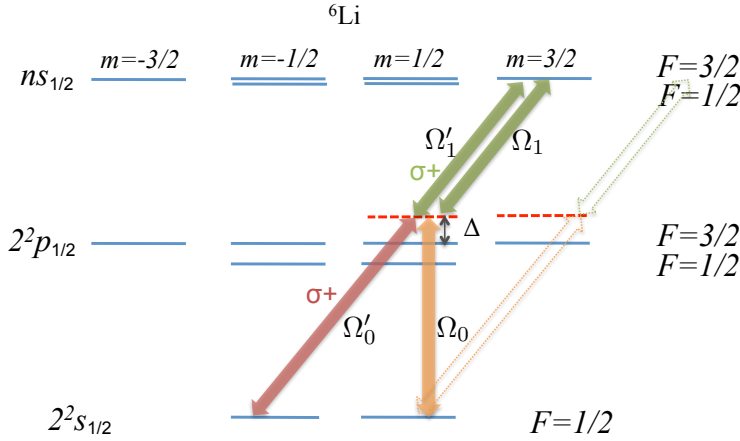


Figure 4.9: Optical transition diagram of the RFF state preparation with ${}^6\text{Li}$ atoms.

The hyperfine multiplet of $|2s_{1/2}, F = 3/2\rangle$ is not shown in Fig. 4.9 as it is more than 200MHz apart from the $|2s_{1/2}, F = 1/2\rangle$ states and is far off-resonant with the two-photon Raman transition. The hyperfine coupling for the Rydberg states is on the order of kHz only, which is negligible against almost all the other coupling energies in the system. The Rydberg state $|n s_{1/2}, F = 3/2, m_F = 3/2\rangle$ is used here, as it is the state with the largest magnetic quantum number for that particular Rydberg level, that can make the σ_+ component of the laser coupling $|g\rangle \leftrightarrow |e\rangle$ to be idle for the atoms. Theoretical computation of the dipole matrix elements and the transition frequencies can be found in Appendix A.

Having a Rydberg state with a large van der Waals interaction and a strong coupling to the intermediate p state at the same time would be desirable. Unfortunately, these criteria contradict each other very often. Depending on the available laser power and experimental set-up, Rydberg levels with $n \geq 20$ may be used.

4.3.2 Three ^{87}Rb atoms

Compared with the ^6Li atoms, the ^{87}Rb atoms are much more frequently used in Rydberg blockade experiments. The availability of lasers to establish the two-photon Rydberg transition is one of the major reasons that favor the rubidium atoms among all the alkali-metal families. The hyperfine structure of the ^{87}Rb D1 and D2 transitions is shown in Fig. 4.10.

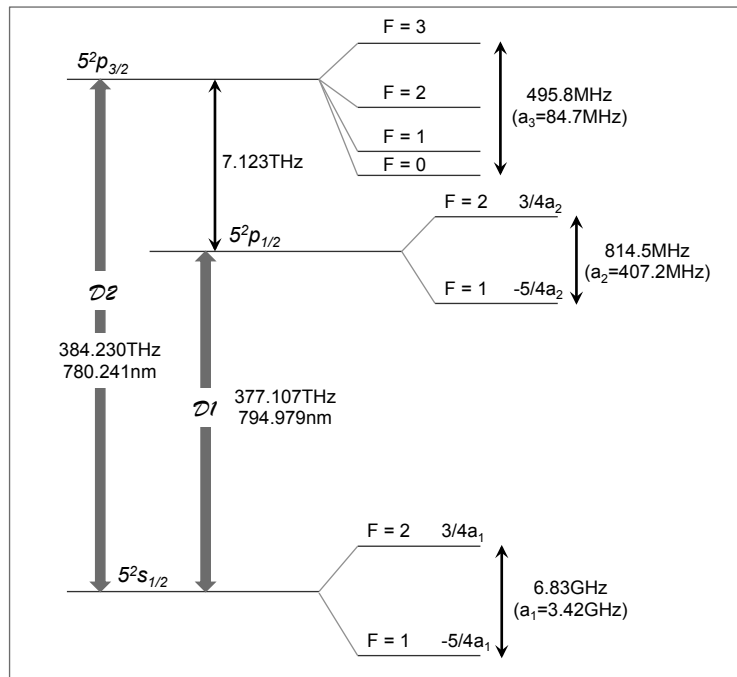


Figure 4.10: Energy diagram of the $5s$ and $5p$ levels of ^{87}Rb .

Selection criteria of the intermediate state and the Rydberg state are similar as for ^6Li . However, the hyperfine splitting of $5p_{1/2}$ state is about 800MHz , that is in the same order of Δ , so both hyperfine states serve as intermediate levels for the Raman transition to the Rydberg state simultaneously. To have a strong van der Waals interaction as well as a large light-atom coupling, the $ns_{1/2}$ Rydberg level with $n \geq 40$ may be used. The energy level transition scheme of ^{87}Rb is sketched in Fig. 4.11.

4.3.3 Three $^{40}\text{Ca}^+$ ions

As it is pointed out in Sec. 2.2.2, $^{40}\text{Ca}^+$ does not have a nuclear spin, and hence, no hyperfine structure. Because of this, it is easier to identify a single intermediate

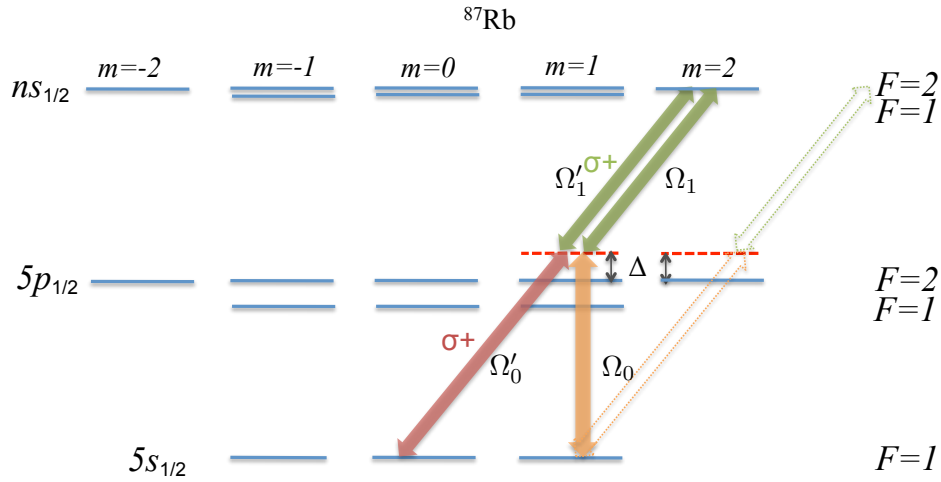


Figure 4.11: Optical transition diagram of the RFF state preparation with ^{87}Rb atoms.

state that is involved in the Raman transition to the Rydberg state. Following the previous examples of ^6Li and ^{87}Rb atoms, a schematic plot of the level transition is shown in Fig. 4.12.

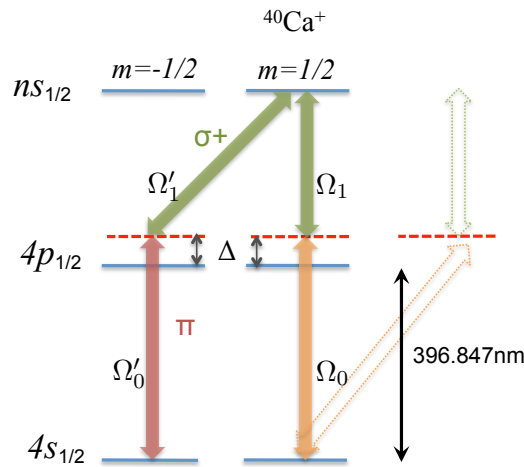


Figure 4.12: Optical transition diagram of the RFF state preparation with $^{40}\text{Ca}^+$ ions.

However, the ionization energy of $^{40}\text{Ca}^+$ is much larger than the alkali atoms: the second ionization from the $4s^1$ ground state requires light with very high frequency. As a result, the Rydberg excitation energy is in the vacuum ultraviolet (VUV) range. One can either employ a wave-mixing method to obtain the corresponding VUV laser [89] or use higher-order Raman transitions of three photons or more to achieve the Rydberg excitation. The level scheme shown in Fig. 4.12 is

only a rough schematic sketch.

4.4 Robustness of RFF State Preparation

In this section, we study the robustness of the state preparation scheme by considering the possible sources of errors in practice. The state preparation of an arbitrary pure RFF qubit $\alpha|+, 0\rangle + \beta|+, 1\rangle$ was studied previously in Secs. 4.2 and 4.3 for the ideal system. However, imperfect control in the system can limit the fidelity of the state prepared. Here is an list of some potential sources of error:

- 1) optical pumping
- 2) double or triple Rydberg excitation
- 3) Rabi frequency and pulse duration control
- 4) incident angles of the laser beams
- 5) laser profile
- 6) atomic Zeeman sublevels and AC Stark effect
- 7) center-of-mass motion of atoms

We will study first the robustness of the state preparation due to a few of the sources of error that is easy to analyze analytically. We also simulated the state preparation procedure taking into account different sources of errors, and results are given at the end of this section.

4.4.1 Error analysis

Inefficiency of optical pumping

Optical pumping was developed in the early 1950s by Alfred Kastler, and since then it has been commonly used to pump electrons to a well-defined quantum state. Here, we use the technique to coherently pump the valence electrons of the three atoms to the same hyperfine sub-level to achieve full population transfer to the state $|g_+g_+g_+\rangle$. A laser with σ_+ polarization serves as the pumping field and population accumulates in state $|g_+g_+g_+\rangle$ owing to the spontaneous emission of

the excited states.

In practice, the efficiency of the coherent optical pumping is limited by power-broadening of the transition bandwidth, hyperfine structure trapping and other undesirable effects. With today's state of the art, the efficiency of optically pumping electrons to a definite hyperfine ground state of the popular alkali atoms can reach near perfection with an efficiency higher than 99%. However, the population that fails accumulating in state $|g_+g_+g_+\rangle$, when the pumping laser is switched off, would contribute directly to the inefficiency of the RFF state preparation, as this population would not be controlled in the following steps of the state preparation.

Error in Rydberg blockade

Complete blockade of the doubly and triply excited Rydberg states happens for infinitely large Rydberg shift. In the real physical system, where the Rydberg shift is large but finite, transitions to doubly or triply excited Rydberg states are possible although strongly suppressed.

The probability of double excitation is given by Eq. (18) in Ref. [88] as

$$P_2 = \sum_{\phi; k < l} |c_{\phi kl}|^2 = \frac{\Omega_N^2}{N^2} \sum_{\phi, k < l} \left| \frac{\kappa_{\phi kl}}{\Delta E_{\phi kl}} \right|^2, \quad (4.20)$$

where $\Omega_N = \sqrt{N}\Omega_{\text{eff}}$ is the effective Rabi frequency between the ground state and the Rydberg state for an ensemble of N atoms, $\kappa_{\phi kl} \equiv N \langle \phi kl | \mathcal{V}_k^\dagger \mathcal{V}_l^\dagger | g \rangle / \Omega_N^2$ gives the relative amplitude for exciting a particular pair kl of atoms to the doubly excited Rydberg state ϕ , \mathcal{V}_j is the light-atom interaction Hamiltonian for atom j and $\Delta E_{\phi kl}$ is the Rydberg shift of state ϕ for the pair of atoms labeled kl .

In the three-atom system we are studying, the atomic distance is the same between all pairs, thus the summation over $k < l$ gives a factor of 3 accounting for all the pairs. With the equilateral triangular configuration and assuming the light is only coupled to a single Rydberg state, we have $\Delta E_{\phi kl} = \Delta E$ and $\kappa_{\phi kl} = 1$.

Thus, the probability of double excitation is simply

$$P_2 = \left| \frac{\Omega_{\text{eff}}}{\Delta E} \right|^2. \quad (4.21)$$

In addition to the production of doubly excited Rydberg states, a finite Rydberg shift also causes a shift in the effective Rabi frequency of the two-level system through virtual excitation of the doubly excited states. The error due to this is roughly about P_2 also. For example, with $\Omega_{\text{eff}} = 10\text{MHz}$ and $\Delta = 500\text{MHz}$, the error due to the multi-excitation is about 0.04%. In the van der Waals interaction regime, for a $ns_{1/2}$ Rydberg state, the interaction is always repulsive and isotropic so that the Rydberg shift for triply excited state is even larger. Thus, the probability of having all three atoms excited in our system is negligible.

Error in Raman transition

Raman transitions are used in both steps of the excitation and deexcitation between the ground states and the Rydberg state, where pulses lasting for half of the oscillation period that produces a full Rabi flopping are required. The required pulse duration can either be determined experimentally or theoretically.

Experimentally, one can measure the Rydberg state population after switching the laser beams on and off for different durations. The time-dependent curve of the Rydberg population can be plotted after repeating the experiment many times, from which the Rabi oscillation period can be estimated. However, the error in the oscillation period determined experimentally this way can be large.

Theoretically, with complete information of the applied laser and the energy spectrum of the atoms, the effective Rabi oscillation period can be computed analytically with very high precision. More of this will be discussed in Chapter 5.

The experimental error in controlling the applied pulse duration can be very small. However, the abrupt switching on and off of the laser power can generate large boardening in the frequency spectrum and so cause other undesired effects. Thus, we assume that the laser pulse is switched on and off gradually within a

duration of typically 10 nanoseconds or longer.

Error in relative intensity and phase of the lasers

When encoding an arbitrary RFF state $|\psi\rangle = (|+,0\rangle + \alpha e^{i\phi}|+,1\rangle)/\sqrt{1+\alpha^2}$, where $\alpha = |E_0/E_1|$ is the ratio between the power of the two sets of lasers encoding $|+,0\rangle$ and $|+,1\rangle$ respectively, control over the parameters α and ϕ is important. The incident angles of the lasers determine if the transition $|g_+g_+g_+\rangle \rightarrow |+,0\rangle$ or $|g_+g_+g_+\rangle \rightarrow |+,1\rangle$ is driven. For the coherent transition to the collective single excitation state, the effective Rabi frequency can be computed as if the lasers are coherently driving the same state. Let δ_α be the percentage error in the relative laser strength α , and δ_ϕ be the percentage error in the relative phase $\phi = \phi_0 - \phi_1$. The actual prepared state would be

$$|\tilde{\psi}\rangle = \frac{1}{\sqrt{1+\alpha^2(1+\delta_\alpha^2)}} [|+,0\rangle + \alpha(1+\delta_\alpha)e^{i(1+\delta_\phi)\phi}|+,1\rangle]. \quad (4.22)$$

With the fidelity of state defined by $F = |\langle\tilde{\psi}|\psi\rangle|^2$, we have

$$F = \frac{1}{(1+\alpha^2)[1+\alpha^2(1+\delta_\alpha^2)]} \left[(1+\alpha^2(1+\delta_\alpha))^2 \cos^2(\delta_\phi) + \alpha^4(1+\delta_\alpha)^2 \sin^2(\delta_\phi) \right]. \quad (4.23)$$

This fidelity is higher than 99%, for a 5% maximum percentage error in α and ϕ .

Incident angles of the lasers

In the ideal case, we have two sets of lasers coming with incident angles θ and $\pi - \theta$ to the xy -plane to prepare state $|\psi\rangle = (|+,0\rangle + \alpha e^{i\phi}|+,1\rangle)/\sqrt{1+\alpha^2}$. In general, the wave vector can be written as $\mathbf{k} = \mathbf{k}_\parallel + \mathbf{k}_\perp$, where \mathbf{k}_\parallel is the component of \mathbf{k} projecting into the plane of the atoms and \mathbf{k}_\perp is the component that is perpendicular to the plane of the atoms. Here we define

$$\cos \theta = \frac{k_\parallel}{k}, \quad \cos \varphi = \frac{\mathbf{k}_\parallel \cdot \mathbf{R}_2}{k_\parallel R_2} \quad \text{and} \quad \cos \phi = \frac{\mathbf{k} \cdot \mathbf{R}_2}{k R_2}, \quad (4.24)$$

4.4. Robustness of RFF State Preparation

so that the identity

$$\cos \phi = \cos \theta \cos \varphi \quad (4.25)$$

holds. In the ideal case, the phases of the RFF state can be matched with $\cos \phi = \frac{1}{2} \cos \theta$, where $\cos \varphi = 1/2$ and $\cos \theta = \frac{2\lambda}{R} (n + \frac{1}{3})$ as in Eq. (4.13).

Errors in the incident angles might produce a different final state. Let ϕ_2 and $\tilde{\phi}_2$ represent the real angles between $\mathbf{k}_0, \mathbf{k}_1$ and \mathbf{R}_{12} and ϕ_3 and $\tilde{\phi}_3$ represent the real angles between $\mathbf{k}_0, \mathbf{k}_1$ and \mathbf{R}_{13} respectively in a experiment, the final state obtain is

$$|\tilde{\psi}\rangle = \frac{1}{\sqrt{3(1+\alpha^2)}} \left[(1 + \alpha e^{i\phi}) |\downarrow\uparrow\uparrow\rangle + (e^{ikR_2 \cos \phi_2} + e^{ikR_2 \cos \tilde{\phi}_2} \alpha e^{i\phi}) |\uparrow\downarrow\uparrow\rangle + (e^{ikR_2 \cos \phi_3} + e^{ikR_2 \cos \tilde{\phi}_3} \alpha e^{i\phi}) |\uparrow\uparrow\downarrow\rangle \right]. \quad (4.26)$$

The fidelity between the actual prepared state $|\tilde{\psi}\rangle$ and the targeted state $|\psi\rangle$ is given by

$$F = \frac{1}{3^2(1+\alpha^2)^2} \left| (1 + \alpha e^{i\phi})(1 + \alpha e^{-i\phi}) + (q + q^2 e^{i\phi})(e^{-ikR \cos \phi_2} + e^{-ikR \cos \tilde{\phi}_2} \alpha e^{-i\phi}) + (q^2 + q e^{i\phi})(e^{-ikR \cos \phi_3} + e^{-ikR \cos \tilde{\phi}_3} \alpha e^{-i\phi}) \right|^2. \quad (4.27)$$

Imperfect geometry of the triangle

In practice, the optical lattice produced might not give the perfect equilateral triangular geometry as designed. Moreover, the center-of-mass motion would have an effect on the relative positions of the atoms as well.

In Fig. 4.13, we denote the actual distance between the atoms by R_{12} , R_{13} and R_{23} respectively, and the angle $\eta \equiv \angle 213$ is given by

$$\eta = \arccos \left(\frac{R_{12}^2 + R_{23}^2 - R_{13}^2}{2R_{12}R_{23}} \right). \quad (4.28)$$

The distances and angles depend on the actual experimental set-up. We can com-

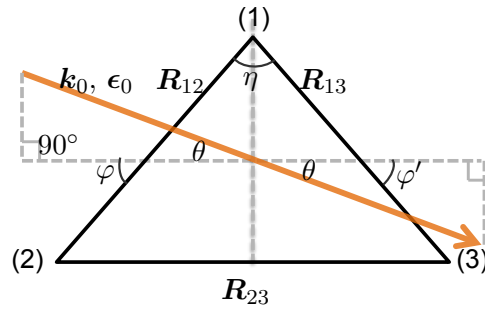


Figure 4.13: The geometry of the three atoms and the incident laser labeled by \mathbf{k}_0, ϵ_0 with imperfection.

bine the error from the imperfect triangle together with the error from the incident angles of the lasers, as both of them cause errors in the geometrical phases of the state prepared.

The phase $\{\phi_2, \phi_3\}$ and $\{\tilde{\phi}_2, \tilde{\phi}_3\}$ in Eq.(4.26) are related to each other pairwise. Assume the real value of angle θ and φ shown in Fig. 4.13 are given for the experiment, the angle ϕ_2 is, thus, given by $\phi_2 = \arccos(\cos \theta \cos \varphi)$. The other angle is given by

$$\phi_3 = \arccos(\cos \theta \cos \varphi') = \arccos(\cos \theta \cos(\pi - \varphi - \eta)). \quad (4.29)$$

The same relation applies for the laser beam coming from the other direction. Fidelity of state can be calculated with Eq. (4.27).

Profile of the laser beams

For a laser beam with a Gaussian frequency distribution, the electric field component of this field can be written as

$$\sqrt{\frac{I}{\pi \epsilon_0 c \sigma^2}} e^{-\frac{(\omega - \omega_0)^2}{\sigma^2}} \cos(\omega t) \boldsymbol{\epsilon}, \quad (4.30)$$

where I is the field intensity, ω_0 is the central frequency, σ is the bandwidth and $\boldsymbol{\epsilon}$ is the polarization vector. To obtain the total electric field strength, we can integrate over ω and have

$$\mathbf{E}(t) = \sqrt{\frac{I}{\epsilon_0 c}} e^{-(\sigma t/2)^2} \cos(\omega_0 t) \boldsymbol{\epsilon}. \quad (4.31)$$

4.4. Robustness of RFF State Preparation

The beam intensity can be measured with very high precision, and the laser bandwidth can be made narrower than 1MHz (bandwidth in the kHz range can be reached with the current technology).

Compared with the frequency profile, it is much more difficult to determine precisely the spatial profile. For a Gaussian beam, the time-averaged intensity distribution over space is given by

$$I(r, z) = I_0 \left(\frac{w_0}{w(z)} \right)^2 e^{-\frac{2r^2}{w^2(z)}}, \quad (4.32)$$

where r is the radial distance from the center axis of the beam, z is the axial distance from the beam's narrowest point, I_0 is the intensity at the center of the beam at its waist and $w(z)$ is the radial radius at which the field amplitude and intensity drop to e^{-1} of their axial value respectively. Ideally, we want the atoms to be located at the same distance from the beam center and to experience the same field intensity. The uncertainty in the relative position between the beams and the three atoms causes errors in the atom-light coupling amplitude. However, with careful control, the error is small if $w(r)$ is much larger than the atomic distance.

Assume that the atoms are located at axial distance z away from the focus of the laser, and the z -axis is designed to pass through the center of the triangle made by the atoms so that the radial distance r would be the same for all three atoms. If $w(z)/r = 5$, the intensity is $I(r, z) = I_0(w_0/w(r))^2 \times 0.923$. Error in the alignment of the axial center z of the laser can cause unequal distances in the radial distance r of the atoms, resulting in different laser intensities at the positions of the atoms. With an error of $\pm 10\%$ in r , the intensity is given by $I(r, z) = I_0(w_0/w(r))^2 \times 0.923^{(1 \pm 0.1)^2}$, and this yields an error of less than 2% in $I(r, z)$.

4.4.2 Numerical simulation

In this section, all the possible errors listed in Sec. 4.4.1 are assembled together and the state preparation is numerically simulated to study the robustness of the

Chapter 4. State preparation of the RFF qubit

scheme. The state preparation schemes for ${}^6\text{Li}$ atoms, ${}^{87}\text{Rb}$ atoms and ${}^{40}\text{Ca}^+$ ions could, in principle, follow the same procedures except that different lasers are used to drive the corresponding transitions. Here, for the numerical simulation we use the system of three ${}^{87}\text{Rb}$ atoms as an example.

First, let us assume perfect optical pumping, that is, initially all the atoms sit in the $|5s_{1/2}, F = 1, m_f = 1\rangle$ ground state. The intermediate excited states are the $5p_{1/2}$ multiplets with a hyperfine level splitting of 814.5MHz, and the $43s_{1/2}$ Rydberg state is used. Therefore, the transitions are driven by lasers with wavelengths at around 780nm and 480nm, which can be easily obtained. The bandwidths of the lasers are assumed to be 1MHz in the simulation. The distance between the atoms are designed to be $1\mu\text{m}$ in the ideal geometry, according to E. (4.13) which requires

$$\cos\theta = \frac{2 \times 780}{1000} \left(n + \frac{1}{3} \right) = 0.52 \quad \text{for } n = 1. \quad (4.33)$$

Error parameters used in the simulation are chosen according to the previous analysis: 5% in the control of total laser intensities, 2% of the difference in the field intensities at the positions of the atoms, 1° in the incident angles of the trapping and optical dressing laser beams, 5% in the distances between atoms R_{12} , R_{13} and R_{23} , 5% in the laser pulse durations and 5% in the position control of the three atoms as a whole.

The two-atom states with the smallest Förster defect to the state $|43s, 43s\rangle$ are states $|43p, 42p\rangle$ and $|42p, 43p\rangle$, which are of energy 5.5GHz lower (the Rydberg level energy is computed with the quantum defect given in [90] and [91]). In Fig. 4.14, the fine-structure splitting of the $43p, 42p$ pair of states is in the order of 0.1GHz which is much smaller than the Förster defect to state $|43s, 43s\rangle$. Thus, the fine structure can be neglected for computing the Rydberg interaction. The next nearest pairs of states are $|44p, 41p\rangle$ and $|47p, 39p\rangle$ whose energy is more than 20GHz lower than the $|43s, 43s\rangle$ state. The Rydberg interaction for state $|43s, 43s\rangle$ is of the van der Waals type which is inversely proportional to the Förster defect between the pair of states, thus for simplicity, we neglect the interaction due to other pairs of states

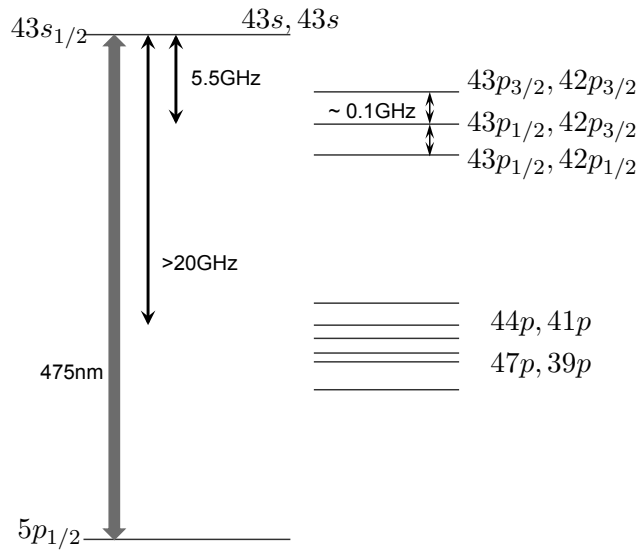


Figure 4.14: Two-atom energy level structure near the $|43s, 43s\rangle$ state.

and only consider the interaction with the $43p, 42p$ levels with the coupling channel

$$s_{1/2} + s_{1/2} \rightarrow p + p. \quad (4.34)$$

The reduced dipole matrix elements of the Rydberg states are numerically computed based on the algorithm given in [92]:

$$R_{43s}^{43p} = 1851.6a_0 \quad \text{and} \quad R_{43s}^{42p} = 1660.9a_0, \quad (4.35)$$

where a_0 is the Bohr radius. There is no strong resonant coupling for the $43s$ state and the dominant second order van der Waals interaction causes an energy shift of the doubly excited state of

$$\Delta E \approx 2 \frac{C^2}{\Delta_F} = 2\mathcal{D} \frac{C_6}{R^6}, \quad (4.36)$$

where

$$C_6 = -\frac{e^4}{\Delta_F} (R_{43s}^{43p} R_{43s}^{42p})^2 \quad (4.37)$$

and \mathcal{D} counts for the Clebsh-Gordan coefficient of the coupling between states. The

dipole-dipole coupling for this particular channel is isotropic and $\mathcal{D} = 2/3$ [88]. The computed Rydberg blockade energy yields

$$\Delta E \approx 2.3h\text{GHz}. \quad (4.38)$$

For the three-atom system, we take the energy shift of the triply excited Rydberg state to be 3GHz for the numerical simulation. It is slightly higher than ΔE given in Eq. (4.38) because the van der Waals interaction is additive and the presence of the third atom nearby would add efficiency to the blockade.

With lasers of coupling strength $\Omega_0 = 120\text{MHz}$ and $\Omega_1 = 80\text{MHz}$ for the transitions $|5s\rangle \rightarrow |5p_{1/2}\rangle$ and $|5p_{1/2}\rangle \rightarrow |43s\rangle$ respectively, and a detuning of $\Delta = 800\text{MHz}$ to the $5p_{1/2}$ state, we simulate the evolution of the Rydberg excitation. The population of the states after a 2π excitation pulse is shown in Fig. 4.15.

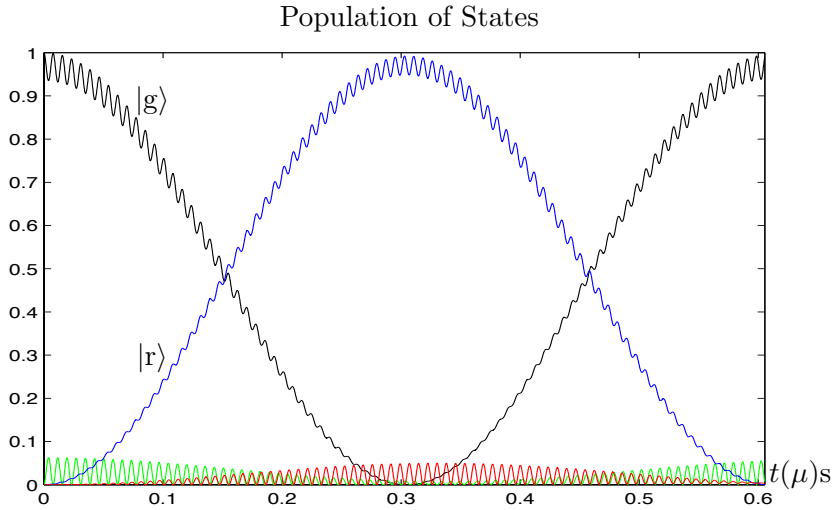


Figure 4.15: The population of the states during a 2π excitation pulse, for $\Delta = 800\text{MHz}$, $\Omega_0 = 120\text{MHz}$ and $\Omega_1 = 80\text{MHz}$. The black curve shows the population of the ground state $|ggg\rangle$; the blue curve shows the population of the collective single-Rydberg-excitation state; the green curve shows the population of the state with a single collective excitation to the intermediate $5p_{1/2}$ state; the red curve shows the population of states with one atom excited to $43s_{1/2}$ and one atom excited to $5p_{1/2}$. The populations of the other states are very small and not shown on this plot.

As a result, the period of the effective Rabi oscillation between the ground state and the single-Rydberg-excitation state is about 600ns; more details about this effective Rabi oscillation will be discussed in Chapter 5. The fidelity of preparing state $|0\rangle + |1\rangle$ for 200 numerical simulations of the random noise model discussed in Sec. 4.4.1 is given in Fig. 4.16.

4.4. Robustness of RFF State Preparation

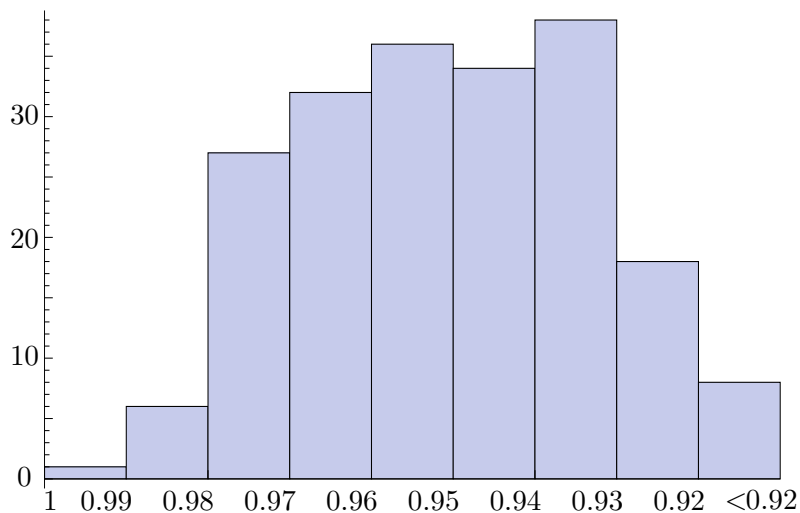


Figure 4.16: Frequency histogram for the fidelities of the state preparation over 200 numerical simulations. The errors of the parameters are randomly selected from normal distributions with the error ranges stated in this section.

The fidelity of the state preparation is above 90% with this set of parameters, as it is shown in Fig. 4.16. Although the error is designed to be selected from a random normal distribution, the distribution of fidelity does not follow a normal distribution, but it is rather uniformly distributed between 93% and 98%. This is because the overall error in the state preparation is dominated by the errors in the control of the Rabi oscillations. The population of the singly excited Rydberg state oscillates quickly with an amplitude of a few percent around half of the Rabi oscillation period. Thus, a small error in the pulse duration can vary the state population by a few percent. Indeed, if we assume perfect Rabi flopping between the ground state and the Rydberg excitation, the fidelity of state is close to a normal distribution around 99%.

To improve on the fidelity, we can either use lasers with weaker intensity or increase the detuning Δ of the $5p_{1/2}$ state to decrease the amplitude of the small but fast oscillation due to the excitation of state $5p_{1/2}$. For the next set of numerical simulation, the atom-light coupling strengths are reduced to $\Omega_0 = 80\text{MHz}$ and $\Omega_1 = 40\text{MHz}$, while the detuning $\Delta = 800\text{MHz}$ remains the same. The population of the states during a 2π excitation pulse and the fidelity of preparing the same state $|0\rangle + |1\rangle$ is shown in Fig. 4.17.

The period of the effective Rabi oscillation between the ground state and the

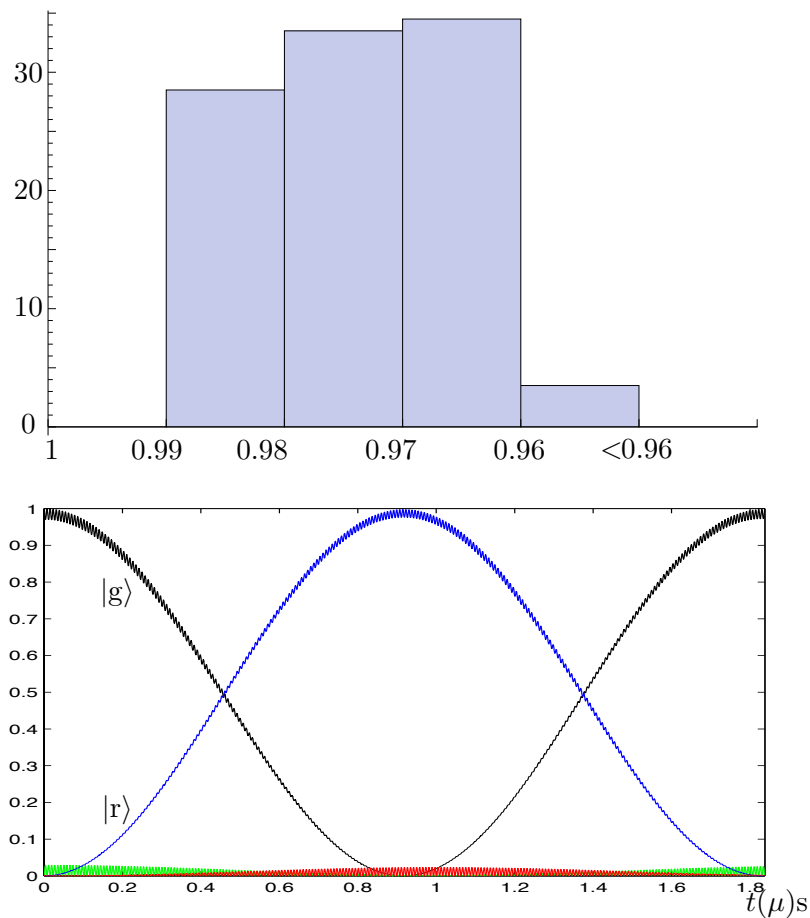


Figure 4.17: The upper plot shows frequency histogram of the fidelities of preparing state $|0\rangle + |1\rangle$ over 100 numerical simulations. The lower plot shows population of the states during a 2π excitation pulse, for $\Delta = 800\text{MHz}$, $\Omega_0 = 80\text{MHz}$ and $\Omega_1 = 40\text{MHz}$. The black curve shows the population of the ground state $|ggg\rangle$; the blue curve shows the population of the collective single-Rydberg-excitation; the green curve shows the population of single collective excitation to the intermediate $5p_{1/2}$ state; and the red curve shows the population of states with one atom excited to $43s_{1/2}$ and one atom excited to $5p_{1/2}$.

single Rydberg excitation is about $1.8\mu\text{s}$. On top of the slow effective Rabi oscillation, there is an oscillation of a much larger frequency and much smaller amplitude than the population curve shown in Fig. 4.15. The fidelity of the state preparation scatters around 96% to unity as shown by the numerical simulation. This verifies that the fidelity improves as $|\Omega/\Delta|$ decreases. We conclude that the scheme of the state preparation is quite robust, as justified by our numerical simulation.

4.5 Summary

In this section, we studied briefly the Rydberg-blockade mechanism and applied this mechanism to the RFF state preparation procedure. The general scheme of the RFF state preparation requires three basic steps, namely, initializing the population to the same hyperfine sub-level by optical pumping, a collective single Rydberg excitation and a deexcitation of the Rydberg population to an initially non-populated hyperfine sub-level. The preparation scheme for the RFF states constructed from trios of ${}^6\text{Li}$ atoms, ${}^{87}\text{Rb}$ atoms or ${}^{40}\text{Ca}^+$ ions is discussed respectively, taking their specific energy level structures into account. As an example for the robustness analysis, we studied the robustness the state preparation numerically for a system of three ${}^{87}\text{Rb}$ atoms in an optical lattice with modest estimations of experimental errors. The numerical simulation shows that the state preparation scheme is quite robust with a minimum fidelity of about 96%.

Raman-type Transitions

Atomic and molecular systems can be coupled in various ways, so that the atomic states evolve and the populations of states change. Of all the electromagnetic multipole couplings, the electric dipole is the strongest. Thus optically allowed atomic transitions are often stimulated by the electric dipole coupling between the atom and a well-controlled laser.

Dipole-allowed transitions can be driven with optical lasers directly. It is, however, quite common that the desired transition is dipole forbidden or the transition frequency is outside of the popular optical range. Then some intermediate state can assist in an indirect transition. Examples for such processes include three-level Raman transitions [66], multi-level Raman transitions [67, 68], and stimulated Raman adiabatic passage (STIRAP) [69, 70]. They all have their useful applications, with three-level Raman transitions being perhaps the most widely used in a large variety of experiments.

In order to reduce the computational complexity of dealing with large Hilbert spaces, one can decrease the dimensionality of the system by eliminating states that are not populated much or not coupled strongly. For a typical three-level Raman transition, the intermediate state is far off-resonantly coupled to the relevant initial and target states. This enables one to perform the so-called *adiabatic elimination* that gets rid of the less relevant state and yields a two-level effective Hamiltonian. Although the procedure of adiabatic elimination is well understood — see [93] and [94], for instance — it gives a reliable approximation only when the detuning of the intermediate state is much larger than the Rabi frequencies for the coupling to the other two states.

In this chapter, we introduce an alternative approach to the quantitative description of the three-level Raman transition. This new method does not rely on adiabatic elimination and gives a much more accurate solution while the computational complexity remains low [95]. We set the stage in Sec. 5.1, where we briefly review driven three-level systems and state the notational conventions used throughout. Then, Sec. 5.2 deals with the usual adiabatic-elimination approach and comments on its limitations and problems. Our new approach is explained in Sec. 5.3: First we present the general methodology, then we show how it gives the exact solution to the on-resonant two-photon transition problem, and finally we generate reliable approximations for the situation of an off-resonant two-photon transition. Last, in Sec. 5.4, we apply this new method to multi-atom Rydberg excitation that is of higher dimension than the single-atom three-level system.

5.1 The three-level system

A Raman transition is a two-photon process that gives an effective coupling between two states $|0\rangle$ and $|1\rangle$ via a far-detuned auxiliary state $|e\rangle$; see Fig. 5.1. As mentioned above, Raman transitions are often used when the transition between levels $|0\rangle$ and $|1\rangle$ is dipole forbidden or has an inconvenient frequency. The Λ -type level configuration of Fig. 5.1(a) applies to transitions between different ground states via an excited state; the cascade-type configuration of Fig. 5.1(b) can be used to achieve the transition between a ground state and a highly excited state, such as a Rydberg state. There is also a V-type transition with the level configuration similar to that of an inverted Λ -type transition. Although the level structures are different for these two configurations, the underlying physics is essentially the same.

We will, therefore, restrict ourselves to treating the Λ -type Raman transition in detail. With reference to $|0\rangle$, $|1\rangle$, and $|e\rangle$ in this order, the 3×3 matrix for the Hamiltonian of the system is

$$H = H_{\text{Atom}} + H_{\text{AL}}, \quad (5.1)$$

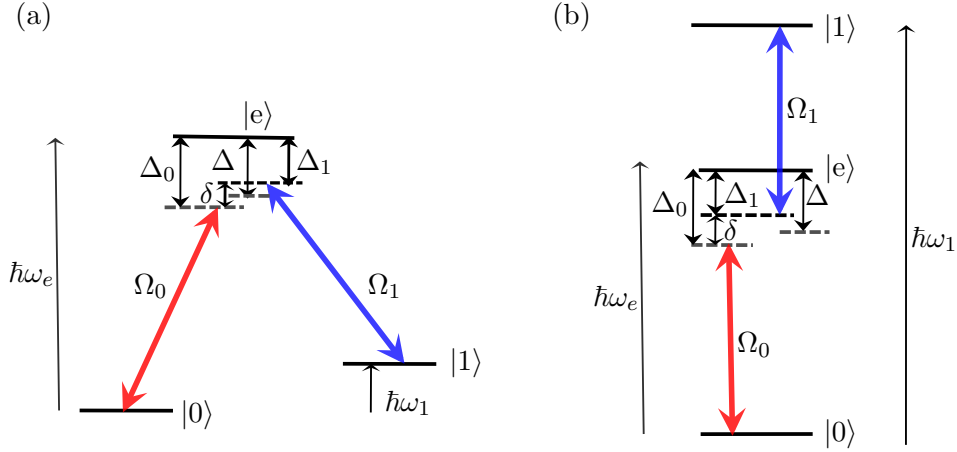


Figure 5.1: Level scheme of a typical Raman transition. (a) shows the level structure of a Λ -type Raman transition and (b) shows the level structure of a cascade-type Raman transition. Ω_0 and Ω_1 denote the Rabi frequencies of the individual two-level transitions, Δ denotes the detuning of the laser from the transition frequency of the excited state and δ is the detuning of the two-photon transition. The requirement is that the detuning Δ is much larger than the Rabi frequencies so that the excited state $|e\rangle$ is not significantly populated.

where

$$H_{\text{Atom}} = \hbar \begin{pmatrix} 0 & 0 & 0 \\ 0 & \omega_1 & 0 \\ 0 & 0 & \omega_e \end{pmatrix} \quad (5.2)$$

is the part for the atom by itself with the convention that the state $|0\rangle$ has energy zero, and

$$H_{\text{AL}} = \frac{\hbar}{2} \begin{pmatrix} 0 & 0 & \Omega_0 e^{i\omega_{L0}t} \\ 0 & 0 & \Omega_1 e^{i\omega_{L1}t} \\ \Omega_0^* e^{-i\omega_{L0}t} & \Omega_1^* e^{-i\omega_{L1}t} & 0 \end{pmatrix} \quad (5.3)$$

accounts for the atom-laser interaction. The laser frequencies are denoted by ω_{L0} and ω_{L1} , respectively. The Rabi frequencies for the electric-dipole transitions are

$$\Omega_0 = \frac{q_{\text{el}}}{\hbar} \langle 0 | \mathbf{r} \cdot \mathbf{E}_{L0} | e \rangle \quad \text{and} \quad \Omega_1 = \frac{q_{\text{el}}}{\hbar} \langle 1 | \mathbf{r} \cdot \mathbf{E}_{L1} | e \rangle, \quad (5.4)$$

where q_{el} is the electron charge, \mathbf{E}_{L0} and \mathbf{E}_{L1} are the amplitudes of the electric fields of the laser beams and \mathbf{r} is the position vector of the atom. Each Rabi frequency depends on the intensity and polarization of the corresponding laser as well as the dipole matrix element between the two coupled states, and can be

Chapter 5. Raman-type Transitions

complex. Typically, the detuning Δ is designed to be large, i.e., $|\Delta| \gg |\Omega_0|, |\Omega_1|$, so that the auxiliary state $|e\rangle$ does not get populated to avoid problems arising from uncontrolled spontaneous emission from $|e\rangle$ to other states; see Fig. Eq. (5.1). Since the two-photon transition from $|0\rangle$ to $|1\rangle$ is nearly resonant, the overall detuning δ of the two-photon transition is small compared with the average detuning Δ , $|\delta/\Delta| \ll 1$. If the detunings between the lasers and the atomic frequencies are denoted by $\Delta_0 = \omega_e - \omega_{L0}$ and $\Delta_1 = \omega_e - \omega_1 - \omega_{L1}$, respectively, we have $\Delta = (\Delta_0 + \Delta_1)/2$ and $\delta = \Delta_0 - \Delta_1$.

In view of the time-dependent phase factors in H_{AL} it is expedient to switch to an interaction picture in which the Hamiltonian does not depend on time. This is achieved by identifying the “free” Hamiltonian H_0 by a suitable splitting of the atomic Hamiltonian,

$$H_0 = H_{\text{Atom}} + \hbar \begin{pmatrix} \frac{1}{2}\delta & 0 & 0 \\ 0 & -\frac{1}{2}\delta & 0 \\ 0 & 0 & -\Delta \end{pmatrix} = \hbar \begin{pmatrix} \frac{1}{2}\delta & 0 & 0 \\ 0 & \omega_1 - \frac{1}{2}\delta & 0 \\ 0 & 0 & \omega_e - \Delta \end{pmatrix}, \quad (5.5)$$

for which we obtain the interaction-picture Hamiltonian

$$H_I = e^{iH_0 t/\hbar} (H - H_0) e^{-iH_0 t/\hbar} = \frac{\hbar}{2} \begin{pmatrix} -\delta & 0 & \Omega_0 \\ 0 & \delta & \Omega_1 \\ \Omega_0^* & \Omega_1^* & 2\Delta \end{pmatrix}. \quad (5.6)$$

The evolution of the three-level system is then studied with the aid of the Schrödinger equation

$$i\hbar \frac{\partial}{\partial t} \Psi_I(t) = H_I \Psi_I(t) \quad \text{with} \quad \Psi_I(t) = \begin{pmatrix} c_0(t) \\ c_1(t) \\ c_e(t) \end{pmatrix} = e^{iH_0 t/\hbar} \Psi(t), \quad (5.7)$$

where the components of $\Psi_I(t)$ are the interaction-picture probability amplitudes for $|0\rangle$, $|1\rangle$, and $|e\rangle$, related to the respective components of $\Psi(t)$ by simple time-

dependent phase factors. As a consequence of this simple relation among the components of $\Psi(t)$ and $\Psi_I(t)$, we can simply square $c_0(t)$, $c_1(t)$, or $c_e(t)$ to obtain the probability amplitudes for the respective atomic levels, as exemplified by the probability for $|0\rangle$,

$$\left| \begin{pmatrix} 1 & 0 & 0 \end{pmatrix} \Psi(t) \right|^2 = \left| \begin{pmatrix} 1 & 0 & 0 \end{pmatrix} \Psi_I(t) \right|^2 = |c_0(t)|^2, \quad (5.8)$$

where, of course, $(1 \ 0 \ 0)$ is the three-component row for $\langle 0|$.

To understand the system analytically, we can solve for the eigensystem of this time-independent Hamiltonian directly. However, very often, this is neither the most efficient way of getting the solution, nor the best method for obtaining a good physical insight into the system. Various approaches have been developed, of which the adiabatic elimination and, for $\delta = 0$, the dark-state method [96] are particularly useful and popular.

5.2 Adiabatic Elimination

5.2.1 The methodology

The standard textbook approach to the Raman transition problem makes use of “adiabatic elimination” in accordance with the following line of reasoning. Since the excited state $|e\rangle$ is far-detuned by Δ , it will remain barely populated if it has no initial population. Thus, the change of the population in this state can be taken as approximately zero, $\frac{\partial}{\partial t}c_e(t) = 0$, so that

$$2i\frac{\partial}{\partial t}c_e(t) = \Omega_0^*c_0(t) + \Omega_1^*c_1(t) + 2\Delta c_e(t) = 0, \quad (5.9)$$

in view of the Schrödinger equation Eq. (5.7). We can now express $c_e(t)$ as a linear combination of $c_0(t)$ and $c_1(t)$, and so eliminate $c_e(t)$ from the equations of motion for $c_0(t)$ and $c_1(t)$. This gives us an effective 2×2 Hamiltonian for the evolution

Chapter 5. Raman-type Transitions

of the two relevant states

$$H_{\text{eff}} = -\frac{\hbar}{2} \begin{pmatrix} \delta + \frac{|\Omega_0|^2}{2\Delta} & \frac{\Omega_0\Omega_1^*}{2\Delta} \\ \frac{\Omega_1\Omega_0^*}{2\Delta} & -\delta + \frac{|\Omega_1|^2}{2\Delta} \end{pmatrix} \quad (5.10)$$

$$\text{for } i\hbar \frac{\partial}{\partial t} \psi(t) = H_{\text{eff}} \psi(t) \quad \text{with } \psi(t) = \begin{pmatrix} c_0(t) \\ c_1(t) \end{pmatrix}.$$

As an immediate benefit of applying adiabatic elimination on the intermediate auxiliary state, the effective Hamiltonian is a simple 2×2 matrix, for which the eigenvalues and the projectors to the eigenspaces are readily available.

The eigenvalues of H_{eff} are

$$E_{\pm} = -\frac{\hbar}{8\Delta} (|\Omega_0|^2 + |\Omega_1|^2) \pm \frac{\hbar}{2} \Omega_{\text{R}} \quad (5.11)$$

with the positive frequency Ω_{R} given by

$$\Omega_{\text{R}}^2 = \frac{1}{(4\Delta)^2} (|\Omega_0|^2 + |\Omega_1|^2)^2 + \frac{\delta}{2\Delta} (|\Omega_0|^2 - |\Omega_1|^2) + \delta^2. \quad (5.12)$$

The projectors to the corresponding eigenspaces are $\frac{1}{2}(1 \pm \sigma_o)$, where

$$\sigma_o = \frac{2H_{\text{eff}} - E_+ - E_-}{E_+ - E_-} \quad (5.13)$$

is a Pauli-type matrix. If the evolution starts with all the population in the ground state $|0\rangle$, i.e., $c_0(t=0) = 1$, the population in state $|1\rangle$ at a later time t is

$$|c_1(t)|^2 = \frac{|\Omega_0|^2 |\Omega_1|^2}{8\Delta^2 \Omega_{\text{R}}^2} [1 - \cos(\Omega_{\text{R}} t)]. \quad (5.14)$$

This tells us the physical significance of $\Omega_{\text{R}} = (E_+ - E_-)/\hbar$: It is the effective Rabi frequency of the transition between states $|0\rangle$ and $|1\rangle$ via this Raman process.

In the situation of a resonant Raman transition, $\delta = 0$, we have

$$|c_1(t)|^2 = \frac{2|\Omega_0|^2 |\Omega_1|^2}{(|\Omega_0|^2 + |\Omega_1|^2)^2} \left[1 - \cos\left(\frac{|\Omega_0|^2 + |\Omega_1|^2}{4\Delta} t\right) \right], \quad (5.15)$$

where the effective Rabi frequency is $\Omega_R = (|\Omega_0|^2 + |\Omega_1|^2)/(4|\Delta|)$ and the amplitude of the Rabi oscillation is less than unity,

$$\frac{4|\Omega_0|^2|\Omega_1|^2}{(|\Omega_0|^2 + |\Omega_1|^2)^2} < 1, \quad (5.16)$$

unless $|\Omega_0|^2 = |\Omega_1|^2$. In other words, when $\delta = 0$, we get complete population transfer between state $|0\rangle$ and state $|1\rangle$ only if the two lasers drive the respective transitions equally strongly.

More generally, perfect population transfer from $|0\rangle$ to $|1\rangle$ is only possible if the two diagonal matrix elements of the effective Hamiltonian are identical, i.e., if there is no effective detuning after the adiabatic elimination. Then $|0\rangle$ and $|1\rangle$ are equal-weight superpositions of the eigenstates of H_{eff} and temporal evolution turns one into the other. For given laser intensities, and thus given Rabi frequencies Ω_0 and Ω_1 , the experimenter can exploit the Zeeman or the Stark effect to adjust the overall detuning such that

$$\delta = \frac{|\Omega_1|^2 - |\Omega_0|^2}{4\Delta}. \quad (5.17)$$

This makes the effective detuning vanish and ensures perfect population transfer. Indeed, for this value of δ , the right-hand side of Eq. (5.14) simplifies,

$$|c_1(t)|^2 = \frac{1}{2}[1 - \cos(\Omega_R t)] \quad \text{with} \quad \Omega_R = \frac{|\Omega_0||\Omega_1|}{2|\Delta|}. \quad (5.18)$$

In experiments, specifically for two-photon population transfer from the ground state to a Rydberg state where the Rabi frequencies $|\Omega_0|$ and $|\Omega_1|$ can be an order of magnitude different in strengths, adjusting the detuning in accordance with Eq. (5.17) is important [97].

5.2.2 Light shift

When an atomic transition is driven by an electromagnetic radiation field with detuning Δ , the dressed atomic levels are shifted. This is the so-called ‘‘light shift’’ of the atomic levels, which is a second-order correction to the eigenenergies of

Chapter 5. Raman-type Transitions

the Hamiltonian [98]. If an atomic transition is driven by Rabi frequency Ω with detuning Δ , the light shift of the ground state of the transition is $-|\Omega|^2/(4\Delta)$ and the light shift of the dressed excited state is of the same amount but opposite in sign. The overall light shift is a direct summation of the light shifts arising from individual electromagnetic radiation fields, when the atomic level is addressed by multiple fields.

In the present context, the light shift of state $|0\rangle$ is $\hbar\delta_0 = -\hbar|\Omega_0|^2/(4\Delta_0)$ and the light shift of state $|1\rangle$ is $\hbar\delta_1 = -\hbar|\Omega_1|^2/(4\Delta_1)$. Thus, the value of δ that brings the two-photon transitions into resonance is determined by the equation

$$\delta = \frac{|\Omega_1|^2}{4\Delta + 2\delta} - \frac{|\Omega_0|^2}{4\Delta - 2\delta}, \quad (5.19)$$

which is solved by

$$\delta \simeq \frac{2\Delta(|\Omega_1|^2 - |\Omega_0|^2)}{8\Delta^2 + |\Omega_0|^2 + |\Omega_1|^2} + \dots, \quad (5.20)$$

where the ellipsis stands for terms of relative size $|\Omega/\Delta|^2$ or smaller. The difference between the δ values obtained from Eq. (5.17) and Eq. (5.20) can be of the order of a percent ($\sim (|\Omega_0|^2 + |\Omega_1|^2)/(64\Delta^2)$). But the approximate solutions provided by the adiabatic-elimination method do not depend much on this small fractional difference in δ . Figure 5.2 shows the fidelity between the states at later times using the two different expressions of δ when the initial state is $|0\rangle$.

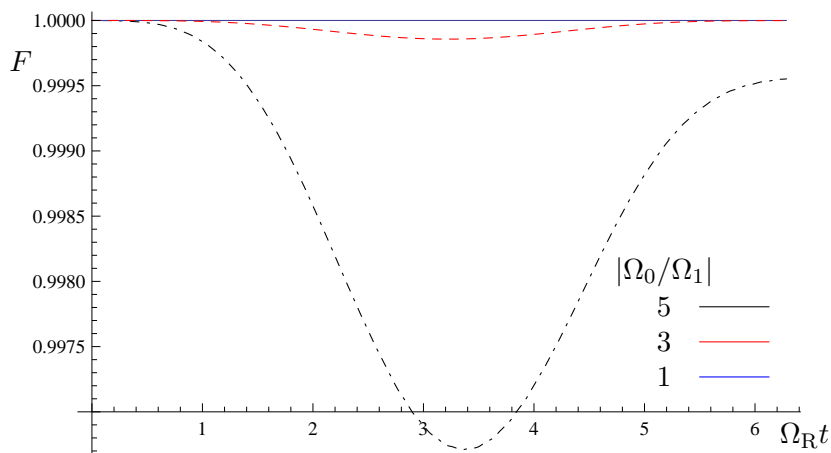


Figure 5.2: Fidelity between the two states at later times evolving with the exact Hamiltonian but taking different δ values given by Eq. (5.17) and Eq. (5.20). $\Delta = 400\text{MHz}$ and $|\Omega_1| = 40\text{MHz}$ are fixed and there different curves are for different ratio of $|\Omega_0/\Omega_1|$.

The effect of using these two different expressions for δ is small when the difference between $|\Omega_0|$ and $|\Omega_1|$ is not too large. For the cases shown in Fig. 5.2, the error from using Eq. (5.17) is a small fraction of a percent. This explains why Eq. (5.17) can serve as a good guidance for experiments, although one should prefer the more accurate relation Eq. (5.20).

5.2.3 Problems with adiabatic elimination

In physics, one speaks of an “adiabatic process” if a relevant property evolves quite slowly, whereas other processes are fast — a clear separation of times scales is a defining element. In the context of adiabatic elimination, one invokes such a separation in the evolution of the components of $\Psi_I(t)$, for which we have the Schrödinger equation in Eq. (5.7). One standard argument observes that, as a consequence of $|\Delta| \gg |\Omega_0|, |\Omega_1|$, the amplitude $c_e(t)$ will undergo many oscillations during a period in which $c_0(t)$ and $c_1(t)$ do not change substantially. Then, if our interest is not in the short-time changes that would reveal the rapid oscillations of $c_e(t)$ but predominantly in the longer-time changes of $c_0(t)$ and $c_1(t)$, the average change of $c_e(t)$ over these longer periods is expected to be quite small. In the spirit of this reasoning, we should then read Eq. (5.9) as a statement about coarse-grained values of the probability amplitudes.

This is hardly a rigorous argument, and whether one regards it as convincing or not is largely a matter of taste. Clearly, though, a more solid argument would be welcome, and one has been provided in [94]. Indeed, the reasoning in [94] uses coarse graining in conjunction with a Markov approximation.

There are other problems that one needs to keep in mind when employing adiabatic elimination. We present them as four questions.

- (i). Which is the correct interaction picture to use? The theory argues that the change of the (coarse-grained) population in the excited state is approximately zero and we arrived at Eq. (5.9) by using the Schrödinger’s equation of motion with the time-independent Hamiltonian H_I in Eq. (5.6). However, the choice of interaction picture is not unique and why do we apply the adiabatic elimi-

nation in this particular interaction picture instead of another? For example, by adding a constant term, the operator $H_I + E$ describes the system equally well. But if we use an interaction picture with $E \neq 0$, the resultant two-level effective Hamilton operator also changes as Δ gets replaced by $\Delta + E/\hbar$ in Eq. (5.10) with consequential changes in the evolution of $\psi(t)$.

This ambiguity in the choice of interaction picture was studied by Brion, Pedersen, and Mølmer with a Green's function formalism [93]. It would be premature, however, to claim that the case is closed. Further studies of the choice of interaction picture and a systematic way of performing the adiabatic elimination are presented in a paper by Paulisch *et al* [94].

- (ii). Is it possible to estimate the population in the eliminated state? This does not have a simple answer because there are problems with the normalization of the wave function. Originally, we have $\Psi_I(t)^\dagger \Psi_I(t) = 1$. Then, since H_{eff} is Hermitian, we also have $\psi(t)^\dagger \psi(t) = 1$. Combined with the initial condition $(c_0, c_1, c_e) = (1, 0, 0)$ this implies $c_e(t) = 0$ for all t , which contradicts the basic approximation in Eq. (5.9).
- (iii). Is it possible to regard the adiabatic-elimination approximation as the first in a hierarchy of approximations? This is possible, indeed, as discussed in [94]. It turns out that the next approximation in the hierarchy gives a substantial improvement and better quantitative estimates. In addition, it provides an answer to the previous question inasmuch as the next approximation provides an estimate for the population in the auxiliary state.
- (iv). Is it possible to avoid the adiabatic elimination without increasing the complexity much beyond the convenient two-level description of Eq. (5.10)? Yes, this is possible, as we demonstrate in Section 5.3.

5.3 Without adiabatic elimination

Alternative methods other than adiabatic elimination are also used to solve Raman transition problems. The most direct way is, of course, to diagonalize the interaction-picture Hamiltonian of Eq. (5.6), and this can be done by hand since the dimensionality of the system is quite small. But the expressions for the eigenvalues and eigencolumns of H_I are quite involved and not transparent. An exception is the resonant two-photon transition, $\delta = 0$, when one can identify a dark state and use it to reduce the three-level system to an effective two-level system, which can then be solved exactly rather simply. The dark states are particularly useful in the context of adiabatic population transfer and electromagnetically induced transparency. When the two-photon transition is not resonant, however, there is no dark state. Methods of perturbation theory can then be used to find corrections for a small detuning δ , but the complexity grows quickly when high accuracy is required.

In this section, we provide a new way of solving the Raman transition problem. Just like the dark-state method, it gives a compact exact solution for $\delta = 0$, and it can solve the off-resonant case with very high precision and rather little extra effort.

5.3.1 General methodology

It will be expedient to use a different interaction picture as the one of Eq. (5.5) and Eq. (5.6) that we used for the adiabatic elimination in Sec. 5.2.1. Instead, we choose

$$H_0 = \frac{\hbar}{2} \begin{pmatrix} \Delta + \delta & 0 & 0 \\ 0 & 2\omega_1 + \Delta - \delta & 0 \\ 0 & 0 & 2\omega_e - \Delta \end{pmatrix}, \quad (5.21)$$

and the Hamiltonian in this interaction picture is

$$H_I = \frac{\hbar}{2} \begin{pmatrix} -\Delta - \delta & 0 & \Omega_0 \\ 0 & -\Delta + \delta & \Omega_1 \\ \Omega_0^* & \Omega_1^* & \Delta \end{pmatrix} = \frac{\hbar}{2} \begin{pmatrix} -(\Delta + \delta\sigma_3) & \Omega \\ \Omega^\dagger & \Delta \end{pmatrix}, \quad (5.22)$$

Chapter 5. Raman-type Transitions

where the latter way of writing emphasizes the $3 = 2 + 1$ split into two relevant states and one auxiliary state; σ_3 is the standard third Pauli 2×2 matrix, and Ω and Ω^\dagger are the two-component column of Rabi frequencies,

$$\Omega = \begin{pmatrix} \Omega_0 \\ \Omega_1 \end{pmatrix}, \quad (5.23)$$

and its adjoint row. This change of interaction picture is equivalent to shifting the energy levels of the interaction-picture Hamiltonian in Eq. (5.6) by $-\hbar\Delta/2$, an example of the freedom of choice discussed in question (i) in Section 5.2.3.

We note that the square of H_I ,

$$H_I^2 = (\hbar M)^2 = \hbar^2(M_0^2 + \epsilon), \quad (5.24)$$

is the sum of a “big” block-diagonal part,

$$M_0^2 \equiv \frac{1}{4} \begin{pmatrix} (\Delta + \delta\sigma_3)^2 + \Omega\Omega^\dagger & 0 \\ 0 & \Delta^2 + \Omega^\dagger\Omega \end{pmatrix}, \quad (5.25)$$

and a “small” off-diagonal part

$$\epsilon \equiv -\frac{\delta}{2} \begin{pmatrix} 0 & \sigma_3\Omega \\ \Omega^\dagger\sigma_3 & 0 \end{pmatrix}. \quad (5.26)$$

Matrix M denotes a square root of the matrix $(H_I/\hbar)^2$ and, since for each eigenvalue we have a choice of sign, there are many M s that are equally good. Any one can be used as a replacement of H_I/\hbar in even functions of H_I ; for example, we could choose $M > 0$ by convention. In particular, then, the unitary evolution matrix in this interaction picture can be written as

$$U(t) = e^{-iH_I t/\hbar} = \cos(Mt) - \frac{i}{\hbar} \frac{\sin(Mt)}{M} H_I. \quad (5.27)$$

Except for the common physical approximations that enter the modeling of the

atom-laser system by a driven three-level system described by the Hamiltonian of Eq. (5.1)–Eq. (5.3), this is an exact 3×3 matrix representing the evolution operator.

Instead of diagonalizing the interaction-picture Hamiltonian Eq. (5.22), we can determine the eigenvalues and eigencolumns of M^2 , whose “big plus small” structure, together with the block-diagonal form of M_0^2 , facilitates approximations. We will see the advantage thereof shortly. Let us note that we can position the factor H_I in the second term of the right-hand-side of Eq. (5.27) equally well to the left of $\sin(Mt)/M$, or break up $\sin(Mt)/M$ and sandwich H_I between even powers of M . Since $[H_I, M^2] = 0$, such a change in the order of the matrices makes no difference in Eq. (5.27), but slightly different expressions are obtained when approximations are introduced for the trigonometric functions of M .

5.3.2 Resonant two-photon transitions ($\delta = 0$) — exact solution

When $\delta = 0$, we have $\epsilon = 0$ and

$$M = M_0 = \frac{1}{2} \begin{pmatrix} -\sqrt{\Delta^2 + \Omega\Omega^\dagger} & 0 \\ 0 & \sqrt{\Delta^2 + \Omega^\dagger\Omega} \end{pmatrix}, \quad (5.28)$$

where the signs are chosen such that $M \rightarrow H_I/\hbar$ in the $\Omega \rightarrow 0$ limit. The resulting evolution operator Eq. (5.27) reads

$$U(t) = \cos(M_0 t) - \frac{i}{\hbar} \frac{\sin(M_0 t)}{M_0} H_I. \quad (5.29)$$

Owing to the block-diagonal structure of M_0 , the original 3×3 problem has been converted into an equivalent 2×2 problem without introducing any approximation. Clearly, the technical difficulty has been significantly reduced!

The column Ω is an eigencolumn of $\Delta^2 + \Omega\Omega^\dagger$ with eigenvalue $\Delta^2 + \Omega^\dagger\Omega$, so that

$$M_0^2 = \frac{1}{4} (\Delta^2 + \Omega^\dagger\Omega) \begin{pmatrix} \frac{\Omega\Omega^\dagger}{\Omega^\dagger\Omega} & 0 \\ 0 & 1 \end{pmatrix} + \frac{1}{4} \Delta^2 \begin{pmatrix} 1 - \frac{\Omega\Omega^\dagger}{\Omega^\dagger\Omega} & 0 \\ 0 & 0 \end{pmatrix} \quad (5.30)$$

is the spectral decomposition of M_0^2 . This gives

$$\cos(M_0 t) = \cos\left(\sqrt{\Delta^2 + \Omega^\dagger \Omega} t/2\right) \begin{pmatrix} \frac{\Omega \Omega^\dagger}{\Omega^\dagger \Omega} & 0 \\ 0 & 1 \end{pmatrix} + \cos(\Delta t/2) \begin{pmatrix} 1 - \frac{\Omega \Omega^\dagger}{\Omega^\dagger \Omega} & 0 \\ 0 & 0 \end{pmatrix} \quad (5.31)$$

and likewise for $\sin(M_0 t)$ in Eq. (5.29). Hence, the exact evolution of the system can be written out analytically. In particular, the population in the excited state $|e\rangle$ is non-zero. With the atom initially in the ground state $|0\rangle$, it is

$$|c_e(t)|^2 = \left| \begin{pmatrix} 0 & 0 & 1 \end{pmatrix} U(t) \begin{pmatrix} 1 \\ 0 \\ 0 \end{pmatrix} \right|^2 = \frac{|\Omega_0|^2}{\Delta^2 + \Omega^\dagger \Omega} \sin\left(\sqrt{\Delta^2 + \Omega^\dagger \Omega} t/2\right)^2. \quad (5.32)$$

This exact expression shows that the population in the excited state oscillates with (angular) frequency $\frac{1}{2}(\Delta^2 + \Omega^\dagger \Omega)^{1/2}$ and the oscillation amplitude can be non-negligible if $|\Omega_0|^2$ is a sizable fraction of $\Delta^2 + \Omega^\dagger \Omega = \Delta^2 + |\Omega_0|^2 + |\Omega_1|^2$.

We note that the second projection matrix in Eq. (5.30) and Eq. (5.31) projects on the dark state, whose bra has the row $(-\Omega_1 \ \Omega_0 \ 0)$ [96]. An atom prepared in this dark state stays in it, and there is no probability of finding the atom in the excited state at any time. The atom is essentially decoupled from the driving lasers under these circumstances. In this sense, one could regard Eq. (5.29) with Eq. (5.30) as the evolution matrix in the dark-state formalism but this is, in fact, not the case. In the dark-state approach, one diagonalizes H_I , reduced to a two-dimensional problem after putting the dark state aside, which amounts to choosing one particular square root of M_0^2 from the continuous family of square roots that the degenerate eigenvalue makes available, namely the square root whose eigenvalues and eigencolumns are those of H_I/\hbar . No such unique M_0 is needed in Eq. (5.29), nor is there any benefit from enforcing a unique square root of M_0^2 by imposing additional criteria. Although in the $\delta = 0$ case, this equivalence can be established between the new approach and the dark-state approach, the new approach offers more flexibility and it also has a clear advantage when dealing with the $\delta \neq 0$ case,

as we shall see in Section 5.3.3.

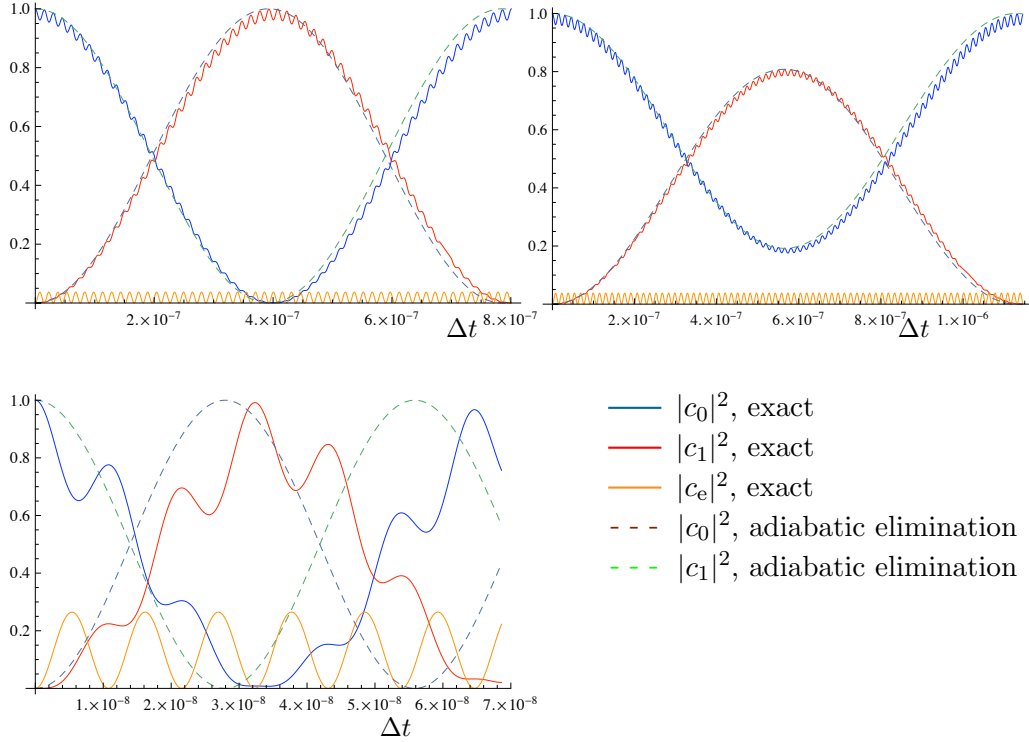


Figure 5.3: Population distribution for a single-atom Raman transition in time when $\delta = 0$. The solid curves show the exact solution, and the dashed curves the adiabatic-elimination approximation. The initial state is $|0\rangle$. The red curves are for the ground-state population $|c_0(t)|^2$, the blue curves for $|c_1(t)|^2$, and the orange curves report $|c_e(t)|^2$, the population in the excited state. The detuning is $\Delta = 400$ MHz for all plots; the top left plot is for $|\Omega_0| = |\Omega_1| = \Delta/10 = 40$ MHz; the top right plot is for $|\Omega_0| = \Delta/10 = 40$ MHz and $|\Omega_1| = \Delta/16 = 25$ MHz; the bottom plot is for $|\Omega_0| = |\Omega_1| = \Delta/4 = 100$ MHz.

For three sets of parameter values, Fig. (5.3) shows the population $|c_e(t)|^2$ of Eq. (5.32) as well as the populations $|c_0(t)|^2$ and $|c_1(t)|^2$ of the relevant states $|0\rangle$ and $|1\rangle$. The populations of $|0\rangle$ and $|1\rangle$ are oscillating with a slow frequency that goes with a large amplitude and a fast frequency that goes with a small amplitude. The population transfer is dominantly controlled by the slow frequency which, therefore, is the effective Rabi frequency of the system. Since M_0^2 has only two distinct eigenvalues, half the sum of their square roots gives the fast frequency and the difference gives the slow frequency. Thus, we have

$$\Omega_R = \frac{1}{2} \left(\sqrt{\Delta^2 + \Omega^\dagger \Omega} - |\Delta| \right) = \frac{\Omega^\dagger \Omega}{4|\Delta|} - \frac{(\Omega^\dagger \Omega)^2}{16|\Delta|^3} + \dots \quad (5.33)$$

for the effective Rabi frequency. The expansion in powers of $|\Omega/\Delta| \ll 1$ permits a comparison of this exact expression with the approximation obtained by adiabatic elimination, the $\delta = 0$ version of Eq. (5.12): The adiabatic-elimination approximation gives the leading term, but does not reproduce any of the higher-order terms.

In summary, we find that the solution from the adiabatic elimination is indeed the zeroth order approximation of the exact result in the expansion of $\Omega^\dagger\Omega/\Delta^2$. For example, in the zeroth order of $\Omega^\dagger\Omega/\Delta^2$, the excited state population vanishes as the oscillation amplitude is proportional to $\Omega^\dagger\Omega/\Delta^2 \sim 0$. We conclude that adiabatic elimination yields a reliable approximation only when $|\Omega_0|, |\Omega_1| \ll |\Delta|$. The difference between the solutions obtained by our method and the adiabatic-elimination approximation is demonstrated clearly in Fig. 5.3.

The top left plot in Fig. 5.3 shows the populations when $|\Omega_0| = |\Omega_1| = \Delta/10$ is small; in this parameter regime, we can already see the deviation of the adiabatic elimination from the exact result but the deviation is not significant. In the top-right plot, the population of state $|1\rangle$ only reaches a maximum of about 80% as $|\Omega_0| \neq |\Omega_1| \sim \Delta/10$ introduces an effective detuning for the two-photon transition; the adiabatic elimination gives a good approximation since we are still in the regime of $|\Omega_0|, |\Omega_1| \ll |\Delta|$. When the magnitudes of $|\Omega_0|$ and $|\Omega_1|$ are not much smaller than $|\Delta|$, the population of the excited state is no longer negligible, but the complete population transfer between states $|0\rangle$ and $|1\rangle$ is still achievable; see the bottom-left plot in Fig. 5.3. The adiabatic elimination method fails in this case of stronger coupling between the relevant states $|0\rangle, |1\rangle$ and the excited state $|e\rangle$.

5.3.3 Non-resonant two-photon transitions ($\delta \neq 0$)

As we discussed in Section 5.2.2, one needs to adjust the detuning δ to compensate for the light shifts and achieve complete population transfer from $|0\rangle$ to $|1\rangle$. Besides this, there can also be other experimental reasons for choosing a particular δ value. Thus, the non-resonant situation of $\delta \neq 0$ is of practical interest, and so we will regard the overall detuning δ as a free parameter that is small compared with the

5.3. Without adiabatic elimination

average detuning Δ . Typically, the ratios δ/Δ and $\Omega^\dagger\Omega/\Delta^2$ are of the same small order, a few percent perhaps.

The splitting of H_1^2 in Eqs. (5.24)–(5.26) has the diagonal blocks in M_0^2 , including the δ -dependent contributions, whereas ϵ contains the off-diagonal parts linear in δ . We shall treat ϵ as a small quantity, without, however, regarding δ as an expansion parameter. Rather, the full δ -dependence of M_0^2 is taken into account. Then, the eigenvalues of M^2 agree with the eigenvalues of M_0^2 to first order in the perturbation of ϵ , and the leading correction will be of order ϵ^2 .

The eigenvalues of M_0^2 in the subspace spanned by $|0\rangle$ and $|1\rangle$ are

$$\mu_{\pm}^2 = \frac{1}{4}(\Delta^2 + \delta^2) + \frac{1}{8}\Omega^\dagger\Omega \pm \frac{1}{8}\sqrt{(\Omega^\dagger\Omega)^2 + 8\delta\Delta\Omega^\dagger\sigma_3\Omega + (4\delta\Delta)^2}, \quad (5.34)$$

which we get from diagonalizing the upper 2×2 diagonal block $(\Delta + \delta\sigma_3)^2 + \Omega\Omega^\dagger$.

The unnormalized eigencolumns are

$$\begin{pmatrix} [4\mu^2 - (\Delta + \delta\sigma_3)^2]\Omega \\ 0 \end{pmatrix} \quad \text{for } \mu^2 = \mu_{\pm}^2, \quad (5.35)$$

unless Ω is an eigencolumn of σ_3 , which is a case of no interest. The eigenvalue $\frac{1}{4}(\Delta^2 + \Omega^\dagger\Omega)$ in the 1×1 block for $|e\rangle$ does not depend on δ . With its eigenvalues and eigencolumns at hand, all functions of M_0^2 are readily evaluated.

In passing, we observe that the difference between μ_+^2 and μ_-^2 is smallest, as a function of δ , when Eq. (5.17) holds, i.e., $4\delta\Delta = -\Omega^\dagger\sigma_3\Omega$. Then

$$\mu_+^2 - \mu_-^2 = \frac{1}{4}\sqrt{(\Omega^\dagger\Omega)^2 - (\Omega^\dagger\sigma_3\Omega)^2} = \frac{|\Omega_0||\Omega_1|}{2}, \quad (5.36)$$

which is nonzero in all situations of interest.

For a systematic inclusion of correction of orders ϵ , ϵ^2 , ϵ^3 , \dots , we do not use the perturbation theory for an approximation of the eigenvalues and eigencolumns of M^2 for use in Eq. (5.27). Rather, we generate approximations for the evolution matrix $U(t) = \exp(-iH_1t/\hbar)$ itself with the aid of an equation of Lippmann-Schwinger

Chapter 5. Raman-type Transitions

type,

$$U(t) = U_0^{(R)}(t) - \int_0^t dt' \frac{\sin(M_0(t-t'))}{M_0} \epsilon U(t'), \quad (5.37)$$

where

$$U_0^{(R)}(t) = \cos(M_0 t) - \frac{i}{\hbar} \frac{\sin(M_0 t)}{M_0} H_I \quad (5.38)$$

differs from Eq. (5.29) by the inclusion of the δ dependent terms in M_0 and H_I .

One way of verifying that Eq. (5.37) is correct, is by checking that both sides have the same Laplace transform. Indeed, they do:

$$\frac{1}{s + iH_I/\hbar} = \frac{s}{s^2 + M_0^2} - \frac{i}{\hbar} \frac{1}{s^2 + M_0^2} H_I - \frac{1}{s^2 + M_0^2} \epsilon \frac{1}{s + iH_I/\hbar} \quad (5.39)$$

is an identity that follows from Eq. (5.24).

As mentioned at the end of Section 5.3.1, the multiplication order of H_I and even powers of M^2 is irrelevant in Eq. (5.27) as they commute. In Eq. (5.38), however, the order does matter as $[H_I, M_0^2] \neq 0$ when $\delta \neq 0$. In addition to Eq. (5.37) with Eq. (5.38) where H_I is on the right, we have, therefore, also an “on the left” version,

$$U(t) = U_0^{(L)}(t) - \int_0^t dt' U(t-t') \epsilon \frac{\sin(M_0 t')}{M_0} \quad (5.40)$$

with

$$U_0^{(L)}(t) = \cos(M_0 t) - \frac{i}{\hbar} H_I \frac{\sin(M_0 t)}{M_0}. \quad (5.41)$$

Half their sum gives a symmetrized version,

$$U(t) = U_0^{(S)}(t) - \frac{1}{2} \int_0^t dt' \frac{\sin(M_0(t-t'))}{M_0} \epsilon U(t') - \frac{1}{2} \int_0^t dt' U(t-t') \epsilon \frac{\sin(M_0 t')}{M_0} \quad (5.42)$$

with

$$U_0^{(S)}(t) = \cos(M_0 t) - \frac{i}{2\hbar} \frac{\sin(M_0 t)}{M_0} H_I - \frac{i}{2\hbar} H_I \frac{\sin(M_0 t)}{M_0}, \quad (5.43)$$

and there are many more variants that one could explore.

Each of the integral equations Eq. (5.37), Eq. (5.40), and Eq. (5.42) provides a hierarchy of approximations by an iteration that commences with the respective

zeroth approximation. This is, of course, the procedure by which one generates the Born series from the Lippmann-Schwinger equation. For the “on the right” equation Eq. (5.37), the k th-order approximation is

$$U_k^{(R)}(t) = U_{k-1}^{(R)}(t) - \int_0^t dt' \frac{\sin(M_0(t-t'))}{M_0} \epsilon U_{k-1}^{(R)}(t'), \quad (5.44)$$

and analogous expressions apply to the “on the left” version and the symmetrized variant. Note that $U_k^{(S)}(t)$ is not half the sum of $U_k^{(R)}(t)$ and $U_k^{(L)}(t)$ for $k \neq 0$; that arithmetic mean could also be taken as a valid k th-order approximation. For such a scheme to be useful in practice, the zeroth-order approximation should be quite good to begin with, the first-order approximation should be sufficient for many purposes, and it should not be necessary to go beyond the second order.

The various k th-order approximations differ from each other, but they are all accurate up to k th-order in $|\epsilon/M_0^2| \sim |\delta\Omega|/\Delta^2$. In the common case where $|\Omega/\Delta| \sim 10^{-1}$ and $|\delta/\Delta| \sim 10^{-2}$, we have $|\epsilon/M_0^2| \sim 10^{-3}$. Remember that the δ dependence in H_I and the ϵ dependence (which also depends on δ) are treated separately. Although ϵ goes to zero when δ vanishes, $|\epsilon/M_0^2|$ is one order of magnitude smaller than δ/Δ .

A technical point is the following. The approximate evolution matrices $U_k(t)$ are not unitary, rather $U_k(t)^\dagger U_k(t)$ deviates from the unit matrix by an amount of order ϵ^{k+1} . One can cope with this in various ways; see Appendix B. Perhaps the simplest is to ensure proper normalization by including a time-dependent factor that depends on the initial set of probability amplitudes, thereby arriving at an effective unitary matrix $\tilde{U}_k(t)$ that is suitable for the given initial column $\Psi_I(0)$,

$$\tilde{U}_k(t)\Psi_I(0) = \frac{U_k(t)\Psi_I(0)}{\sqrt{\Psi_I(0)^\dagger U_k(t)^\dagger U_k(t)\Psi_I(0)}}. \quad (5.45)$$

In other words, we apply $U_k(t)$ to $\Psi_I(0)$ and normalize the resulting column to unit length. This procedure worked fine for all examples that we studied.

As remarked above, the k th-order approximations $U_k^{(R)}(t)$, $U_k^{(L)}(t)$, and $U_k^{(S)}(t)$

differ slightly and might not describe the system equally well. We discuss a few examples of the state populations as functions of time under different approximations, and analyze the performance of these approximations. We compare the results to the exact numerical answers. The value $\Delta = 400$ MHz is taken for the average detuning, as it is of typical order for real experiments, and the values of the Rabi coupling strengths Ω_0 and Ω_1 can vary in a range of fractions of Δ . The overall detuning δ of the two-photon transition can be controlled to within 1 MHz accuracy in laboratory experiments. For the purpose of this analysis, then, we take the liberty of setting δ to any value we like.

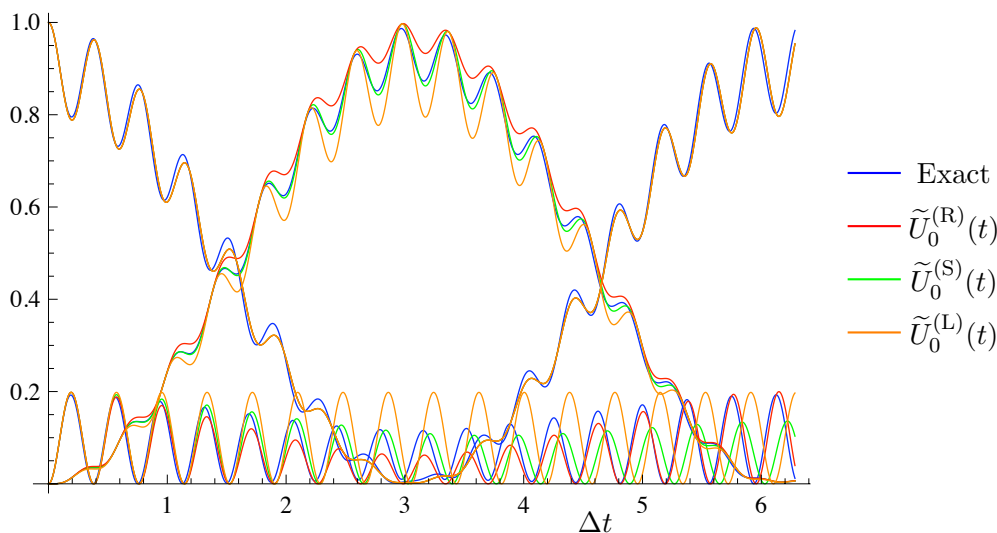


Figure 5.4: Plots of populations obtained from different zeroth-order solutions of the Lippmann-Schwinger equations. Blue curves give the exact results from numerical simulation using the Hamiltonian H_I ; green curves show solutions from the symmetric approximation $\tilde{U}_0^{(S)}(t)$; red curves show solutions from $\tilde{U}_0^{(R)}(t)$; and orange curves show solutions from $\tilde{U}_0^{(L)}(t)$. The parameters are $\Delta = 400$ MHz, $|\Omega_0| = \Delta/2$, $|\Omega_1| = 3\Delta/10$ and $\delta = -\Omega^\dagger \sigma_3 \Omega / (4\Delta) = (|\Omega_1|^2 - |\Omega_0|^2) / (4\Delta) = -16$ MHz. The effective Rabi frequency is $\Omega_R = 27.8$ MHz, about 7% of Δ . Initially, we have $c_0(0) = 1$ and $c_1(0) = c_e(0) = 0$. The curves starting at 1 show the approximations for $|c_0(t)|^2$; the curves that start at 0 and rise to 1 are for $|c_1(t)|^2$; and the curves that start at 0 and never exceed small values are for $|c_e(t)|^2$.

Figure 5.4 gives an example that demonstrates the quality of the zeroth-order approximations given by $\tilde{U}_0^{(R)}(t)$, $\tilde{U}_0^{(L)}(t)$, and $\tilde{U}_0^{(S)}(t)$. Since $U_0^{(S)}(t)$ is an average of $U_0^{(R)}$ and $U_0^{(L)}(t)$, we expect the population curves for $\tilde{U}_0^{(S)}(t)$ to lie between the other two curves and this can be seen quite clearly in Fig. 5.4. Moreover, the solutions of the population in the initial state $|0\rangle$ do not depend much on which of the three zeroth-order approximations is used, and all of them are very close to

the exact numerical solution. In this example, we use $\delta = (|\Omega_1|^2 - |\Omega_0|^2)/(4\Delta)$, the value of Eq. (5.17), which gives an effective resonant two-photon transition, and we can see that full population transfer from $|0\rangle$ to $|1\rangle$ can be achieved. In comparison, full population transfer cannot be achieved for other values of δ .

In Fig. 5.4, the value of $|\delta|$ is about a few percent of $|\Delta|$. The plot shows that, in this parameter regime, $\tilde{U}_0^{(S)}(t)$ approximates the evolution of the probabilities for finding $|0\rangle$ and $|1\rangle$ quite well, and it certainly works best among the three different zeroth-order approximations shown here. The approximation for the excited state population also works well when t is short, i.e. during the first few fast oscillation periods, but the deviation grows quickly with time.

The accuracy is better for higher-order approximations. We compare the approximations of zeroth, first, and second order for the three different Lippmann-Schwinger equations in Figs. 5.5(a), 5.5(b), and 5.6. Figure 5.5(a) shows that the deviation of the zeroth-order approximation $\tilde{U}_0^{(R)}(t)$ from the exact numerical solution is large when about half of the effective Rabi cycle is completed, i.e., around $t = \pi/\Omega_R$ or $\Delta t \simeq 45$, and the deviation is smaller around a full Rabi cycle. The main deviation is in the size of the small-amplitude oscillations with short period, whereas the Rabi oscillation with longer period is reproduced equally well by $\tilde{U}_k^{(R)}(t)$ with $k = 0, 1, 2$. The first-order approximation corrects part of the error in the zeroth-order approximation, and the second-order approximation improves matters further and gets the probabilities very close to their exact values. The same observations can be made about the corresponding “on the left” approximations in Fig. 5.5(b). How about the symmetric version $\tilde{U}_k^{(S)}(t)$ whose zeroth-order approximation already works quite well?

Figure 5.6 shows that when the two-photon transition is resonant, the difference between $\tilde{U}_0^{(S)}(t)$, $\tilde{U}_1^{(S)}(t)$, and $\tilde{U}_2^{(S)}(t)$ is difficult to detect. All three lowest-order approximations of Eq. (5.42) describe the evolution of the system well during the first Rabi cycle. The zeroth-order approximation works surprisingly well, at times it gives a better result than the higher-order approximations (see the bottom plot of the two blow-ups). The improvement offered by the higher-order approximations

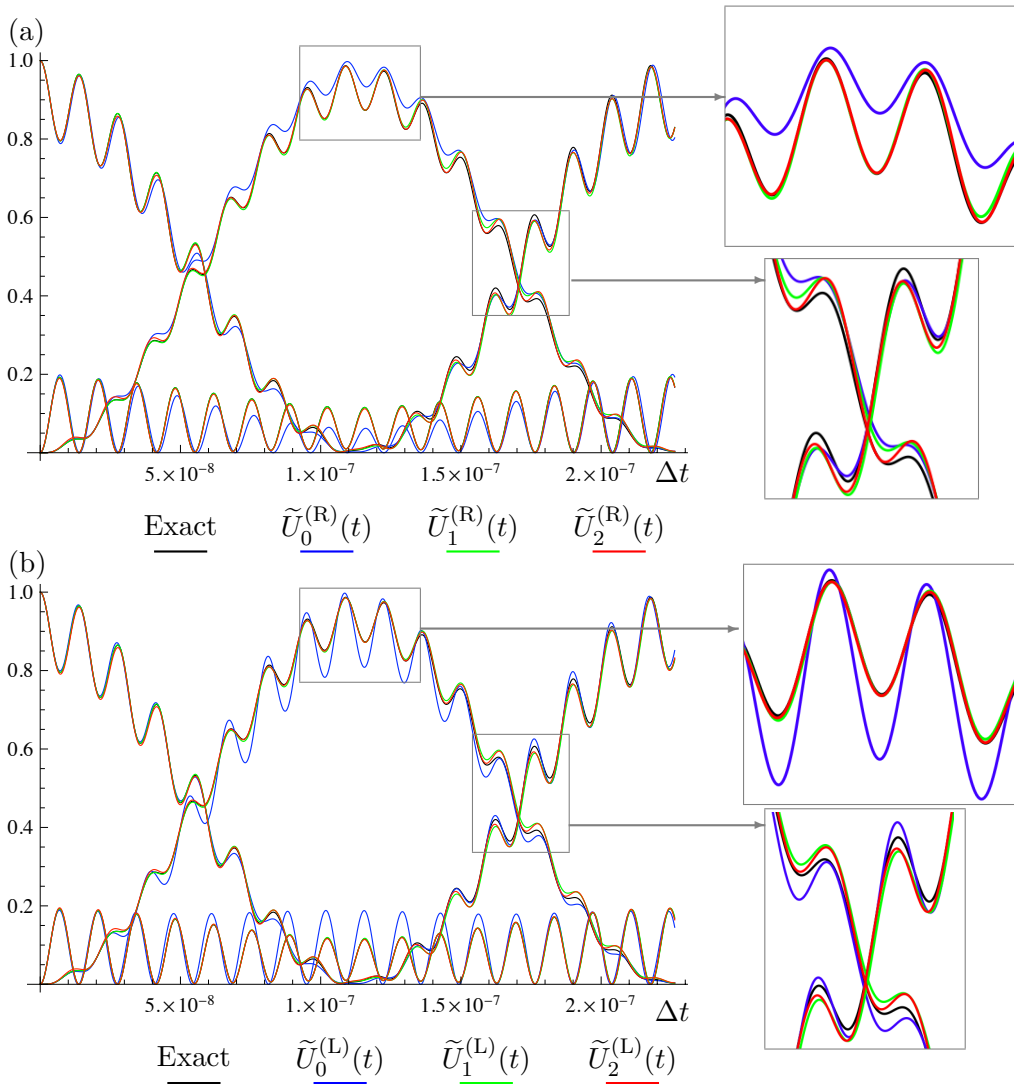


Figure 5.5: Comparison of the probabilities obtained from the zeroth-, first-, and second-order approximations of the Lippmann-Schwinger equations Eq. (5.37) and Eq. (5.40). In plot (a), the blue, green, and red curves show solutions from $\tilde{U}_0^{(R)}(t)$, $\tilde{U}_1^{(R)}(t)$, and $\tilde{U}_2^{(R)}(t)$, respectively; and in plot (b), the blue, green, and red curves show solutions from from $\tilde{U}_0^{(L)}(t)$, $\tilde{U}_1^{(L)}(t)$, and $\tilde{U}_2^{(L)}(t)$, respectively. The parameters and the initial state are the same as in Fig. 5.4.

can be observed near the middle of the Rabi cycle (see the top plot of the blow-ups), and this improvement is more substantial when ϵ gets larger. For a practical application to experiments that aim at complete population transfer from $|0\rangle$ to $|1\rangle$, the approximation provided by $\tilde{U}_0^{(S)}(t)$ is accurate enough to determine the parameter values reliably.

5.3.4 Discussion

To summarize our approach, we split $(H_I/\hbar)^2$, the square of the interaction Hamiltonian, into two parts: the dominant part M_0^2 and a small correction ϵ . With this

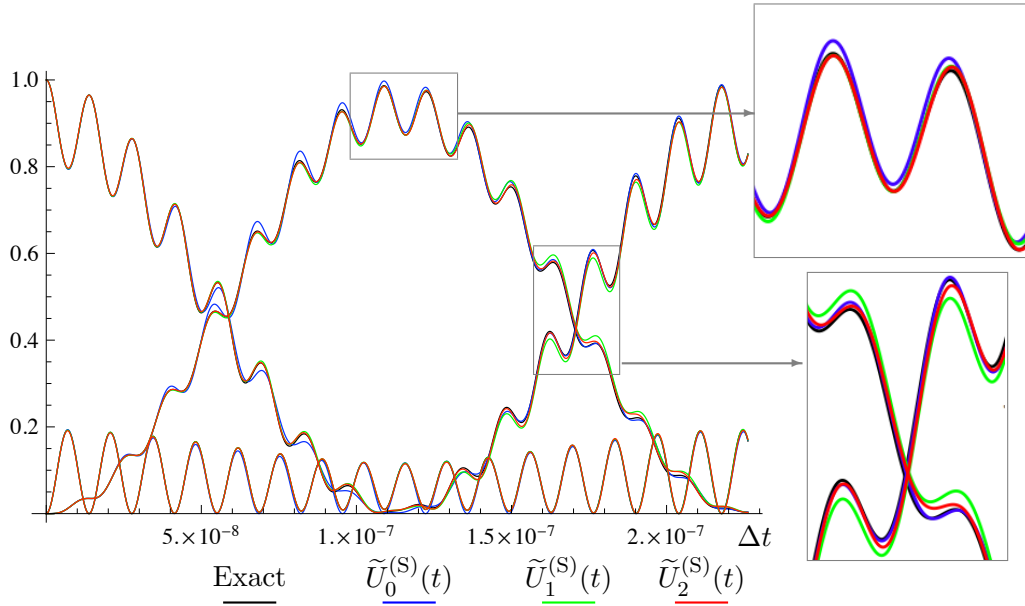


Figure 5.6: Comparison of the zeroth-, first-, and second-order approximations of the symmetric Lippmann-Schwinger Eq. (5.42). The parameter values, the initial state, and the color coding are the same as in Fig. 5.5.

splitting and any one of the Lippmann-Schwinger equations Eq. (5.37), Eq. (5.40), or Eq. (5.42), successive approximations to the unitary evolution matrix $U(t) = \exp(-iH_I t/\hbar)$ can be obtained iteratively. If we use the approximations given by $\tilde{U}_k^{(R)}(t)$ and $\tilde{U}_k^{(L)}(t)$, we only need to do one iteration and stop at the first-order solution ($k = 1$) for a very good approximation. If we use the symmetric version $\tilde{U}_k^{(S)}(t)$, we do not even need to go beyond the zeroth-order approximation since $\tilde{U}_0^{(S)}(t)$ is already very close to the exact evolution for typical experimental parameters. Thus, we have

$$U(t) \simeq U_0^{(S)}(t) = \cos(M_0 t) - \frac{i}{2\hbar} \frac{\sin(M_0 t)}{M_0} H_I - \frac{i}{2\hbar} H_I \frac{\sin(M_0 t)}{M_0} \rightarrow \tilde{U}_0^{(S)}(t), \quad (5.46)$$

where $\tilde{U}_0^{(S)}(t)$ differs from $U_0^{(S)}(t)$ by the time-dependent factor of Eq. (5.45) that ensures $\Psi_I(t) = \tilde{U}_0^{(S)}(t)\Psi_I(0)$ is properly normalized for the given initial column of probability amplitudes.

According to Eq. (5.46), the oscillation of the state populations of $|0\rangle$ and $|1\rangle$ are governed by the operator M_0^2 . The effective Rabi oscillation frequency, to a very good approximation, only depends on the eigenvalues μ_{\pm}^2 of the first diagonal

Chapter 5. Raman-type Transitions

block of M_0^2 . Applying the same argument as in Section 5.3.2 for the case of $\delta = -\Omega^\dagger \sigma_3 \Omega / 4\Delta$ in Eq. (5.17), the effective Rabi frequency is (we take $\mu_\pm > 0$)

$$\Omega_R = \mu_+ - \mu_- = \frac{1}{2} \sqrt{(\Delta^2 + \delta^2) + \frac{1}{2}(|\Omega_0| + |\Omega_1|)^2} - \frac{1}{2} \sqrt{(\Delta^2 + \delta^2) + \frac{1}{2}(|\Omega_0| - |\Omega_1|)^2}, \quad (5.47)$$

With this particular choice of δ , the Rabi oscillation amplitude could reach unity; however, this might not be the real maximum that the population in state $|1\rangle$ can reach, because on top of this slow effective Rabi oscillation, the population also oscillates with a fast frequency. This fast oscillation goes roughly with the frequency $\mu_- + \mu_+ \simeq |\Delta|$. Nevertheless, up to linear order in δ/Δ , we find that the oscillation amplitude goes to unity, regardless whether we choose δ in accordance with Eq. (5.17) or with Eq. (5.20). This shows why the evolution of the system is essentially the same for both δ values.

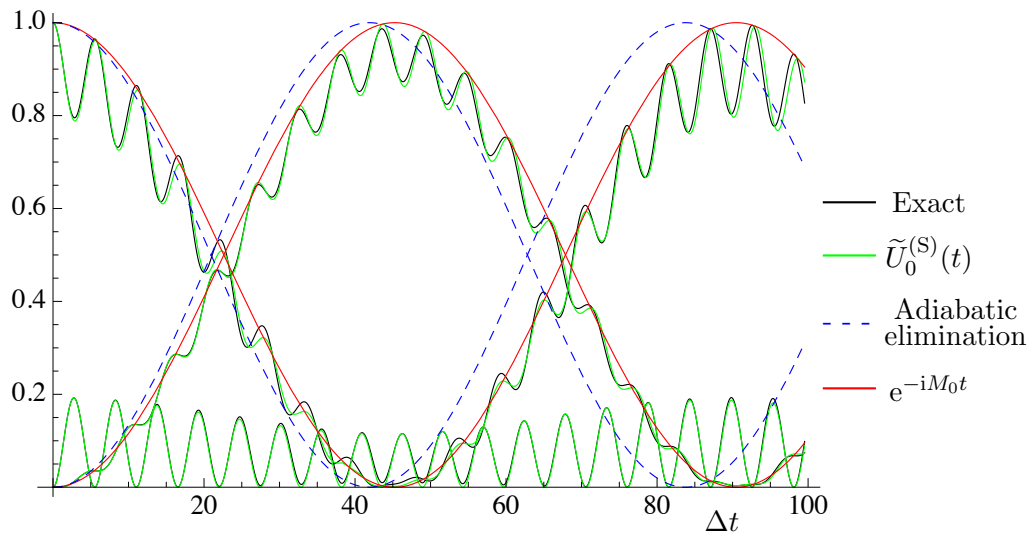


Figure 5.7: Improvement on the effective two-level Hamiltonian compared with adiabatic elimination. The black curves give the exact numerical solution; the green curves are for the symmetric zeroth-order approximation of $U(t)$; the blue dashed curves are for the adiabatic-elimination approximation; and the red curves result from taking M_0 as the effective Hamiltonian. The parameter values and the initial state are the same as in Figs. 5.4.

Moreover, since approximately the effective Rabi oscillation of the two relevant states depends on the eigensystem of M_0^2 only, the effective Hamiltonian between states $|0\rangle$ and $|1\rangle$ is approximately given by the 2×2 upper diagonal block of $\hbar M_0$,

5.4. Multi-atom collective Rydberg transitions

if we exclude the excited state $|e\rangle$ from the evolution directly. That is

$$H_{\text{eff}} = -\frac{\hbar}{2}\sqrt{(\Delta + \delta\sigma_3)^2 + \Omega\Omega^\dagger}. \quad (5.48)$$

The minus sign is chosen for the same reasoning as in Eq. (5.28). From this effective Hamiltonian, we can find the Rabi frequency directly and one of the special cases was already given in Eq. (5.47); the oscillation amplitude for an arbitrary δ is

$$P = 1 - \frac{(\Omega^\dagger\sigma_3\Omega + 4\delta\Delta)^2}{(\Omega^\dagger\Omega)^2 + 8\delta\Delta\Omega^\dagger\sigma_3\Omega + (4\delta\Delta)^2}, \quad (5.49)$$

and again we have $P = 1$ when $\delta = -\Omega^\dagger\sigma_3\Omega/4\Delta$. Figure 5.9 shows that this effective Hamiltonian is much more accurate than that of the adiabatic-elimination approximation, inasmuch as the evolution given by e^{-iM_0t} gives a very close envelope of the population oscillation.

Therefore, if one is only interested in having an effective two-level description for the relevant states $|0\rangle$ and $|1\rangle$, the effective Hamiltonian can be obtained with Eq. (5.48) directly without going through adiabatic elimination. Moreover, the effective Hamiltonian obtained this way describe the evolution of the state and the Rabi oscillation much more accurately than the adiabatic elimination method. For more accurate solutions including the intermediate state, Eq. (5.46) can be used.

5.4 Multi-atom collective Rydberg transitions

As we mentioned in Sec. 4.1, an atomic transition to a highly excited Rydberg level is normally performed by a two-photon Raman process, due to the large energy difference between the ground state and the Rydberg state. For Rydberg states with strong Rydberg blockade, when more atoms are simultaneously involved in the transition within the blockade range, only a collective single excitation can be achieved and the multi-Rydberg excitations are non-resonant owing to the strong dipole-dipole interaction between the Rydberg levels.

The single-atom Rydberg transition is a three-level Raman process, for which

one can solve for the light shift δ and the effective Rabi frequency Ω_R . The multi-atom Rydberg excitation is often treated as an effective three-level problem analogously with, namely, the ground state, the single collective intermediate excited state and the single collective Rydberg state. As we know from standard quantum optics, when N identical particles are involved in the transition simultaneously, the Rabi frequency is enhanced by a \sqrt{N} factor (Dicke's superradiance [99] are a familiar example). Thus, for the reduced three-level Raman transition from the ground state to the collective single excited Rydberg state, one expects that the N -atom effective Rabi frequency is

$$\Omega_{R,N} = \sqrt{N}\Omega_R. \quad (5.50)$$

The light shifts are usually taken to be the same as for the single atom.

The simple expression in Eq. (5.50) is often used as an approximate solution for experimental works, and the exact solution is difficult to compute analytically since the dimension of the total Hilbert space grows exponentially with the number of atoms. Here, we develop a scheme of solving such a many-atom Rydberg excitation more rigorously following a methodology similar to that presented in the last two subsections of this chapter, and hence, provide a more accurate answer for the effective Rabi frequency. Rydberg excitation for a system of two atoms is discussed in detail here.

5.4.1 Two-atom collective Rydberg excitation

For each atom, we label the ground state, the intermediate excited state and the Rydberg state with $|g\rangle$, $|e\rangle$ and $|r\rangle$, respectively. Again, we take as the basic physical model that each atom can be treated as a three-level system and forget all the other levels that are not initially populated and not coupled efficiently to the relevant levels. The Rydberg transition is a Raman transition of the cascade-type, where the excited state $|e\rangle$ couples the other two states $|g\rangle$ and $|r\rangle$ non-resonantly with coupling strengths Ω_0 and Ω_1 ; see Fig. 5.8. The two transitions are driven by two

5.4. Multi-atom collective Rydberg transitions

lasers with frequencies ω_{L0} and ω_{L1} , and the atom-light interaction Hamiltonian for the system is

$$H_{AL} = -\frac{\hbar}{2} \sum_{j=1,2} (|g\rangle\langle e|)_j \Omega_0 e^{i\omega_{L0}t} - \frac{\hbar}{2} \sum_{j=1,2} (|e\rangle\langle r|)_j \Omega_1 e^{i\omega_{L1}t} + \text{h.c.}, \quad (5.51)$$

where j labels the identical atoms and the Rabi frequencies are

$$\Omega_0 = \frac{q_{\text{el}}}{\hbar} \langle g | \mathbf{r} \cdot \mathbf{E}_{L0} | e \rangle \quad \text{and} \quad \Omega_1 = \frac{q_{\text{el}}}{\hbar} \langle e | \mathbf{r} \cdot \mathbf{E}_{L1} | r \rangle. \quad (5.52)$$

With a symmetric coupling between the identical atoms, the system remains in a symmetric state if the initial state is symmetric. The total dimensionality of the two-atom system is $3^2 = 9$, but the dimensionality is reduced to six because we restrict the treatment to only considering the symmetric states. The total Hamiltonian of the system is

$$H = H_{\text{Atom}} + H_{\text{dd}} + H_{AL}, \quad (5.53)$$

where H_{dd} is the dipole-dipole interaction between the two atoms, which causes the energy of the selected doubly excited Rydberg state to be shifted. H_{dd} affects the two-atom energy levels, but it does not have an effect on the interaction Hamiltonian between light and atoms directly. Since H_{dd} is small compared with the free energy H_{Atom} , we can treat the dipole-dipole interaction as a perturbation to H_{Atom} and so arrive at

$$\tilde{H}_{\text{Atom}} = \sum_{j=1}^6 |v_j\rangle E_j \langle v_j|, \quad (5.54)$$

where

$$\begin{aligned}
 |v_1\rangle &= |gg\rangle, & E_1 &= 0; \\
 |v_2\rangle &= (|rg\rangle + |gr\rangle)/\sqrt{2}, & E_2 &= \hbar\omega_r; \\
 |v_3\rangle &= (|eg\rangle + |ge\rangle)/\sqrt{2}, & E_3 &= \hbar\omega_e; \\
 |v_4\rangle &= (|re\rangle + |er\rangle)/\sqrt{2}, & E_4 &= \hbar(\omega_e + \omega_r); \\
 |v_5\rangle &= |ee\rangle, & E_5 &= 2\hbar\omega_e; \\
 |v_6\rangle &= |rr\rangle, & E_6 &= \hbar(2\omega_r + \omega_{dd}).
 \end{aligned} \tag{5.55}$$

The effect of the strong dipole-dipole interaction between Rydberg states is taken into account by adding the energy shift $\hbar\omega_{dd}$ to the energy of the doubly excited Rydberg state $|v_6\rangle$, and the perturbative effect of H_{dd} on the lower-lying atomic levels is weak and negligible. The atomic level diagram is shown in Fig. 5.8.

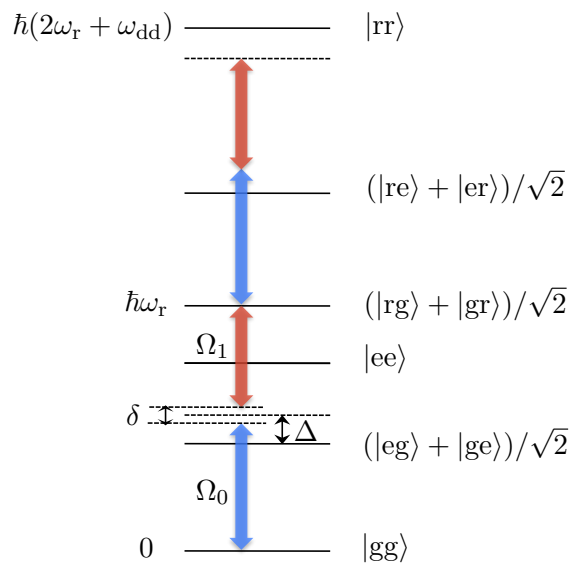


Figure 5.8: Level diagram of a two-atom Rydberg excitation. The transition between the ground state $|g\rangle$ and the excited state $|e\rangle$ is detuned by $-\Delta + \delta/2$; the transition between the excited state $|e\rangle$ and the Rydberg state $|r\rangle$ is detuned by $\Delta + \delta/2$. $\hbar\omega_{dd}$ is the energy shift arising from the Rydberg blockade mechanism.

According to Fig. 5.8, the two-photon transition is detuned by $\delta = \omega_r - \omega_{L0} - \omega_{L1}$, and, in general, we have $|\delta| \ll |\Delta|$ in practical situations. The total Hamiltonian

5.4. Multi-atom collective Rydberg transitions

in the basis of $\{|v_j\rangle\}$ can be represented by the 6×6 matrix

$$H \cong \frac{\hbar}{2} \begin{pmatrix} 0 & 0 & \sqrt{2}\Omega_0 e^{i\omega_{L0}t} & 0 & 0 & 0 \\ 0 & 2\omega_r & \Omega_1^* e^{-i\omega_{L1}t} & \Omega_0 e^{i\omega_{L0}t} & 0 & 0 \\ \sqrt{2}\Omega_0^* e^{-i\omega_{L0}t} & \Omega_1 e^{i\omega_{L1}t} & 2\omega_e & 0 & \sqrt{2}\Omega_0 e^{i\omega_{L0}t} & 0 \\ 0 & \Omega_0^* e^{-i\omega_{L0}t} & 0 & 2(\omega_e + \omega_r) & \sqrt{2}\Omega_1^* e^{-i\omega_{L1}t} & \sqrt{2}\Omega_1 e^{i\omega_{L1}t} \\ 0 & 0 & \sqrt{2}\Omega_0^* e^{-i\omega_{L0}t} & \sqrt{2}\Omega_1 e^{i\omega_{L1}t} & 4\omega_e & 0 \\ 0 & 0 & 0 & \sqrt{2}\Omega_1^* e^{-i\omega_{L1}t} & 0 & (4\omega_r + 2\omega_{dd}) \end{pmatrix}. \quad (5.56)$$

We get rid of this periodic time dependence by going to the rotating frame of $H_0 = \tilde{H}_{\text{Atom}} + D$, where

$$D \cong \frac{\hbar}{2} \begin{pmatrix} \delta & 0 & 0 & 0 & 0 & 0 \\ 0 & -\delta & 0 & 0 & 0 & 0 \\ 0 & 0 & 2\Delta & 0 & 0 & 0 \\ 0 & 0 & 0 & 2\Delta - 2\delta & 0 & 0 \\ 0 & 0 & 0 & 0 & 4\Delta - \delta & 0 \\ 0 & 0 & 0 & 0 & 0 & -3\delta - 2\omega_{dd} \end{pmatrix}. \quad (5.57)$$

The Hamiltonian in this particular interaction picture is time independent,

$$H_I = e^{iH_0 t/\hbar} (H_{\text{AL}} - D) e^{-iH_0 t/\hbar} \\ \cong \frac{\hbar}{2} \begin{pmatrix} -\delta & 0 & \sqrt{2}\Omega_0 & 0 & 0 & 0 \\ 0 & \delta & \Omega_1^* & \Omega_0 & 0 & 0 \\ \sqrt{2}\Omega_0^* & \Omega_1 & -2\Delta & 0 & \sqrt{2}\Omega_0 & 0 \\ 0 & \Omega_0^* & 0 & -2\Delta + 2\delta & \sqrt{2}\Omega_1^* & \sqrt{2}\Omega_1 \\ 0 & 0 & \sqrt{2}\Omega_0^* & \sqrt{2}\Omega_1 & -4\Delta + \delta & 0 \\ 0 & 0 & 0 & \sqrt{2}\Omega_1^* & 0 & 3\delta + 2\omega_{dd} \end{pmatrix}. \quad (5.58)$$

In the interaction picture, the diagonal entries no longer give the true energies of the atomic levels. Rather, the difference between two diagonal entries yields the detuning of the respective coupling. For example, the states $|v_1\rangle$ and $|v_2\rangle$ are

Chapter 5. Raman-type Transitions

coupled to state $|v_3\rangle$ with detuning $-\Delta + \delta/2$ and $\Delta + \delta/2$; state $|v_5\rangle$ is coupled to states $|v_3\rangle$ and $|v_4\rangle$ with detuning $-\Delta + \delta/2$ and $\Delta + \delta/2$; and state $|v_6\rangle$ is coupled to state $|v_4\rangle$ with detuning $\omega_{\text{dd}} + \Delta + \delta/2$. When the atomic frequency shift ω_{dd} due to the Rydberg blockade is large (a few times of Δ in magnitude), the detuning of state $|v_6\rangle$ becomes so large that it gets nearly decoupled from the rest of the system. State $|v_5\rangle$ is coupled to two other states with only a detuning of roughly Δ in magnitude; however, it does not directly couple to states $|v_1\rangle$ and $|v_2\rangle$. The coupling of $|v_5\rangle$ to $|v_1\rangle$ or $|v_2\rangle$ is not only of higher-order in $|\Omega/\Delta|$ but also detuned by roughly -2Δ . Therefore, if we start with the population in the subspace spanned by $|v_1\rangle$ and $|v_2\rangle$, the chance that states $|v_5\rangle$ and $|v_6\rangle$ will get populated is very low.

If we discard these two states completely from the system, we get a reduced four-level problem with the effective interaction-picture Hamiltonian

$$H_{\text{R}} \hat{=} \frac{\hbar}{2} \begin{pmatrix} -\delta & 0 & \sqrt{2}\Omega_0 & 0 \\ 0 & \delta & \Omega_1^* & \Omega_0 \\ \sqrt{2}\Omega_0^* & \Omega_1 & -2\Delta & 0 \\ 0 & \Omega_0^* & 0 & -2\Delta + 2\delta \end{pmatrix} \quad (5.59)$$

by deleting the last two rows and columns associated with states $|v_5\rangle$ and $|v_6\rangle$. This four-level Hamiltonian does not carry any information about the presence of the two deleted states.

Alternatively, instead of ignoring the last two states from the system completely, we can employ the concept of adiabatic elimination for these two states by setting $\frac{\partial}{\partial t}c_5(t) = 0$ and $\frac{\partial}{\partial t}c_6(t) = 0$. However, this adiabatic elimination has to be done in the appropriate interaction picture, for the same reason we argued in Sec. 5.2.3 for a three-level system. Using the simplest criteria in [94], the appropriate interaction pictures is chosen when the trace of the relevant or uneliminated sector of the Hamiltonian in the interaction picture vanishes, i.e., $H_{\text{I}} \rightarrow H_{\text{I}} + \Delta - \delta/2$. This

5.4. Multi-atom collective Rydberg transitions

yields

$$\begin{aligned} \sqrt{2}\Omega_0^*c_3 + \sqrt{2}\Omega_1c_4 + (-3\Delta + \delta/2)c_5 &= 0 \\ \text{and } \sqrt{2}\Omega_1^*c_4 + (2\omega_{\text{dd}} + \Delta + 5\delta/2)c_6 &= 0; \end{aligned} \quad (5.60)$$

thus, the last two states can be eliminated using

$$\begin{aligned} c_5 &= \frac{\sqrt{2}}{3\Delta - \delta/2}(\Omega_0^*c_3 + \Omega_1c_4) \\ \text{and } c_6 &= -\frac{\sqrt{2}\Omega_1^*}{2\omega_{\text{dd}} + \Delta + 5\delta/2}c_4. \end{aligned} \quad (5.61)$$

Hereby, the reduced four-level Hamiltonian is

$$H_{\text{R}} \hat{=} \frac{\hbar}{2} \begin{pmatrix} -\delta & 0 & \sqrt{2}\Omega_0 & 0 \\ 0 & \delta & \Omega_1^* & \Omega_0 \\ \sqrt{2}\Omega_0^* & \Omega_1 & -2\Delta + \frac{2|\Omega_0|^2}{3\Delta - \delta/2} & \frac{2\Omega_0\Omega_1}{3\Delta - \delta/2} \\ 0 & \Omega_0^* & \frac{2\Omega_0^*\Omega_1^*}{3\Delta - \delta/2} & -2\Delta + 2\delta + \frac{2|\Omega_1|^2}{3\Delta - \delta/2} - \frac{2|\Omega_1|^2}{2\omega_{\text{dd}} + \Delta + 5\delta/2} \end{pmatrix}. \quad (5.62)$$

Now, we try to apply what we learnt from the single-atom Raman transition to this effective four-level problem. First, since shifting all the diagonal elements by the same amount does not change the physics, the Hamiltonian in a different interaction picture,

$$\tilde{H}_{\text{R}} \hat{=} H_{\text{R}} + \frac{\hbar\beta}{2} = \frac{\hbar}{2} \begin{pmatrix} A & \Omega \\ \Omega^\dagger & A' \end{pmatrix}, \quad (5.63)$$

describes the system equally well as H_{R} , where

$$A = \begin{pmatrix} \beta - \delta & 0 \\ 0 & \beta + \delta \end{pmatrix}, \quad \Omega = \begin{pmatrix} \sqrt{2}\Omega_0 & 0 \\ \Omega_1^* & \Omega_0 \end{pmatrix} \quad (5.64)$$

and

$$A' = \begin{pmatrix} \beta - 2\Delta + \frac{2|\Omega_0|^2}{3\Delta - \delta/2} & \frac{2\Omega_0\Omega_1}{3\Delta - \delta/2} \\ \frac{2\Omega_0^*\Omega_1^*}{3\Delta - \delta/2} & \beta - 2\Delta + 2\delta + \frac{2|\Omega_1|^2}{3\Delta - \delta/2} - \frac{2|\Omega_1|^2}{2\omega_{\text{dd}} + \Delta + 5\delta/2} \end{pmatrix}. \quad (5.65)$$

The square of the reduced four-level Hamiltonian is given by

$$\frac{\tilde{H}_R^2}{\hbar^2} \doteq \underbrace{\frac{1}{4} \begin{pmatrix} A^2 + \Omega\Omega^\dagger & 0 \\ 0 & A'^2 + \Omega'^\dagger\Omega' \end{pmatrix}}_{M_0^2} + \underbrace{\frac{1}{4} \begin{pmatrix} 0 & -\Omega A' - A\Omega \\ -A'\Omega'^\dagger - \Omega'^\dagger A & 0 \end{pmatrix}}_{\epsilon}, \quad (5.66)$$

where M_0^2 contains the two 2×2 diagonal blocks and ϵ contains the off-diagonal blocks that are small compared with M_0^2 . The structure of Eq. (5.66) is similar to that of Eq. (5.24) in Sec. 5.3. Analogously, we can get the zeroth-order solution using the evolution operator given by the Lippmann-Schwinger equation, i.e.,

$$U_0^{(S)}(t) = \cos(M_0 t) - \frac{i}{2\hbar} \frac{\sin(M_0 t)}{M_0} \tilde{H}_R - \frac{i}{2\hbar} \tilde{H}_R \frac{\sin(M_0 t)}{M_0}. \quad (5.67)$$

We have one additional parameter β to fix. In the successive solutions given by the Lippmann-Schwinger equation, the error goes with the orders of ϵ , ϵ^2 , \dots ; thus, the smaller the size of ϵ , the better the approximation. For an optimal choice of β , we minimize

$$\text{tr} \left\{ \epsilon^\dagger \epsilon \right\} = 2 \text{tr} \left\{ (\Omega A' + A\Omega)(A'\Omega'^\dagger + \Omega'^\dagger A) \right\}. \quad (5.68)$$

This gives a quadratic equation for β , and the minimum is reached when

$$\beta = \Delta_3 - \frac{1}{6|\Omega_0|^2 + 2|\Omega_1|^2} \left[\delta(|\Omega_0|^2 - |\Omega_1|^2) + \frac{4|\Omega_0|^2|\Omega_1|^2}{3\Delta - \delta/2} + 2|\Omega_0|^2(\Delta_4 - \Delta_3) \right], \quad (5.69)$$

where

$$\Delta_3 = \Delta - \frac{|\Omega_0|^2}{3\Delta - \delta/2} \quad \text{and} \quad \Delta_4 = \Delta - \delta - \frac{|\Omega_1|^2}{3\Delta - \delta/2} + \frac{|\Omega_1|^2}{2\omega_{\text{dd}} + \Delta + 5\delta/2}. \quad (5.70)$$

5.4. Multi-atom collective Rydberg transitions

The oscillation frequency is given by the difference of the eigenvalues of the first 2×2 diagonal block of matrix M_0 . The effective two-level Hamiltonian for the two states $|v_1\rangle = |gg\rangle$ and $|v_2\rangle = (|rg\rangle + |gr\rangle)/\sqrt{2}$ is

$$H_{\text{eff}} = -\frac{\hbar}{2} \sqrt{A^2 + \Omega\Omega^\dagger} = -\frac{\hbar}{2} \begin{pmatrix} (\beta - \delta)^2 + 2|\Omega_0|^2 & \sqrt{2}\Omega_0\Omega_1 \\ \sqrt{2}\Omega_0^*\Omega_1^* & (\beta + \delta)^2 + |\Omega_0|^2 + |\Omega_1|^2 \end{pmatrix}^{1/2}. \quad (5.71)$$

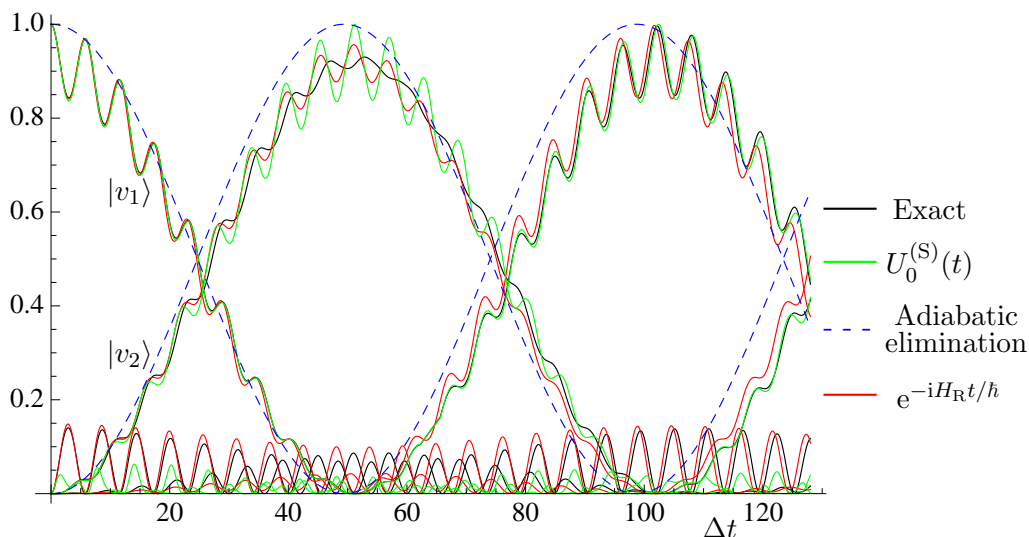


Figure 5.9: Population distribution for a collective single Rydberg excitation of two atoms with Rydberg blockade. The black curves give the exact numerical solution; the green curves are for the symmetric zeroth-order approximation of $U(t)$; the blue dashed curves are for the adiabatic-elimination approximation; and the red curves give the result from using the effective Hamiltonian H_R in Eq. (5.63). The detuning is $\Delta = 400\text{MHz}$, $\omega_{\text{dd}} = 2\text{GHz}$, $\delta = 0$ and coupling strengths $|\Omega_0| = |\Omega_1| = 3\Delta/10$. Initially, we have all the population in the ground state $|v_1\rangle$. The curves that start at 0 show the results for population in state $|v_1\rangle$; the curves that start at 0 and rise to approximately 1 show the population in state $|v_2\rangle$; and the curves that oscillate with small amplitudes are for the populations in state $|v_3\rangle$ and $|v_4\rangle$.

Figure 5.9 gives an example that demonstrates the quality of the approximation given by $U_0^{(S)}(t)$ and H_R given by Eqs. (5.67) and (5.63). First, it is clear that the approximations given by our method work much better than the conventional adiabatic elimination. Furthermore, for the population in the two relevant states $|v_1\rangle$ and $|v_2\rangle$, the results given by the evolution from the four-level effective Hamiltonian H_R and the results given by $U_0^{(S)}(t)$ are very close. This shows that the new method developed in this section works well not only for a three-level Raman transition but also for a four-level system like that described by H_R . However, by using $U_0^{(S)}(t)$, the computational complexity is much reduced since one only needs to diagonalize

two 2×2 matrices instead of a 4×4 matrix. Very often, the approximations to the population in state $|v_1\rangle$ is better than the approximations to the population in state $|v_2\rangle$; this is because the population in $|v_2\rangle$ is affected more by the population in state $|v_4\rangle$, which is not approximated well.

If one is only interested in the effective Rabi frequency for the collective Rydberg excitation, the difference in the eigenvalues of the first diagonal block of M_0 is a very good approximation; this is demonstrated by the green curves in Fig. 5.9. However, by eliminating states $|v_5\rangle$ and $|v_6\rangle$, the small-amplitude oscillation (or the “wiggles”) of the population in state $|v_1\rangle$ is no longer modeled well. To have a better approximation to the details in the small wiggles, one needs to seek a different way of eliminating states $|v_5\rangle$ and $|v_6\rangle$. This work is not presented in this thesis.

Here, it is worth emphasizing that, to reduce the six-level system to a four-level system, the choice of interaction picture in which one carries out the adiabatic elimination is essential. Elimination of state $|v_6\rangle$ has little effect as it is far-detuned by ω_{dd} , however, the choice of interaction picture for eliminating state $|v_5\rangle$ does affect the quality of the approximation. One should regard all the first four-levels ($\{|v_1\rangle, |v_2\rangle, |v_3\rangle, |v_4\rangle\}$) as the relevant states when applying the criteria in [94] for the right choice of interaction picture.

For future study, one can also extend this formalism to the more general problem of a N -atom collective single Rydberg excitation. When N is large, the \sqrt{N} enhancement in the Rabi frequency suggests that the same transition rate can be achieved with weaker laser powers. Thus, for very large N , one may be able to function in the regime where $|\Omega_0|, |\Omega_1| \ll |\Delta|$ such that results from the simple adiabatic elimination can be sufficiently reliable.

5.5 Summary

The conventional method of applying adiabatic elimination in solving multi-photon Raman transitions has its limitation and problems, as a result, it very often does

not give a good approximation. We presented an alternative approach to the quantitative description of the three-level Raman transition without applying adiabatic elimination and this new method gives a much more accurate solution while the computational complexity remains low. Integro-differential equations of Lippmann-Schwinger type provide a systematic way of generating successive approximations. A particular one with high symmetry performs so well that the lowest-order approximation is all one needs for a highly reliable determination of experimental parameters. With this method, one only needs to diagonalize a 2×2 matrix to obtain very accurate solutions of the entire system including the intermediate auxiliary state. This method also suggests a way for providing an effective two-level Hamiltonian for the two relevant states without adiabatic elimination. Moreover, this method can be used for higher-dimensional systems, such as multi-atom Rydberg excitation, which deserves further study.

Conclusion and outlook

A RFF qubit can be constructed from three or more identical particles. Three specific examples of three spin-1/2 particles, four spin-1/2 particles, and three spin-1 particles are provided in Chapter 2. These can be physically implemented with systems such as neutral atoms in an optical lattice or trapped ions. The RFF qubit stays perfectly coherent as long as the spins of the three atoms are affected by a magnetic-field-like noise in a homogenous manner. The inhomogeneous evolution of the atoms causes decoherence in the RFF qubit, but this decoherence can be suppressed efficiently by applying a bias magnetic field of modest strength perpendicular to the plane of the atoms in a 2D geometry.

The robustness of RFF qubits is studied in Chapter 3. The resulting lifetime of the RFF qubit can be many days, making RFF qubits of this kind promising candidates for quantum information storage units. Specifically, we examine the situation of three ${}^6\text{Li}$ atoms trapped in a CO_2 -laser-generated optical lattice and find that, even with conservatively estimated parameters for experimental imperfections, a stored qubit maintains a fidelity of 0.9999 for two hours. The RFF qubit made of three atoms in an equilateral geometry is proven to be more robust than the RFF qubit made of four atoms of the same kind in a 2D geometry. RFF qubits made from three ${}^{87}\text{Rb}$ atoms or three ${}^{40}\text{Ca}^+$ ions are also shown to be robust. Besides these, physical implementations of other kinds are also possible.

One way of preparing the RFF states with three atoms is studied in Chapter 4, which makes use of the Rydberg-blockade mechanism. The preparation scheme for RFF states constructed from trios of ${}^6\text{Li}$ atoms, ${}^{87}\text{Rb}$ atoms or ${}^{40}\text{Ca}^+$ ions is discussed explicitly, taking into account their specific energy-level structures. As

Chapter 6. Conclusion and outlook

an example, we show, with numerical simulations, that the robustness of the state preparation for a system of three ^{87}Rb atoms in an optical lattice can be very high. With modestly estimated experimental errors, the state preparation scheme is proven to be quite robust with a minimum fidelity of about 96%.

To use the RFF qubits for quantum storage, the retrieval of the stored information and quantum gate operations are also essential. In principle, one can follow the decoding procedure presented in [48] by doing a sequence of gates. However, it may not be possible to adapt that scheme exactly, as methods for gates implementation, for NMR qubits and atomic qubits can be very different. Further study on RFF-qubit gate operations is crucial for the quantum storage scheme to be implemented in practice.

The last part of this thesis is inspired by the use of two-photon Raman transitions for Rydberg excitations in the RFF state-preparation scheme. After reviewing the standard adiabatic-elimination approximation, which reduces the theoretical description of a three-level Raman transition to an effective two-level problem, and identifying some of the shortcomings of this approach, we introduce an alternative approximation method. Similar to adiabatic elimination, there is an essential two-level component in the new method without, however, eliminating the third auxiliary level. This makes the new method easy to use, inasmuch as one only needs to diagonalize a 2×2 matrix. Integro-differential equations of Lippmann-Schwinger type are the powerful tools that enable one to generate successive approximations. A particular hierarchy of approximations with high symmetry performs so well that the lowest-order approximation is all one needs for a highly reliable determination of experimental parameters. This method can also be applied to systems of higher dimensions, and the example of the two-atom Rydberg excitation with Rydberg blockade is presented briefly. The extension of the new method to higher-dimensional systems requires further study.

Appendices

Reduced dipole matrix element

The electric-dipole interaction between a one-electron atom and an electromagnetic field depends both on the strength and the polarization of the electric field as well as the wave functions of the two coupled states. The angular momentum components together with the field polarization, lead to an angular integral of the spherical harmonics, which can be computed analytically with the help of the Clebsh-Gordan coefficients. On the other hand, the radial dependence of the coupling strength between state $|n_i, l_i\rangle$ and $|n_f, l_f\rangle$ is given by the so-called reduced dipole matrix element, i.e.,

$$\langle n_f, l_f || r || n_i, l_i \rangle = \int_0^\infty dr r^2 P_{n_i, l_i}(r) r P_{n_f, l_f}(r) \quad (\text{A.1})$$

where $P_{n,l}(r)$ is the radial part of the electronic wave function defined with the normalization

$$\int_0^\infty dr r^2 P_{n,l}^2(r) = 1, \quad (\text{A.2})$$

and similarly for the orthogonality relationship. Alternatively, in some other contexts, the function $\phi_{n,l}(r) = P_{n,l}(r)r$ is also sometimes referred as the normalized spatial wave function.

The wave function $P_{n,l}$ of an atom depends only on the principle quantum number n and the orbital angular momentum l . These functions can be solved analytically for the hydrogen atom, but, analytical solutions of the wave functions of other atoms are not known. For alkali-metal atoms, there is only one valence electron that interacts with the environment. With the quantum defect theory,

Appendix A. Reduced dipole matrix element

such atoms can be treated as effective one-electron atoms and numerical method for computing the reduced matrix elements are available. In this work, we follow closely the numerical method presented in [92].

Physically the wave function changes dramatically near the core and becomes smoother as the radial distance r increases. Therefore, to have a reasonable description of the wave function, more computation points are required for small r . To deal with this efficiently, we use the logarithmic scaling of the distance r . Let

$$x = \ln r, \quad (\text{A.3})$$

so that the radial distance r increases exponentially with x . We define a new function

$$X = \sqrt{r}P_{n,l}, \quad (\text{A.4})$$

whose second derivative is, thus, given by

$$\begin{aligned} \frac{d^2 X}{dx^2} &= \frac{d}{dx} \left(\frac{d}{dx} r \right) \frac{d}{dr} \sqrt{r} P_{n,l} \\ &= r \frac{d}{dr} r \left(\frac{1}{2\sqrt{r}} P_{n,l} + \sqrt{r} \frac{d}{dr} P_{n,l} \right) \\ &= \left(\frac{\sqrt{r}}{4} + 2r^{3/2} \frac{d}{dr} + r^{5/2} \frac{d^2}{dr^2} \right) P_{n,l}. \end{aligned} \quad (\text{A.5})$$

The Schrödinger equation for the radial part of the electronic wave function is

$$-\frac{\hbar^2}{2\mu} \left(\frac{d^2}{dr^2} + \frac{2}{r} \frac{d}{dr} - \frac{l(l+1)}{r^2} \right) P_{n,l} = [E - V(r)] P_{n,l}, \quad (\text{A.6})$$

where μ is the reduced mass of the valence electron and the core (including the bounded electrons) system, E is the energy and $V(r)$ is the Coulomb potential. Equation (A.6) can be rewritten as

$$\frac{\hbar^2}{\mu} \left(\frac{r^{1/2}}{4} + 2r^{3/2} \frac{d}{dr} + r^{5/2} \frac{d^2}{dr^2} \right) P_{n,l} = \left[2e^{2x}(V - E) - \left(l + \frac{1}{2} \right)^2 \right] P_{n,l}, \quad (\text{A.7})$$

which suggests that

$$\frac{d^2}{dx^2}X(x) = g(x)X(x), \quad (\text{A.8})$$

where

$$g(x) = \frac{\mu}{\hbar^2} \left[2e^{2x}(V - E) - \left(l + \frac{1}{2} \right)^2 \right]. \quad (\text{A.9})$$

In atomic units, the reduced mass $\mu = m_e M / (m_e + M) \approx m_e = 1$, and the expression for $g(x)$ in Eq. (A.9) is reduced to

$$g(x) = 2e^{2x}(V - E) - \left(l + \frac{1}{2} \right)^2. \quad (\text{A.10})$$

For a hydrogen atom, the potential experienced by the atom is given by the Coulomb potential of a point like nucleus, i.e.,

$$V_0 = -\frac{1}{r}. \quad (\text{A.11})$$

For alkali atoms, V_0 approximately represents the single-electron central field due to the nucleus and core electrons. For a core consisting of many nucleons, the motion of the valence electron is able to polarize or penetrate the core. To the lowest order, the potential due to this effect is given by

$$V_p = -\frac{1}{2}\alpha_d \frac{1}{r^4}, \quad (\text{A.12})$$

where α_d is the dipole polarizability of the core. The spin-orbital interaction also has an effect on the potential experienced by the valence electron [100], however, that is a higher-order effect which would not be accounted for here. Therefore, for the potential, we have $V = V_0 + V_p$. For the core polarizability, we use the numbers given in [92], i.e., $\alpha_d = 0.191$ for Li and $\alpha_d = 9.023$ for Rb, in atomic units.

Numerical Algorithm: Numerically, we can solve the second-order differential equation for $X(x)$ given by Eqs. (A.8) and (A.10) to obtain the radial wave function

Appendix A. Reduced dipole matrix element

with $P_{n,l}(r) = X(\ln r)/\sqrt{r}$. With the boundary condition $P_{n,l}(r \rightarrow \infty) = 0$, the second-order differential equation for $X(x)$ can be solved by integrating inwards from large x . Let r_s being the boundary value for r , with a logarithmic step size h , we have $r_j = r_s e^{-jh}$ for $j = 0, 1, 2, 3, \dots$ and

$$x_j = \ln r_j = \ln r_s - jh. \quad (\text{A.13})$$

The Runge-Kutta method can be applied to solve the differential equation. However, for simplicity, we directly use the established numerical algorithm for solving a second-order ordinary differential equation of this form [92]:

$$X_{j+1} = \frac{[X_{j-1}(g_{j-1} - 12) + X_j(10g_j + 24)]}{(12 - g_{j+1})}, \quad (\text{A.14})$$

where

$$g_j = 2r_j^2 [V(r_j) - E] + (l + 1/2)^2. \quad (\text{A.15})$$

The wave function obtained this way is not properly normalized, and the reduced dipole matrix elements with proper normalization of the wave functions is given by

$$\begin{aligned} \langle \Phi_f || r || \Phi_i \rangle &= \frac{\int_0^\infty P_{n_i, l_i}(r) r^3 P_{n_f, l_f}(r) dr}{\sqrt{\int_0^\infty P_{n_i, l_i}^2(r) r^2 dr \int_0^\infty P_{n_f, l_f}^2(r') r'^2 dr'}}, \\ &= \frac{\sum_j X_j(n_i, l_i) X_j(n_f, l_f) r_j^3}{\sqrt{\sum_j X_j^2(n_i, l_i) r_j^2 \sum_k X_k^2(n_f, l_f) r_k^2}}. \end{aligned} \quad (\text{A.16})$$

Physically, the wave function $P_{nl}(r \rightarrow \infty) = 0$, and the starting point we choice as a reference for $P_{nl}(r_s) = 0$ is

$$r_s = 2n(n + 15)a_0, \quad (\text{A.17})$$

where a_0 is the Bohr radius (choosing a larger boundary point would not affect the results). The initial slope of the radial wave function is taken to be that of a decreasing exponential, that is $f'(r) = -e^{-r/n}/n$ for function $f(r) = e^{-r/n}$.

Therefore,

$$X_1 = 0 \tag{A.18}$$

$$X_2 = \Delta r f'(r_s) = \frac{r_s}{n} (1 - e^{-h}) e^{-r_s/n}. \tag{A.19}$$

A cutoff point as the radius to terminate the calculation in the inward direction is also required, as for very small r , the Schrödinger equation with the potential $V = V_0 + V_p$ no longer describes the physics well and more complicated forces like nuclear-binding force would interfere with the system. Nevertheless, we do not need to take into account of the situation for very small r in the calculation for the reduced dipole matrix element, as these terms go with r^2 or r^3 and the contribution to the integral for small r is negligible. For the calculation given in this work, the cutoff point is taken to be $\alpha_d^{1/3}$.

Unitarity of the approximate evolution operators

In Sec. 5.3.3, the evolution operator of a two-photon Raman transition can be approximated successively with the help of Lippmann-Schwinger equations, and the solutions $U_k(t)$ are accurate up to the k th order in ϵ . Thus, the evolution operator $U_k(t)$ is approximately unitary with

$$U_k(t)U_k(t)^\dagger - 1 = w_k(t) \sim O(\epsilon^{k+1}). \quad (\text{B.1})$$

In Eq. (5.45), the unitarity of the evolution of states is preserved by applying $U_k(t)$ to the initial state and normalize the probability amplitude at time t . This might be the simplest way to ensure the proper normalization of $\Psi_I(t)$, however, the evolutionary operator obtained this way is state-dependent. Alternative methods to preserve the unitarity of operator $U_k(t)$ are conceivable. Here we discuss one method for obtaining a unitary operator by first defining

$$\tilde{U}_k(t) = C_k(t)U_k(t) \quad (\text{B.2})$$

and, then, finding an operator $C(k)$ such that $C_k(t)U_k(t)U_k^\dagger(t)C_k^\dagger(t) = 1$ and $C_k(t) \rightarrow 1$ as $w_k(t) = U_k(t)U_k^\dagger(t) - 1 \rightarrow 0$. This can be achieved with the operator

$$C_k(t) = \prod_{n=0}^{\infty} \left[1 + e^{i\frac{2\pi}{3}} w_k(t)^{3^n} \right], \quad (\text{B.3})$$

Appendix B. Unitarity of the approximate evolution operators

and this guarantees that the operator $\tilde{U}_k(t)$ is unitary exactly. The product in Eq. B.3 converges very rapidly, with an accuracy of order ϵ^{3mk} if one stops after including the first m factors. In practice, it is often efficient to take the first term only,

$$C_k(t) \simeq \left[1 + e^{i\frac{2\pi}{3}} (U_k(t)U_k^\dagger(t) - 1) \right], \quad (\text{B.4})$$

and then the normalized state-independent evolution operator is

$$\tilde{U}_k(t) \simeq \left[1 + e^{i\frac{2\pi}{3}} (U_k(t)U_k^\dagger(t) - 1) \right] U_k(t). \quad (\text{B.5})$$

Bibliography

- [1] M. E. Gehm, *Preparation of an Optically-Trapped Degenerate Fermi Gas of ${}^6\text{Li}$: Finding the Rout to Degeneracy*. PhD thesis, Duke University, 2003.
- [2] R. Feynman, “Simulating physics with computers,” *International Journal of Theoretical Physics*, vol. 21, pp. 467–488, 1982.
- [3] M. A. Nielsen and I. L. Chuang, *Quantum Computation and Quantum Information*. Cambridge University Press, 2000.
- [4] C. H. Bennett and G. Brassard, “Quantum Cryptography: Public Key Distribution and Coin Tossing,” *In Proceedings of the IEEE International Conference on Computers, Systems and Signal Processing*, pp. 175–179, 1984.
- [5] A. K. Ekert, “Quantum cryptography based on Bell’s theorem,” *Phys. Rev. Lett.*, vol. 67, pp. 661–663, 1991.
- [6] T. Schmitt-Manderbach, H. Weier, M. Fürst, R. Ursin, F. Tiefenbacher, T. Scheidl, J. Perdigues, Z. Sodnik, C. Kurtsiefer, J. G. Rarity, A. Zeilinger, and H. Weinfurter, “Experimental Demonstration of Free-Space Decoy-State Quantum Key Distribution over 144 km,” *Phys. Rev. Lett.*, vol. 98, p. 010504, 2007.
- [7] H.-J. Briegel, W. Dür, J. I. Cirac, and P. Zoller, “Quantum Repeaters: The Role of Imperfect Local Operations in Quantum Communication,” *Phys. Rev. Lett.*, vol. 81, pp. 5932–5935, 1998.
- [8] T. D. Ladd, F. Jelezko, R. Laflamme, Y. Nakamura, C. Monroe, and J. L. O’Brien, “Quantum Computers,” *Nature*, vol. 464, pp. 45–53, 2010.
- [9] C. Simon, M. Afzelius, J. Appel, A. B. Giroday, S. J. Dewhurst, N. Gisin, C. Y. Hu, F. Jelezko, S. Kröll, J. H. Müller, J. Nunn, E. S. Polzik, J. G. Rarity, H. De Riedmatten, W. Rosenfeld, A. J. Shields, N. Sköld, R. M. Stevenson, R. Thew, I. A. Walmsley, M. C. Weber, H. Weinfurter, J. Wrachtrup,

BIBLIOGRAPHY

- and R. J. Young, “Quantum Memories. A Review based on the European Integrated Project ‘Qubit Applications (QAP)’,” *Eur. Phys. J. D*, vol. 58, pp. 1–22, 2010.
- [10] S. Chen, Y.-A. Chen, T. Strassel, Z.-S. Yuan, B. Zhao, J. Schmiedmayer, and J.-W. Pan, “Deterministic and Storable Single-Photon Source Based on a Quantum Memory,” *Phys. Rev. Lett.*, vol. 97, p. 173004, 2006.
- [11] C. Simon and W. T. M. Irvine, “Robust Long-Distance Entanglement and a Loophole-Free Bell Test with Ions and Photons,” *Phys. Rev. Lett.*, vol. 91, p. 110405, 2003.
- [12] M. F. Riedel, P. Böhi, Y. Li, T. W. Hänsch, A. Sinatra, and P. Treutlein, “Atom-chip-based generation of entanglement for quantum metrology,” *Nature*, vol. 464, pp. 1170–1173, 2010.
- [13] D. P. DiVincenzo, “The physical implementation of quantum computation,” *Fortschr. Phys.*, vol. 48, 2000.
- [14] E. Knill, R. Laflamme, and G. J. Milburn, “A scheme for efficient quantum computation with linear optics,” *Nature*, vol. 409, pp. 46–52, 2001.
- [15] J. L. O’Brien, “Optical quantum computing,” *Science*, vol. 318, pp. 1567–1570, 2007.
- [16] H. J. Briegel and R. Raussendorf, “Persistent Entanglement in Arrays of Interacting Particles,” *Phys. Rev. Lett.*, vol. 86, pp. 910–913, 2001.
- [17] C. Y. Hu, W. J. Munro, and J. G. Rarity, “Deterministic photon entangler using a charged quantum dot inside a microcavity,” *Phys. Rev. B*, vol. 78, p. 125318, 2008.
- [18] H. Wang, M. Mariantoni, R. C. Bialczak, M. Lenander, E. Lucero, M. Neeley, A. D. O’Connell, D. Sank, M. Weides, J. Wenner, T. Yamamoto, Y. Yin, J. Zhao, J. M. Martinis, and A. N. Cleland, “Deterministic Entanglement of

- Photons in Two Superconducting Microwave Resonators,” *Phys. Rev. Lett.*, vol. 106, p. 060401, 2011.
- [19] T. Monz, P. Schindler, J. T. Barreiro, M. Chwalla, D. Nigg, W. A. Coish, M. Harlander, W. Hänsel, M. Hennrich, and R. Blatt, “14-Qubit Entanglement: Creation and Coherence,” *Phys. Rev. Lett.*, vol. 106, p. 130506, 2011.
- [20] J. I. Cirac and P. Zoller, “Quantum Computations with Cold Trapped Ions,” *Phys. Rev. Lett.*, vol. 74, pp. 4091–4094, 1995.
- [21] D. J. Wineland, C. Monroe, W. Itano, D. Leibfried, B. King, and D. Meekhof, “Experimental issues in coherent quantum-state manipulation,” *J. Res. Natl. Inst. Stand. Tech.*, vol. 103, pp. 259–328, 1998.
- [22] E. Knill, D. Leibfried, R. Reichle, J. Britton, R. B. Blakestad, J. D. Jost, C. Langer, R. Ozeri, S. Seidelin, and D. J. Wineland, “Randomized benchmarking of quantum gates,” *Phys. Rev. A*, vol. 77, p. 012307, 2008.
- [23] D. J. Wineland and R. Blatt, “Entangled states of trapped atomic ions,” *Nature*, vol. 453, pp. 1008 – 1015, 2008.
- [24] W. Rosenfeld, F. Hocke, F. Henkel, M. Krug, J. Volz, M. Weber, and H. Weinfurter, “Towards Long-Distance Atom-Photon Entanglement,” *Phys. Rev. Lett.*, vol. 101, p. 260403, 2008.
- [25] H. P. Specht, C. Nolleke, A. Reiserer, M. Uphoff, E. Figueroa, S. Ritter, and G. Rempe, “A single-atom quantum memory,” *Nature*, vol. 473, pp. 190–193, 2011.
- [26] A. Gaëtan, Y. Miroshnychenko, T. Wilk, A. Chotia, M. Viteau, D. Comparat, P. Pillet, A. Browaeys, and P. Grangier, “Observation of collective excitation of two individual atoms in the Rydberg blockade regime,” *Nature Physics*, vol. 5, pp. 115–118, 2009.
- [27] E. Urban, T. A. Johnson, T. Henage, L. Isenhower, D. D. Yavuz, T. G.

BIBLIOGRAPHY

- Walker, and M. Saffman, “Observation of Rydberg blockade between two atoms,” *Nature Physics*, vol. 5, pp. 110–114, 2009.
- [28] C. Weitenberg, M. Endres, J. F. Sherson, M. Cheneau, P. Schausz, T. Fukuhara, and I. Bloch, “Single-spin addressing in an atomic Mott insulator,” *Nature*, vol. 471, pp. 319–324, 2008.
- [29] M. D. Lukin, M. Fleischhauer, R. Cote, L. M. Duan, D. Jaksch, J. I. Cirac, and P. Zoller, “Dipole Blockade and Quantum Information Processing in Mesoscopic Atomic Ensembles,” *Phys. Rev. Lett.*, vol. 87, p. 037901, 2001.
- [30] K. Hammerer, A. S. Sørensen, and E. S. Polzik, “Quantum interface between light and atomic ensembles,” *Rev. Mod. Phys.*, vol. 82, pp. 1041–1093, 2010.
- [31] C. Negrevergne, T. S. Mahesh, C. A. Ryan, M. Ditty, F. Cyr-Racine, W. Power, N. Boulant, T. Havel, D. G. Cory, and R. Laflamme, “Benchmarking Quantum Control Methods on a 12-Qubit System,” *Phys. Rev. Lett.*, vol. 96, no. 17, p. 170501, 2006.
- [32] F. H. L. Koppens, C. Buizert, K. J. Tielrooij, I. T. Vink, K. C. Nowack, T. Meunier, L. P. Kouwenhoven, and L. M. K. Vandersypen, “Driven coherent oscillations of a single electron spin in a quantum dot,” *Nature*, vol. 442, pp. 766–771, 2006.
- [33] J. R. Petta, A. C. Johnson, J. M. Taylor, E. A. Laird, A. Yacoby, M. D. Lukin, C. M. Marcus, M. P. Hanson, and A. C. Gossard, “Coherent Manipulation of Coupled Electron Spins in Semiconductor Quantum Dots,” *Science*, vol. 309, no. 5744, pp. 2180–2184, 2005.
- [34] D. Press, T. D. Ladd, B. Zhang, and Y. Yamamoto, “Complete quantum control of a single quantum dot spin using ultrafast optical pulses,” *Nature*, vol. 456, pp. 218–221, 2008.
- [35] M. V. G. Dutt, L. Childress, L. Jiang, E. Togan, J. Maze, F. Jelezko, A. S. Zibrov, P. R. Hemmer, and M. D. Lukin, “Quantum Register Based on In-

- dividual Electronic and Nuclear Spin Qubits in Diamond,” *Science*, vol. 316, no. 5829, pp. 1312–1316, 2007.
- [36] G. Balasubramanian, P. Neumann, D. Twitchen, M. Markham, R. Kolesov, N. Mizuochi, J. Isoya, J. Achard, J. Beck, J. Tissler, V. Jacques, P. R. Hemmer, F. Jelezko, and J. Wrachtrup, “Ultralong spin coherence time in isotopically engineered diamond,” *Nature Materials*, vol. 8, pp. 383–387, 2009.
- [37] P. E. Barclay, C. Santori, K.-M. Fu, R. G. Beausoleil, and O. Painter, “Coherent interference effects in a nano-assembled diamond NV center cavity-QED system,” *Opt. Express*, vol. 17, no. 10, pp. 8081–8097, 2009.
- [38] L. DiCarlo, J. M. Chow, J. M. Gambetta, L. S. Bishop, B. R. Johnson, D. I. Schuster, J. Majer, A. Blais, L. Frunzio, S. M. Girvin, and R. J. Schoelkopf, “Demonstration of two-qubit algorithms with a superconducting quantum processor,” *Nature*, vol. 460, pp. 240–244, 2009.
- [39] J. A. Schreier, A. A. Houck, J. Koch, D. I. Schuster, B. R. Johnson, J. M. Chow, J. M. Gambetta, J. Majer, L. Frunzio, M. H. Devoret, S. M. Girvin, and R. J. Schoelkopf, “Suppressing charge noise decoherence in superconducting charge qubits,” *Phys. Rev. B*, vol. 77, p. 180502, 2008.
- [40] H. Paik, D. I. Schuster, L. S. Bishop, G. Kirchmair, G. Catelani, A. P. Sears, B. R. Johnson, M. J. Reagor, L. Frunzio, L. I. Glazman, S. M. Girvin, M. H. Devoret, and R. J. Schoelkopf, “Observation of High Coherence in Josephson Junction Qubits Measured in a Three-Dimensional Circuit QED Architecture,” *Phys. Rev. Lett.*, vol. 107, p. 240501, 2011.
- [41] P. Aliferis and A. W. Cross, “Subsystem Fault Tolerance with the Bacon-Shor Code,” *Phys. Rev. Lett.*, vol. 98, p. 220502, 2007.
- [42] P. W. Shor, “Scheme for reducing decoherence in quantum computer memory,” *Phys. Rev. A*, vol. 52, pp. 2493–2496, 1995.

BIBLIOGRAPHY

- [43] L. Viola, E. Knill, and S. Lloyd, “Dynamical Decoupling of Open Quantum Systems,” *Phys. Rev. Lett.*, vol. 82, pp. 2417–2421, 1999.
- [44] D. Lidar and K. Birgitta Whaley, “Decoherence-Free Subspaces and Subsystems,” in *Irreversible Quantum Dynamics* (F. Benatti and R. Floreani, eds.), vol. 622 of *Lecture Notes in Physics*, pp. 83–120, Springer Berlin/Heidelberg, 2003.
- [45] P. G. Kwiat, A. J. Berglund, J. B. Altepeter, and A. G. White, “Experimental Verification of Decoherence-Free Subspaces,” *Science*, vol. 290, no. 5491, pp. 498–501, 2000.
- [46] D. Kielpinski, V. Meyer, M. A. Rowe, C. A. Sackett, W. M. Itano, C. Monroe, and D. J. Wineland, “A Decoherence-Free Quantum Memory Using Trapped Ions,” *Science*, vol. 291, no. 5506, pp. 1013–1015, 2001.
- [47] E. M. Fortunato, L. Viola, J. Hodges, G. Teklemariam, and D. G. Cory, “Implementation of universal control on a decoherence-free qubit,” *New Journal of Physics*, vol. 4, no. 1, p. 5, 2002.
- [48] L. Viola, E. M. Fortunato, M. A. Pravia, E. Knill, R. Laflamme, and D. G. Cory, “Experimental Realization of Noiseless Subsystems for Quantum Information Processing,” *Science*, vol. 293, no. 5537, pp. 2059–2063, 2001.
- [49] R. Han, N. Lörch, J. Suzuki, and B.-G. Englert, “Long-lived qubit from three spin-1/2 atoms,” *Phys. Rev. A*, vol. 84, p. 012322, 2011.
- [50] C. Boisseau, I. Simbotin, and R. Côté, “Macrodimers: Ultralong Range Rydberg Molecules,” *Phys. Rev. Lett.*, vol. 88, p. 133004, 2002.
- [51] K. Singer, M. Reetz-Lamour, T. Amthor, S. Flling, M. Tschernack, and M. Weidemüller, “Spectroscopy of an ultracold Rydberg gas and signatures of Rydberg-Rydberg interactions,” *J. Phys. B: At. Mol. Opt. Phys.*, vol. 38, no. 2, p. 321, 2005.

- [52] M. Saffman, T. G. Walker, and K. Mølmer, “Quantum information with Rydberg atoms,” *Rev. Mod. Phys.*, vol. 82, pp. 2313–2363, 2010.
- [53] D. Jaksch, J. I. Cirac, P. Zoller, S. L. Rolston, R. Côté, and M. D. Lukin, “Fast Quantum Gates for Neutral Atoms,” *Phys. Rev. Lett.*, vol. 85, pp. 2208–2211, 2000.
- [54] T. F. Gallagher, *Rydberg Atoms*. Cambridge University Press, 2005.
- [55] L. Isenhower, E. Urban, X. L. Zhang, A. T. Gill, T. Henage, T. A. Johnson, T. G. Walker, and M. Saffman, “Demonstration of a Neutral Atom Controlled-NOT Quantum Gate,” *Phys. Rev. Lett.*, vol. 104, p. 010503, 2010.
- [56] M. Murphy, S. Montangero, T. Calarco, P. Grangier, and A. Browaeys, “Towards an experimentally feasible controlled-phase gate on two blockaded Rydberg atoms,” *arXiv:1111.6083v1*, 2011.
- [57] M. Saffman and T. G. Walker, “Creating single-atom and single-photon sources from entangled atomic ensembles,” *Phys. Rev. A*, vol. 66, p. 065403, 2002.
- [58] I. Bouchoule and K. Mølmer, “Spin squeezing of atoms by the dipole interaction in virtually excited Rydberg states,” *Phys. Rev. A*, vol. 65, p. 041803, 2002.
- [59] E. Brion, K. Mølmer, and M. Saffman, “Quantum Computing with Collective Ensembles of Multilevel Systems,” *Phys. Rev. Lett.*, vol. 99, p. 260501, 2007.
- [60] M. Saffman and K. Mølmer, “Scaling the neutral-atom Rydberg gate quantum computer by collective encoding in holmium atoms,” *Phys. Rev. A*, vol. 78, p. 012336, 2008.
- [61] D. Møller, L. B. Madsen, and K. Mølmer, “Quantum Gates and Multiparticle Entanglement by Rydberg Excitation Blockade and Adiabatic Passage,” *Phys. Rev. Lett.*, vol. 100, p. 170504, 2008.

BIBLIOGRAPHY

- [62] R. Heidemann, U. Raitzsch, V. Bendkowsky, B. Butscher, R. Löw, L. Santos, and T. Pfau, “Evidence for Coherent Collective Rydberg Excitation in the Strong Blockade Regime,” *Phys. Rev. Lett.*, vol. 99, p. 163601, 2007.
- [63] H. Weimer, M. Müller, H. P. Büchler, and I. Lesanovsky, “Digital Quantum Simulation with Rydberg Atoms,” *Quantum Information Processing*, vol. 10, 2011.
- [64] A. V. Gorshkov, J. Otterbach, M. Fleischhauer, T. Pohl, and M. D. Lukin, “Photon-Photon Interactions via Rydberg Blockade,” *Phys. Rev. Lett.*, vol. 107, p. 133602, 2011.
- [65] C. Cohen-Tannoudji, J. Dupont-Roc, and G. Grynberg, *Atom-Photon Interactions: Basic Processes and Applications*. Wiley, 1992.
- [66] M. O. Scully and M. S. Zubairy, *Quantum Optics*. Cambridge University Press, 1997.
- [67] E. Kyrölä and M. Lindberg, “Serial and parallel multilevel systems,” *Phys. Rev. A*, vol. 35, pp. 4207–4225, 1987.
- [68] Z. Deng, “Separated subsystems in four-level atom,” *Optics Communications*, vol. 48, no. 4, pp. 284 – 286, 1983.
- [69] J. Oreg, F. T. Hioe, and J. H. Eberly, “Adiabatic following in multilevel systems,” *Phys. Rev. A*, vol. 29, pp. 690–697, 1984.
- [70] J. R. Kuklinski, U. Gaubatz, F. T. Hioe, and K. Bergmann, “Adiabatic population transfer in a three-level system driven by delayed laser pulses,” *Phys. Rev. A*, vol. 40, pp. 6741–6744, 1989.
- [71] C. J. Foot, *Atomic Physics*. Oxford University Press, 2005.
- [72] M. Kasevich and S. Chu, “Laser cooling below a photon recoil with three-level atoms,” *Phys. Rev. Lett.*, vol. 69, pp. 1741–1744, 1992.

- [73] A. J. Kerman, V. Vuletić, C. Chin, and S. Chu, “Beyond Optical Molasses: 3D Raman Sideband Cooling of Atomic Cesium to High Phase-Space Density,” *Phys. Rev. Lett.*, vol. 84, pp. 439–442, 2000.
- [74] A. D. Boozer, R. Miller, T. E. Northup, A. Boca, and H. J. Kimble, “Optical pumping via incoherent Raman transitions,” *Phys. Rev. A*, vol. 76, p. 063401, 2007.
- [75] S. D. Bartlett, T. Rudolph, and R. W. Spekkens, “Reference frames, superselection rules, and quantum information,” *Rev. Mod. Phys.*, vol. 79, pp. 555–609, 2007.
- [76] J. Suzuki, G. N. M. Tabia, and B.-G. Englert, “Symmetric construction of reference-frame-free qubit,” *Phys. Rev. A*, vol. 78, p. 052328, 2008.
- [77] D. A. Lidar and K. B. Whaley, “Decoherence-Free Subspaces and Subsystems,” *Springer Lecture Notes in Physics – Irreversible Quantum Dynamics*, vol. 622, 2003.
- [78] D. A. Steck, “Rubidium 87 D Line Data,” <http://steck.us/alkalidata>, 2001.
- [79] K. L. Lee, B. Grémaud, R. Han, B.-G. Englert, and C. Miniatura, “Ultracold fermions in a graphene-type optical lattice,” *Phys. Rev. A*, vol. 80, p. 043411, 2009.
- [80] H.-P. Breuer and F. Petruccione, *The theory of open quantum systems*. Oxford University Press, Oxford and New York, 2002.
- [81] N. Lörch, *A study of open quantum systems*. Diplomarbeit: Universität Heidelberg, 2010.
- [82] T. A. Fulton and G. J. Dolan, “Observation of single-electron charging effects in small tunnel junctions,” *Phys. Rev. Lett.*, vol. 59, pp. 109–112, 1987.
- [83] D. V. Averin and K. K. Likharev, “Coulomb blockade of single-electron tunneling, and coherent oscillations in small tunnel junctions,” *Journal of Low Temperature Physics*, vol. 62, pp. 345–373, 1986.

BIBLIOGRAPHY

- [84] K. Ono, D. G. Austing, Y. Tokura, and S. Tarucha, “Current Rectification by Pauli Exclusion in a Weakly Coupled Double Quantum Dot System,” *Science*, vol. 297, no. 5585, pp. 1313–1317, 2002.
- [85] K. M. Birnbaum, A. Boca, R. Miller, A. D. Boozer, T. E. Northup, and H. J. Kimble, “Photon blockade in an optical cavity with one trapped atom,” *Nature*, vol. 436, pp. 87–90, 2005.
- [86] M. J. Seaton, “Quantum defect theory,” *Rep. Prog. Phys.*, 1983.
- [87] T. Pohl and P. R. Berman, “Breaking the Dipole Blockade: Nearly Resonant Dipole Interactions in Few-Atom Systems,” *Phys. Rev. Lett.*, vol. 102, p. 013004, 2009.
- [88] T. G. Walker and M. Saffman, “Consequences of Zeeman degeneracy for the van der Waals blockade between Rydberg atoms,” *Phys. Rev. A*, vol. 77, p. 032723, 2008.
- [89] F. Schmidt-Kaler, T. Feldker, D. Kolbe, J. Walz, M. Mller, P. Zoller, W. Li, and I. Lesanovsky, “Rydberg excitation of trapped cold ions: a detailed case study,” *New Journal of Physics*, vol. 13, no. 7, p. 075014, 2011.
- [90] P. Goy, J. Liang, M. Gross, and S. Haroche, “Quantum defects and specific-isotopic-shift measurements in ns and np highly excited states of lithium: Exchange effects between Rydberg and core electrons,” *Phys. Rev. A*, vol. 34, pp. 2889–2896, 1986.
- [91] C.-J. Lorenzen and K. Niemax, “Quantum Defects of the $n2P_{1/2,3/2}$ Levels in ^{39}K I and ^{85}Rb I,” *Physica Scripta*, vol. 27, no. 4, p. 300, 1983.
- [92] M. L. Zimmerman, M. G. Littman, M. M. Kash, and D. Kleppner, “Stark structure of the Rydberg states of alkali-metal atoms,” *Phys. Rev. A*, vol. 20, pp. 2251–2275, 1979.
- [93] E. Brion, L. H. Pedersen, and K. Mølmer, “Adiabatic elimination in a

- lambda system,” *Journal of Physics A: Mathematical and Theoretical*, vol. 40, pp. 1033–1043, 2007.
- [94] V. Paulisch, R. Han, H. K. Ng, and B.-G. Englert, “Raman transitions: Adiabatic elimination revisited,” *arXiv:1209.6568*, 2012.
- [95] R. Han, H. K. Ng, and B.-G. Englert, “Raman transitions without adiabatic elimination: A simple and accurate treatment,” *arXiv:1209.6569*, 2012.
- [96] M. Fleischhauer and A. S. Manka, “Propagation of laser pulses and coherent population transfer in dissipative three-level systems: An adiabatic dressed-state picture,” *Phys. Rev. A*, vol. 54, pp. 794–803, 1996.
- [97] Y. Miroshnychenko, A. Gaëtan, C. Evellin, P. Grangier, D. Comparat, P. Pillet, T. Wilk, and A. Browaeys, “Coherent excitation of a single atom to a Rydberg state,” *Phys. Rev. A*, vol. 82, p. 013405, 2010.
- [98] J. P. Barratt and C. Cohen-Tannoudji, “Étude du pompage optique dans le formalisme de la matrice densité,” *J. phys. radium*, vol. 22, no. 329 and 443, 1961.
- [99] R. H. Dicke, “Coherence in Spontaneous Radiation Processes,” *Phys. Rev.*, vol. 93, pp. 99–110, 1954.
- [100] C. E. Theodosiou, “Lifetimes of alkali-metal—atom Rydberg states,” *Phys. Rev. A*, vol. 30, pp. 2881–2909, 1984.